

MAMBO Mapping of Spitzer c2d Small Clouds and Cores[★]

Jens Kauffmann^{1,2,3}, Frank Bertoldi⁴, Tyler L. Bourke³, Neal J. Evans II⁵, and Chang Won Lee^{3,6}

¹ Max-Planck-Institut für Radioastronomie, Auf dem Hügel 69, D-53121 Bonn, Germany

² Initiative in Innovative Computing at Harvard University, 60 Oxford Street, 02138 Cambridge, MA, USA

³ Harvard-Smithsonian Center for Astrophysics, 60 Garden Street, 02138 Cambridge, MA, USA

⁴ Argelander Institut für Astronomie, Universität Bonn, Auf dem Hügel 71, D-53121 Bonn, Germany

⁵ Department of Astronomy, University of Texas at Austin, 1 University Station C1400, 78712 Austin, TX, USA

⁶ Korea Astronomy and Space Science Institute, 61-1 Hwaam-dong, Yuseong-gu, Daejeon 305-348, Korea

Received xxx; accepted xxx

ABSTRACT

Aims. To study the structure of nearby (< 500 pc) dense starless and star-forming cores with the particular goal to identify and understand evolutionary trends in core properties, and to explore the nature of Very Low Luminosity Objects ($\leq 0.1 L_{\odot}$; VeLLOs).

Methods. Using the MAMBO bolometer array, we create maps unusually sensitive to faint (few mJy per beam) extended ($\approx 5'$) thermal dust continuum emission at 1.2 mm wavelength. Complementary information on embedded stars is obtained from Spitzer, IRAS, and 2MASS. [The journal article will come with FITS files of the maps.]

Results. Our maps are very rich in structure, and we characterize extended emission features (“subcores”) and compact intensity peaks in our data separately to pay attention to this complexity. We derive, e.g., sizes, masses, and aspect ratios for the subcores, as well as column densities and related properties for the peaks. Combination with archival infrared data then enables the derivation of bolometric luminosities and temperatures, as well as envelope masses, for the young embedded stars.

Conclusions. Starless and star-forming cores occupy the same parameter space in many core properties; a picture of dense core evolution in which any dense core begins to actively form stars once it exceeds some fixed limit in, e.g., mass, density, or both, is inconsistent with our data. A concept of *necessary conditions* for star formation appears to provide a better description: dense cores fulfilling certain conditions *can* form stars, but they do not need to, respectively have not done so yet. Comparison of various evolutionary indicators for young stellar objects in our sample (e.g., bolometric temperatures) reveals inconsistencies between some of them, possibly suggesting a revision of some of these indicators. Finally, we challenge the notion that VeLLOs form in cores not expected to actively form stars, and we present a first systematic study revealing evidence for structural differences between starless and candidate VeLLO cores.

Key words. Stars: formation – ISM: evolution – ISM: structure – ISM: dust – ISM: clouds

1. Introduction

Stars form from dense gas ($\gg 10^5$ cm⁻³). Such gas is, e.g., found in discrete nearby ($\lesssim 500$ pc) cold (≈ 10 K) small-scale ($\lesssim 0.1$ pc) condensations referred to as dense cores (Myers et al. 1983). These are thought to be the sites where low-mass stars form (Myers & Benson 1983). Their properties provide the initial conditions for star formation. It is thus necessary to understand the physical state of dense cores in order to be able to understand the star formation process in detail.

Some of the many physical parameters of dense cores are their sizes, masses, and densities. Given that thermal dust continuum emission at ≈ 1 mm wavelength is a better mass tracer than molecular emission lines (e.g., Tafalla et al. 2002), and that modern bolometer cameras enable complete maps of the dust emission from dense cores to be made within a short time, dust emission maps are a prime tool to study the above core parameters. Dust emission surveys thus enable a systematic overview of dense core properties.

In recent years several surveys studied dense cores in large (up to several 10 pc) and massive (up to several $10^3 M_{\odot}$) complexes of molecular clouds (Motte et al. 1998; Johnstone & Bally

2006; Johnstone et al. 2004, 2001, 2006, 2000; Hatchell et al. 2005; Enoch et al. 2007, 2006; Young et al. 2006b; Stanke et al. 2006). Most cores in these clouds are in groups and clusters (e.g., Enoch et al. 2007). Although it is believed that most stars in the galaxy form in such environments (Magnani et al. 1995), two issues make it difficult to study the fundamental physics of star formation in such environments. First, cores can be confused in crowded regions forming clusters; it becomes difficult to identify and study individual cores (see, e.g., Motte et al. 1998; see also Ward-Thompson et al. 2007 for illustrative examples). Second, cores might interact in crowded regions; more parameters than relevant in isolated cores influence the evolution of dense cores. These problems can be avoided by studying dense cores in relative isolation (Clemens & Barvainis 1988; Bourke et al. 1995) instead of cores hosted in larger (up to $\gtrsim 100$ pc) complexes of giant molecular clouds (Blitz 1993).

The present study therefore focuses on isolated cores. We have observed both starless cores and cores with embedded stars, covering a large range in size, mass, central density and (supposedly) evolutionary status. This creates a unique database for detailed studies of dependencies between various dense core parameters and their relation to dense core evolution.

Send offprint requests to: J. Kauffmann, jkauffmann@cfa.harvard.edu

[★] Based on observations with the IRAM 30m-telescope.

1.1. The Need for a new Dust Emission Survey

Several surveys of isolated cores with and without active star formation have been conducted in the past ≈ 15 years (e.g., Motte & André 2001, Visser et al. 2002, Kirk et al. 2005, Young et al. 2006a, Wu et al. 2007). They have covered a large number of dense cores in a broad variety of physical states. While these surveys in principle should yield a comprehensive database on the properties of dense cores, this is in fact true only to a limited extent. Many existing studies were relatively insensitive to faint emission (because of noise) and structure on scales beyond $1'$ to $2'$ (due to artifacts, e.g., due to ‘jiggle maps’).

State-of-the-art bolometer cameras nowadays allow for the reliable imaging of faint large-scale ($\gtrsim 5'$) extensions of sources initially — if at all — only detected in their brightest intensity peaks. This urged us to conduct a new comprehensive dust emission survey towards isolated dense cores at ≈ 1 mm wavelength using up-to-date instrumentation. For this we use the Max-Planck Millimetre Bolometer (MAMBO) arrays (Kreysa et al. 1999) at the IRAM 30m-telescope. This combination of telescope and receiver was probably the most sensitive facility for mapping of extended dust emission available before the recent emergence of LABOCA (when considering the levels of extended artifacts and statistical noise). The research presented here is the first census with MAMBO that covers ≥ 10 starless dense cores.

A further motivation of our survey is the demand for complementary data on dense cores for the recent Spitzer Space Telescope imaging surveys of dense cores. Such data is needed to, e.g., put the properties of the stellar content probed by Spitzer in context with dense core properties like density and mass; the latter can usually not be derived from the Spitzer data. In particular the Spitzer Legacy Program “From Molecular Cores to Planet Forming Disks” (AKA. “Cores to Disks” or “c2d”; Evans et al. 2003), which imaged 82 nearby (≤ 500 pc) isolated dense cores as part of its agenda, stimulated a number of coordinated surveys of the c2d cores covering many spectral windows. Our survey — the c2d MAMBO survey — is one of four new dust continuum emission surveys of isolated cores carried out in the c2d framework (with Young et al. 2006a, Wu et al. 2007, and Brede et al., in prep., being the other three).

1.2. Specific Aim of the c2d MAMBO Survey

Dust emission data can be used to address a number of open issues in star formation research. In general, stars are thought to form from very dense molecular cores (H_2 densities $\gtrsim 10^5 \text{ cm}^{-3}$). In particular, the spatial mass distribution is thought to govern the stability of dense cores against gravitational collapse (e.g., McKee & Holliman 1999). One might thus hope to derive criteria to be fulfilled to allow star formation in dense cores by comparing the mass distributions of starless cores with those of cores actively forming stars. This could lead to a better understanding of the underlying star formation physics. The c2d MAMBO survey is ideally suited for such comparative studies since it probes the mass distribution in cores with and without ongoing star formation at high sensitivity (see Sec. 5.3.4 for details).

Also, the evolution of young stellar objects (or “protostars”; hereafter YSOs), i.e., stars that are surrounded by significant amounts of the matter from which they did or do form, can be studied with dust continuum emission data. These allow the investigation of the relation between the broadband spectral prop-

erties, the structure of the circumstellar envelope, and present models of evolutionary schemes (see Sec. 5.4 for details).

Our sample includes four candidate Very Low Luminosity Objects (VeLLOs; see Kauffmann et al. 2005 and di Francesco et al. 2007), enigmatic objects of apparent protostellar nature but unusually low luminosity that were recently discovered by c2d (Young et al. 2004a, Bourke et al. 2005, Dunham et al. 2006; cf. André et al. 1999). They are defined as objects with internal luminosities (i.e., not including the dense core luminosity from interstellar heating due to, e.g., the interstellar radiation field) $\leq 0.1 L_\odot$ that are embedded in dense cores. Some of these objects have been interpreted as very young ($\lesssim 10^4$ years; André et al. 1999) YSOs of stellar final mass (i.e., $\geq 0.08 M_\odot$). Based on their low accretion rates, others are thought to be young objects in the process of growing to substellar final mass (Young et al. 2004a, Bourke et al. 2005; see Dunham et al. 2006 for a summarizing discussion). The c2d MAMBO survey is the first study with a sensitive and homogeneous data set on several starless, YSO, and VeLLO natal cores. This allows comparative studies between these core types to better understand how VeLLO natal cores differ from others (see Sec. 5.5 for details).

1.3. Structure of the present Study

In Sec. 2 we begin with an introduction to our sample, provide a summary of the observations, and detail our data reduction. This includes a description of a new iterative data reduction scheme designed to mitigate problems affecting the reconstruction of maps of weak extended emission. Section 3 provides a first discussion of the source properties and an overview of the source identification and quantification strategies. YSO properties from supplemental data are derived in Sec. 4. The main discussion of the data follows in Sec. 5, where we in particular study the structure and evolution of dense cores in general (Sec. 5.3), YSO cores (Sec. 5.4), and VeLLOs (Sec. 5.5). We summarise our study in Sec. 6. Appendix A discusses the standard dust emission properties adopted by the c2d collaboration to derive the mass distribution from observed dust emission maps.

2. Sample, Observations, and Data Reduction

2.1. Sample Selection

Our sample of 38 cores (Table 1) is drawn from the initial target list of the c2d Spitzer survey of isolated dense cores (Evans et al. 2003). This list contains dense cores within about 400 pc from the sun that are smaller than $\approx 5'$ and were mapped in dense gas tracers before the start of the c2d surveys. These cores are nearby enough to allow for the detection of intrinsically faint embedded sources. Their small apparent size allows them to be mapped in a reasonable time. This sample was drawn from the compilations and surveys of Jijina et al. (1999, for NH_3 maps), Lee et al. (2001, for CS and N_2H^+ maps), and Caselli et al. (2002, for N_2H^+ maps), and completed by adding individual cores. Due to time constraints not all sources in our sample were finally observed by Spitzer as part of c2d. Some further cores have or will be covered as part of the Spitzer Gould Belt survey¹, or have been covered in other programs (see Table 1 for details).

The initial c2d target list contains about 150 cores. At the start of the c2d survey, MAMBO was the most efficient bolometer camera available for sensitive mapping of large fields. Therefore, those cores in this list that were expected or known

¹ <http://www.cfa.harvard.edu/gouldbelt/index.html>

to have faint or extended dust continuum emission, or both, and are visible from Spain, were mapped by MAMBO. The other cores were observed in other surveys with SCUBA on the JCMT (Young et al. 2006a), SHARC II on the CSO (Wu et al. 2007), and with SIMBA on the SEST (Brede et al., in prep.). We obtained usable MAMBO data for 38 cores, which are listed in Table 1. Of these cores 21 are starless to our present knowledge, 4 contain VeLLO candidates (out of which 2, those in L1014 and L1521F, can be considered proven VeLLOs), and 13 contain YSOs (see Sec. 4.1 for a discussion of the association between YSOs and dense cores). Spitzer data is available for 32 cores (i.e., 3/4) of the MAMBO sample (see Table 1 for Spitzer observation references). The MAMBO sample covers 25 out of the 82 cores observed by c2d, and thus roughly 1/3 of the total c2d sample. In total 13 out of the 17 YSO and VeLLO candidate cores observed by us using MAMBO were targeted by Spitzer. However, only for 8 of these (less than half) there is c2d data and therefore homogeneous Spitzer photometry.

The observed cores reside in very different environments, ranging from regions of isolated low-mass star formation, like Taurus, over more turbulent regions, like the Cyg OB7 molecular cloud complex and the Cepheus Flare, to the high-mass star-forming site of Orion. In this respect the c2d MAMBO sample does not constitute a homogeneous sample, but a cross section of the different star-forming clouds in the solar neighborhood. Correspondingly our sample includes cores from near (≈ 100 pc) to intermediate (≈ 400 pc) distances.

2.2. Observations

Continuum observations of the 1.2 mm thermal dust emission were done with the IRAM 30m-telescope on Pico Veleta (Spain) using the 37-receiver MAMBO-1 (projected array diameter of 120'') and 117-receiver MAMBO-2 bolometer (240'' diameter) cameras of the Max-Planck-Institut für Radioastronomie (Kreysa et al. 1999). A total of 122 usable maps was taken between the summer of 2002 and the winter of 2003/2004 in the framework of a flexible observing pool (Table 2). Only 6 maps were acquired using the MAMBO-1 array. The weather conditions were good, with zenith optical depths between 0.1 and 0.3 for most of the time, and above this for $\approx 20\%$ of the time. Some of the maps were affected by clouds. All but 13 maps (i.e., 11%) were taken at an elevation above 40°. This yields typical line-of-sight optical depths much below 0.5. Two maps are affected by strong anomalous refraction (Altenhoff et al. 1987; one map on the southern part of L1041-2, one map on L1148).

The beam size on the sky was 11'', and the effective frequency 250 GHz with half sensitivity limits at 210 and 290 GHz. Pointing and focus position were usually checked before and after each map. The pointing and focus corrections were usually below 3'' and 0.3 mm, respectively. The zenith optical depth was typically measured with a skydip at least once within an hour from start or end of a map. The sources were observed with the standard on-the-fly technique, where the telescope secondary was chopping by $\approx 40''$ to $\approx 70''$ at a rate of 2 Hz parallel to the scanning direction of the telescope. The telescope was constantly scanning in azimuth for up to 90 s at a speed of 6 to 8'' s⁻¹ before turning around, except for one map of L1521B-2 for which the telescope moved in azimuth and elevation (then using the "rotated" chopping secondary). Where possible, each source was mapped with varying scanning directions (in equatorial coordinates) and chop throws. Several times per week Mars and Uranus were observed for absolute flux calibration. "Secondary" calibrators of constant but not a priori known

Table 2. MAMBO map details. For each core the products 'number of maps' \times 'array type' list how often a core was observed with which array ('37' for MAMBO-1 and '117' for MAMBO-2). Several products are given if a dense core was observed with both arrays. The last column lists the minimum noise level in a map after smoothing to 20'' resolution.

c2d Name	MAMBO Maps	Minimum Noise Level mJy per 11'' beam
L1355	2 \times 117	1.6
L1521B-2	5 \times 117	1.1
L1521F	2 \times 117	2.0
L1521-2	4 \times 117	1.3
L1524-4	2 \times 117	1.4
B18-1	4 \times 117	1.1
TMC-2	4 \times 117	0.9
B18-2	2 \times 117	1.3
B18-4	3 \times 117 ^a	1.1
B18-5	3 \times 117 ^a	1.1
TMC-1C	6 \times 117	1.2
TMC-1	6 \times 117	1.7
L1507A	5 \times 117	1.6
L1582A	3 \times 117	1.3
IRAS05413	3 \times 117	1.2
L1622A	7 \times 117	1.1
L183	4 \times 117	1.4
L438	2 \times 117	1.2
L492	3 \times 117	0.8
CB188	1 \times 37, 2 \times 117	0.8
L673-7	2 \times 117	1.3
L675	1 \times 37, 2 \times 117	0.9
L1100	1 \times 37, 2 \times 117	1.3
L1041-2	4 \times 117	1.4
L1148	5 \times 117	1.1
L1155E	2 \times 117	1.5
L1082C-2	2 \times 117	1.8
L1082C	2 \times 117	1.5
L1082A	4 \times 117	1.1
L1228	3 \times 117	1.3
Bern48	1 \times 37, 1 \times 117	1.0
L1172A	2 \times 117	1.5
L1177	1 \times 117	1.3
L1021	3 \times 117	1.0
L1014	2 \times 37	1.3
L1103-2	3 \times 117	1.4
L1251A	3 \times 117	1.2
L1197	6 \times 117	0.9

Notes: a) B18-4 and B18-5 were observed together in one field.

flux density were observed every few hours. The scatter in their retrieved flux densities suggests a relative map-to-map calibration uncertainty < 15%, suggesting an absolute uncertainty of order 20%.

Part of the data were already presented by Crapsi et al. (2004, for L1521F), Crapsi et al. (2005, for TMC-2 and L492), Young et al. (2004a, for L1014), and Schnee et al. (2007b, for TMC-1C). The raw data for these sources are included in this work and are partially complemented by additional maps².

² Some of these data was kindly provided by A. Crapsi.

Table 1. Dense cores covered by the c2d MAMBO survey. The table lists, from left to right, the core name adopted within the c2d collaboration, names for the cores adopted by other authors, the core distance, the type of the core (i.e., starless, YSO, or VeLLO), the approximate galactic environment of the dense core, and whether Spitzer data is available for the core. The last column gives a rough description of the morphology of the subcores (i.e., extended substructures; see Sec. 3.2) within each core using the c2d standard morphology keywords (Enoch et al. 2006; see Sec. 3.3 for a description).

c2d Name	Other Names	Distance ^a pc	Type ^b	Region ^c	Spitzer Data ^d	Morphology Keywords ^e
L1355		200 ± 50 ¹	s.l.	Cepheus Flare	c2d	elongated, extended
L1521B-2	B217B	140 ± 10 ²	s.l.	Taurus	c2d	multiple, elongated, extended
L1521F		140 ± 10 ²	Ve.	Taurus	c2d	elongated, extended
L1521-2		140 ± 10 ²	s.l.	Taurus	c2d	round, extended
L1524-4		140 ± 10 ²	s.l.	Taurus	c2d	multiple, round to elongated, extended
B18-1	TMC-2A	140 ± 10 ²	s.l.	Taurus	c2d	multiple, round to elongated, extended
TMC-2	L1529	140 ± 10 ²	s.l.	Taurus	c2d	multiple, elongated, extended
B18-2		140 ± 10 ²	s.l.	Taurus	c2d	multiple, elongated, extended
B18-4	TMC-3	140 ± 10 ²	YSO	Taurus	IRAC, MIPS	multiple, elongated, extended
B18-5		140 ± 10 ²	s.l.	Taurus	c2d	multiple, elongated, extended
TMC-1C	B220	140 ± 10 ²	s.l.	Taurus	c2d	multiple, elongated, extended
TMC-1	L1534	140 ± 10 ²	s.l.	Taurus	c2d	multiple, elongated, extended
L1507A		140 ± 10 ²	s.l.	Taurus	c2d	multiple, round to elongated, extended
L1582A	B32	400 ± 40 ³	YSO	λ Orionis	IRAC, MIPS	multiple, elongated, extended
IRAS05413	HH212-mm	450 ± 50 ⁴	YSO	Orion B	IRAC, MIPS	multiple, round to elongated, extended
L1622A		450 ± 50 ⁴	s.l.	Orion East	IRAC, MIPS	multiple, elongated, extended
L183	L134N	110 ± 10 ⁵	s.l.	north of Ophiuchus	IRAC, MIPS	multiple, round to elongated, extended
L438	CB119	270 ± 50 ⁶	s.l.	Aquila Rift	c2d	round, extended
L492	CB128	270 ± 50 ⁶	s.l.	Aquila Rift	c2d	elongated, extended
CB188	L673-1	300 ± 100 ⁷	YSO	Aquila Rift, Cloud B	c2d	elongated, extended
L673-7		300 ± 100 ⁷	Ve.	Aquila Rift, Cloud B	c2d	multiple, round to elongated, extended
L675	CB193	300 ± 100 ⁷	s.l.	Aquila Rift, Cloud B	c2d	elongated, weak
L1100	CB224	400 ± 50 ⁸	YSO	northern Cyg OB7		elongated, extended
L1041-2		400 ± 50 ⁸	YSO	northern Cyg OB7		multiple, round to elongated, extended
L1148	L1147	325 ± 25 ⁹	Ve.	Cepheus Flare	c2d	multiple, elongated, extended
L1155E	L1158	325 ± 25 ⁹	s.l.	Cepheus Flare	c2d	multiple, elongated, extended
L1082C-2		400 ± 50 ¹⁰	s.l.	Cyg OB7		elongated, extended
L1082C		400 ± 50 ¹⁰	YSO	Cyg OB7		elongated, extended
L1082A	B150	400 ± 50 ¹⁰	YSO	Cyg OB7		multiple, round to elongated, extended
L1228		200 ± 50 ¹¹	YSO	Cepheus Flare	c2d	round, extended
Bern48	RNO129	200 ± 50 ¹¹	YSO	Cepheus Flare	c2d	round, extended
L1172A		288 ± 25 ⁹	YSO	Cepheus Flare	IRAC, MIPS	multiple, round, extended
L1177	CB230	288 ± 25 ⁹	YSO	Cepheus Flare	IRAC	round, extended
L1021		250 ± 50 ¹²	s.l.	Cyg OB7	c2d	elongated, extended
L1014		250 ± 50 ¹²	Ve.	Cyg OB7	c2d	elongated, extended
L1103-2	L1106	250 ± 50 ¹²	s.l.	Cyg OB7		elongated, extended
L1251A		300 ± 50 ¹³	YSO	Cepheus Flare	c2d	multiple, round to elongated, extended
L1197		300 ± 50 ¹⁴	s.l.	Cepheus Flare	c2d	elongated, extended

Notes:

a) Standard c2d distances (Bourke, priv. comm.), derived by reddening methods or association (in position-velocity space) to objects of known distance. The individual references are: [1] Obayashi et al. (1998), via association; [2] Kenyon et al. (1994); [3] Murlin & Penston (1977); [4] Genzel & Stutzki (1989), via association to L1630; [5] Franco (1989); [6] Straizys et al. (2003); [7] Herbig & Jones (1983), via association to L673; [8] Dobashi et al. (1994), and association to L1041; [9] Straizys et al. (1992), and association with L1172; [10] via reddening, following Bourke et al. (1995); [11] Kun (1998); [12] Pagani & Beart de Boisanger (1996), via association to B164; [13] Kun & Prusti (1993); and [14] Yonekura et al. (1997), via association to L1192/L1200.

b) The abbreviations mark starless cores ('s.l.:', these have no known star within the core boundaries defined in Sec. 3.2), YSO cores ('YSO': YSOs within the core boundaries), and VeLLO cores ('Ve.': VeLLOs within the core boundaries). The cores L1521-2, B18-1, TMC-1, and L1622A are excluded from the YSO category since the YSOs are off the main core body. See Sec. 4.1 for a discussion of the association between YSOs and dense cores.

c) The designation of regions roughly follows Dame et al. (1987), Maddalena et al. (1986), Yonekura et al. (1997), and Dobashi et al. (1994).

d) Cores with data from the c2d project (Evans et al. 2003) are labeled 'c2d'. For other cores existing Spitzer imaging data is indicated in the table, and the Spitzer program numbers and PIs are: GO 3584 (Padgett) and GO 20302 (Andre) for B18-4; GO 20339 (Stauffer) for L1582A; GO 3315 (Noriega-Crespo) and GTO 47 (Fazio) for IRAS05413; GTO 47 (Fazio) for L1622A; GTO 94 (Lawrence) and GTO 53 (Rieke) for L183; L 30574 (Allen) and IOC 717 (Rieke) for L1172A; and GTO 124 (Gehrz) for L1177.

e) The c2d standard keywords are adopted from the c2d Bolocam survey by Enoch et al. (2006). See Sec. 3.3 for a description.

2.3. Data Reduction

2.3.1. Classical Limitations & A new Strategy

The reduction of bolometer data for extended sources is still an evolving art, in particular when dealing with faint emission. The basic problem is that the brightness of the sky usually exceeds the intensity of the astronomical sources by 2 to 4 orders of magnitude (e.g., at 1.2 mm wavelength the intensity from a 300 K atmosphere of optical depth ≥ 0.1 exceeds the intensity from interstellar dust at 10 K with an H_2 column density $\leq 10^{23} \text{ cm}^{-2}$ by a factor ≥ 640). The sky brightness (and if possible also its rapid fluctuations known as “skynoise”, that contribute to the noise) thus has to be subtracted during the data reduction. This subtraction unfortunately can introduce artifacts to the derived maps.

Specifically, classical data reduction algorithms filter a significant fraction of the source flux when sources have a size comparable to the size of the bolometer array (relevant when subtracting skynoise), a size similar to an individual bolometer map (i.e., before mosaicing; relevant when subtracting the mean sky brightness as, e.g. the minimum intensity in the map), or both. (Note that these fundamental problems also affect maps from modern total-power bolometers like LABOCA³, SCUBA-2⁴, and Bolocam⁵. A detailed analysis of this problem for Bolocam has been given by Enoch et al. (2006).) This is the case for a large fraction of the sources studied in our sample. We therefore implement an innovative data reduction scheme that partially mitigates classical reconstruction problems.

The central element of our data reduction algorithm is the subtraction of the expected signal due to the astronomical source (based on a source model) from the raw data before determining and then subtracting from it the mean sky brightness and skynoise. This processed raw data is then turned into a map. The sum of this “residual” map (since source emission is subtracted) and the source model yields an improved source model that can be used in further iterations. This approach has the advantage that the resulting source model suffers from lesser artifacts due to skynoise and sky subtraction than if no existing knowledge of the source structure was used during the subtraction. The initial source model for the iterative scheme comes from a map created using classical (i.e., biased) algorithms. It can be shown analytically that, in the ideal case without noise, sources much larger than in the classical approach can be recovered. In our iterative scheme, the residual intensities decrease with a factor 2^{-n} , where n is the number of iterations. To be specific, full recovery of the source structure requires the source diameter, d_{source} , to be smaller than the effective map size,

$$d_{\text{source}} < \ell_{\text{scan}} + \ell_{\text{chop}}, \quad (1)$$

where ℓ_{scan} and ℓ_{chop} are (following IRAM terminology) the scan length and the chop throw (of the secondary mirror), respectively. Slightly larger sources can still be recovered, but convergence is slower than 2^{-n} . This size can be increased by mosaicing. Classical methods, on the contrary, require for full recovery (with d_{array} being the array diameter)

$$d_{\text{source}} < \ell_{\text{scan}} + \ell_{\text{chop}} - d_{\text{array}} \quad (2)$$

when not subtracting skynoise, and have the additional constraint

$$d_{\text{source}} < d_{\text{array}} \quad (3)$$

if doing so. Mosaicing will furthermore bias intensities. Experiments with simulated raw data including noise show that the simulated maps are consistent with the above ideal analysis.

In a formal sense, the improvements due to our approach thus mean that observations are only limited by Eq. (1), while conventional approaches are limited by Eqs. (2) and (3). The gain in mapping parameter space is illustrated in Fig. B.1 in Appendix B. There, we also present a direct comparison between maps derived using conventional methods to those from our approach (Fig. B.2).

For typical MAMBO map sizes $\ell_{\text{scan}} = 360''$ to $540''$ and chop throws $\ell_{\text{chop}} = 60''$ sources with diameters $d_{\text{source}} < 6'$ to $9'$ can thus be recovered without significant bias when using our new approach. For comparison, when using the larger MAMBO-2 array, classical algorithms would only recover sources with a diameter $d_{\text{source}} < 3'$ to $6'$, where skynoise filtering sets the additional constraint that $d_{\text{source}} < 4'$ even for much longer scan lengths.

2.3.2. Implementation

Our iterative data reduction scheme is implemented using the MOPSI software package, which is developed and maintained by R. Zylka (IRAM Grenoble); for L1521B-2 we used MOPSI, an upgrade of MOPSI also able to handle data obtained using the “rotated” wobbler. These packages provide subroutines to estimate and remove the correlated skynoise, to reconstruct maps from chopped bolometer data using the EKH algorithm (Emerson et al. 1979), to simulate chopped intensity difference maps for given source models, and many other tools. These routines are combined to carry out our iterative data reduction scheme.

During the first iteration no skynoise is removed. The chopped intensity difference maps derived for each epoch are co-added and then restored using EKH reconstruction. In the resulting map the area with emission is then marked by hand. The intensity for the area outside the area with emission is set to zero, as is done for all pixels with negative intensity inside the area with emission. The modified intensity map is then smoothed to an effective resolution of $20''$, except for visually selected areas with strong emission, where the data is smoothed to $14''$ resolution. This smoothing increases the signal-to-noise ratio for emission more extended than the beam. This map is then taken as the source model for the second iteration.

In the further iterations the simulated chopped intensity difference map for the source model is first subtracted from the raw data for every single observation. Then the correlated skynoise is estimated and subtracted in these residual maps. We use a correlation exclusion radius of $50''$ for all sources with data from the 37 receiver MAMBO-1 camera (i.e., for each array receiver a neighborhood of $50''$ radius is excluded when estimating skynoise, since this reduces intensity biases), and $100''$ otherwise. To remove offsets due to sky intensity and instabilities, a constant intensity (i.e., a baseline of order 0) is then subtracted from each receiver signal for every scan lag. A co-added intensity map including all observations is then derived using EKH restoration. This map is then added to the source model, and a source model for the next iteration is derived as done above. In total 10 iterations are performed. Note that the smoothing of the source model does not reduce the resolution in the reconstructed maps: the source map derived at the end of every iteration is corrected for differences between the actual and model source structure due to smoothing since these show up in the residual maps finally added to the source model.

³ <http://www.apex-telescope.org/bolometer/laboca/>

⁴ <http://www.jach.hawaii.edu/JCMT/continuum/scuba2.html>

⁵ <http://casa.colorado.edu/~aikinr/research/bolocam.html>

The final maps presented here are usually smoothed to an effective resolution of $20''$, though they are available for resolutions down to $11''$. This smoothing improves the signal-to-noise level for emission more extended than the beam. In order to facilitate comparison with maps of different resolutions the data are calibrated in mJy per $11''$ beam. Further weight maps give the variation of the effective integration time per pixel across the map. They are calculated during the data reduction and used to calculate noise maps. The noise increases with increasing distance from the map center due to a decrease in exposure time towards the map boundaries.

3. Results

3.1. Maps

Figure 1 presents the intensity maps of the dense cores covered by our MAMBO observations. The minimum noise level in the maps ranges from 0.8 to 2.0 mJy per $11''$ beam and is listed for each source in Table 2. To facilitate comparison, all maps are drawn with the same contouring levels and to the same angular scale.

In most sources the maps reveal extended emission on scales of several arc-minutes, and in many fields the presence of compact emission with a full width at half maximum of only a few beams. Compared with many other bolometer surveys that often detect only the most prominent intensity peaks, our MAMBO maps are very rich in structure.

In spite of our careful data reduction, some maps are still affected by artifacts such as stripes in the scanning direction and extended areas of negative intensities. Sources significantly affected by this are given lesser weight in our analysis. These are in particular objects with obvious scanning stripes in their boundaries (e.g., L183 C4; see below for object names), i.e., series of intensity peaks in the scanning direction separated by the chop throw, those located at map boundaries (e.g., L183 C6), or with a low intensity contrast to the surrounding at the object boundary (e.g., L1082C-2 C1; often due to artifacts).

[The journal article will be accompanied by the maps in FITS format.]

3.2. Source Identification and Quantification

The MAMBO maps reveal extended emission and compact emission peaks with no direct correspondence between these. We therefore separately identify and quantify extended features, which we term ‘subcores’, emission peaks in these subcores, and additional ‘significant peaks’ that fulfill some significance criterion and are not necessarily located within the subcore boundaries.

For some properties it is not possible to derive their uncertainties by Gaussian error propagation. In these cases we run Monte-Carlo simulations with artificial noise with properties identical to the actual one to estimate the uncertainties. Uncertainties are then derived as the standard deviation of the derived values. To reduce the noise level for the extended emission, all quantities derived for the cores and peaks are derived from maps smoothed to $20''$ resolution unless noted otherwise.

3.2.1. Extended Structures

Identification Our source identification method aims at a formal definition of what a human investigator would intuitively iden-

tify as a source. Our criteria are therefore not mathematically exact, but adopted from a series of trial-and-error experiments.

To identify sources we generate signal-to-noise ratio (SNR) maps for a beamsize of $20''$, which are then smoothed to a spatial resolution of $60''$. Regions above an SNR of 2 in these maps are taken as source candidates. Obvious artifacts at the rim of the maps are excluded. The remaining area above an SNR of 2 is then hand-divided into ‘subcores’. For this we search the $60''$ SNR maps for saddle points and draw core boundaries by following the gradient. This scheme is conceptually similar to, but not identical with, the “CLUMPFIND” algorithm by Williams et al. (1994). Our scheme thus assigns all emission above an SNR of 2 to some ‘subcore’.

Quantification Table 3 lists general information on the identified subcores. For each subcore we list the centroid position, defined as the mean position of the pixels in each subcore, where the pixels are not weighted by their intensity. The quoted uncertainties reflect the influence of statistical noise, while systematic contributions are not folded in. For each field mapped the subcores are labeled by a ‘C’, followed by a number in order of increasing right ascension. In the tables a star marks those cores associated with a YSO (see below). Cores with uncertain properties due to an unreliable reconstruction are marked by square brackets.

We then list the area assigned to the subcore, A , and the corresponding effective radius,

$$r_{\text{eff}} = (A/\pi)^{1/2}. \quad (4)$$

Furthermore, we derive the flux densities, F , and the corresponding masses, M , for the total subcore’s area (subscripts ‘tot’) and for the area above 50% of the peak intensity for the respective subcore (subscripts ‘50%’). The masses are derived from the flux densities as described in Sec. 3.2.3. Finally, Table 3 lists the maximum SNR for each subcore, $S_{\text{max}}^{\text{beam}}$. The uncertainties of F_{tot} and M_{tot} are derived by Gaussian error propagation of the measured noise level. For $F_{50\%}$ and $M_{50\%}$ the uncertainties are estimated by the Monte-Carlo experiments described above.

Table 4 lists geometrical information on the identified cores. This is done by fitting ellipsoids to the area above 50% of the peak intensity for the respective core (no weighting by intensity is applied)⁶. We give the major and minor axis, a and b , their ratio, and the position angle (east of north). The filling factor, f , gives the fraction of the fitted ellipse filled with emission above 50% peak intensity. Low filling factors indicate cases in which ellipses are a bad fit to the observed intensity distributions. We also list the effective diameter for the area above 70% of the peak intensity, $r_{70\%}$ (Crapsi et al. 2005). No attempt has been made to separately handle subcores in which the emission from two or more peaks contributes to $r_{70\%}$. In these cases $r_{70\%}$ is overestimated by an uncertain amount.

3.2.2. Peaks

Identification In order to quantify all intensity peaks in our maps we study the peak position of every identified subcore. In addition we search each map manually for ‘significant peaks’. These have an SNR of at least 4 and can be spatially separated from already identified peaks. To identify them we search the map for local intensity peaks with an $\text{SNR} \geq 4$ and draw the

⁶ This is implemented by using the IDL routine FitEllipse by David Fanning.

surrounding contour at the peak intensity minus three times the local noise level. Such a peak is taken to be significant if no brighter peak is situated in this contour. In the area outside identified cores we also require that there is also no fainter local peak within the contour. This additional restriction excludes most artifacts.

Quantification Peak properties are listed in Table 5. The quoted uncertainties reflect the influence of statistical noise, while systematic contributions are not folded in. For each mapped field peaks are labeled by a ‘P’, followed by a number in order of increasing right ascension. Uncertain peaks, which are not well reconstructed, are marked by square brackets. These were identified by searching the maps for peaks close to map boundaries, and those affected by scanning stripes.

Besides the peak position we give the subcore to which the peak belongs, if applicable. The peak intensity, F_{\max}^{beam} , is listed besides the corresponding peak H_2 column density and visual extinction, $N(\text{H}_2)$ and A_V . These are derived using the c2d standard assumptions on dust properties, as outlined in Appendix A, but they are only listed for starless cores for which there is no internal heating. In YSO cores the dust temperature exceeds 10 K and needs to be calculated separately for each source (Sec. 3.2.3). Also given are the flux density and the corresponding mass within an aperture of 4 200 AU radius, $F_{4200\text{AU}}$ and $M_{4200\text{AU}}$, as derived in Sec. 3.2.3. This aperture of constant physical diameter is a better measure of the mass distribution than the central column density since, for close enough sources, beam smearing does not play a role. The specific radius of 4 200 AU is somewhat arbitrary; Motte & André (2001) used it before, given that it matches $30''$ at the distance of Taurus (≈ 140 pc) and is about the radius of an envelope’s volume available for YSO formation (Sec. 5.3.3). We finally list the flux density for the c2d standard apertures of $20''$, $40''$, $80''$, $120''$ diameter (e.g., Young et al. 2006a and Wu et al. 2007). In deviation to most other parts of this work the flux densities for the apertures are derived from unsmoothed maps since the smoothed maps sometimes have a resolution comparable to the aperture size.

3.2.3. Mass and Column Density Estimates

Mass and column density estimates for starless cores are derived from the observed flux densities assuming the c2d standard dust emission properties, i.e., a dust temperature of 10 K and an opacity of $0.0102 \text{ cm}^2 \text{ g}^{-1}$ (per gram of ISM) at MAMBO’s effective observing wavelength. Appendix A presents a detailed discussion of the conversion between mass and dust emission. The related discussion of uncertainties in temperature and dust opacities suggest a systematic uncertainty for mass estimates of an order of a factor two. Dust near YSOs is, however, heated by the YSO radiation, and for later YSO stages likely to be more coagulated than interstellar dust. Therefore, we adopt higher dust temperatures and opacities when deriving masses for YSO cores. The temperature gradients also prevent us from deriving meaningful estimates of the peak column density of YSO cores; therefore we do not quote values.

The dust temperature near YSOs can be estimated from analytic models of temperature profiles for YSO envelopes cooling via dust emission. For opacities with power-law dependence on wavelength, $\kappa \propto \lambda^{-\beta}$, where β is the emissivity spectral index,

the dust temperature profile in a YSO envelope only heated radiatively by the star is

$$T_{\text{d}}^{\text{rad}}(r) = 38.4 \text{ K} \left(\frac{r}{100 \text{ AU}} \right)^{-q} \left(\frac{L}{L_{\odot}} \right)^{q/2}, \quad (5)$$

where $q = 2/(4 + \beta)$, L is the luminosity, and r is the distance from the star (Terebey et al. 1993). The numerical values hold for $\beta = 1$, which is consistent with observations (e.g., Belloche et al. 2006) and assumed in the following. Rearrangement allows for an estimate of the radius at a particular dust temperature,

$$r^{\text{rad}}(T_{\text{d}}) = 2890 \text{ AU} \left(\frac{T_{\text{d}}}{10 \text{ K}} \right)^{-1/q} \left(\frac{L}{L_{\odot}} \right)^{1/2}. \quad (6)$$

However, in absence of nearby stars, the interstellar dust is heated by the interstellar radiation field and in collisions with gas (which is heated by cosmic rays and the UV-part of the interstellar radiation field), which produces a typical equilibrium temperature of order 10 K (e.g., Goldsmith 2001; see Evans et al. 2001, Galli et al. 2002, and Young et al. 2004b for actual core temperature models). The dust temperature cannot drop below this value, so that

$$T_{\text{d}}(r) = \max(10 \text{ K}, T_{\text{d}}^{\text{rad}}[r]). \quad (7)$$

For this temperature profile Belloche et al. (2006) derive the mass-weighted dust temperature. This assumes optically thin dust emission, which applies to the majority of the mass. Only the densest and hottest parts of an envelope might be optically thick, which leads to an insignificant bias towards slightly overestimated average dust temperatures. For this calculation we assume the density profile in a subcore to be roughly described by a power-law, i.e. $\varrho \propto r^{-p}$, where ϱ is the density and r is the distance from peak center. Then the mass-weighted dust temperature within an aperture of radius R is

$$\langle T_{\text{d}} \rangle = \begin{cases} \frac{3-p}{3-q-p} T_{\text{d}}^{\text{rad}}(R), & \text{if } T_{\text{d}}^{\text{rad}}(R) \geq 10 \text{ K}, \\ \left(\frac{q}{3-p-q} \left[\frac{r^{\text{rad}}(10 \text{ K})}{R} \right]^{3-p} + 1 \right) \cdot 10 \text{ K}, & \text{otherwise.} \end{cases} \quad (8)$$

For YSO peaks and subcores we use this average temperature to derive masses from the flux densities of the whole subcore, of the area above 50% peak intensity, and of an aperture of 4 200 AU radius. In these cases the aperture radius R is set to be the effective core radius of the whole core, or the geometric mean of the major and minor axis at 50% peak intensity, or 4 200 AU, respectively. We assume a power-law exponent of $p = 2$ for the density profile (i.e., profile for a singular isothermal sphere; Shu 1977). The mean dust temperatures are thus overestimated for density profiles shallower than $\varrho \propto r^{-2}$. The YSO luminosities are taken to be identical to the bolometric luminosities derived in Sec. 4.2. For the VeLLOs associated with L1521F P1, L1148 P1 (a VeLLO candidate), and L1014 P1, however, we use the better constrained “internal luminosities” derived by Bourke et al. (2006), Kauffmann et al. (in prep.) and Young et al. (2004a). Given the observed luminosities, the temperatures assumed for class I sources are $(15 \pm 3) \text{ K}$, while for class 0 sources they reach from 10 to 24 K and 21 K is derived for the only class II source (in L1021 P1; see below for YSOs and their classes).

The uncertain density profile leads to an uncertain mass estimate. We consider a range in the exponent p from 2 to $3/2$, as expected for YSO envelopes (Shu 1977), in order to gauge the uncertainties in the mass estimate. This shows that the aperture averaged temperatures in power-law envelopes, and correspondingly the derived masses, are uncertain by 30% and less.

For the dust near class II YSOs we adopt an opacity of $0.02 \text{ cm}^2 \text{ g}^{-1}$ because of an expected enhanced coagulation (Motte & André 2001, Ossenkopf & Henning 1994). For the other YSO and starless cores we adopt the standard c2d opacity, which is $0.0102 \text{ cm}^2 \text{ g}^{-1}$ at MAMBO's observing wavelength.

Circumstellar disks might also contribute to the millimetre continuum emission. Their contribution to apertures with radii $\geq 4200 \text{ AU}$ is estimated to be $\lesssim 10\%$ for YSOs of the classes 0 and I (Motte & André 2001). The emission from the disks does therefore not significantly bias our envelope mass estimates for the youngest YSOs. Class II YSOs, in contrast, are not expected to have envelopes (e.g., André et al. 2000 and references therein); their emission is dominated by compact ($\lesssim 1000 \text{ AU}$) disks with a temperature above the one estimated from Eq. (8). Our procedure will thus overestimate the mass for YSOs with significant disk emission.

3.3. Overview of Source Properties

We use the morphology keywords adopted by Enoch et al. (2006) to describe our maps. These are summarised in Table 1 and can be employed to compare the dense core morphologies revealed by our maps with those found in other c2d bolometer surveys.

All dense cores that were observed are detected in our maps, i.e., the maximum SNR in the map is at least 4. For one source only 'weak' emission is detected, meaning a peak SNR equal to or below 5; all other sources are brighter. In total 21 cores (55% of all cores) have at least two peaks separated by less than $3'$, and we consider them to be 'multiple'. All cores are 'extended', as they contain at least one subcore with an equivalent radius exceeding $30''$. We take all subcores with a major-to-minor axis ratio exceeding 1.2 to be 'elongated', and the others to be 'round'. Then 6 cores (16%) only contain round subcores, 21 cores (55%) only contain elongated subcores, and 9 cores (24%) contain both round and elongated subcores.

Figure 3 gives an overview over the sizes, masses, column densities, and ellipticities of well reconstructed subcores. These have typical values in the range $(1 \text{ to } 6) \cdot 10^4 \text{ AU} = 0.05 \text{ to } 0.30 \text{ pc}$ for the effective radius, $0.5 \text{ to } 20 M_{\odot}$ for the subcore masses, $0.1 \text{ to } 1.0 M_{\odot}$ for the mass within 4200 AU from the peak, and major-to-minor axes ratios at 50% peak intensity ranging from 1 to about 4. Implications from these properties for the physical state and evolution of dense cores and YSOs are discussed in Sec. 5.

4. Supplemental YSO Data

For the c2d MAMBO survey to be fully exploited, it needs to be complemented with information on the YSOs covered by the maps. Most of our analysis below is based on IRAS data since c2d finally observed only half of the YSO (& VeLLO) cores in our sample (i.e., 8 out of 17) and a homogeneous characterization is not possible based on c2d Spitzer data only. Also, we only use c2d photometry for Spitzer source characterization to guarantee homogeneity, implying that some images in the Spitzer archive cannot be used for the present study. All YSOs visible in Spitzer images are, however, either characterized by IRAS or Spitzer, with the singular exception of a Spitzer source in L1582A not covered by c2d data and not detected by IRAS.

Table 7. IRAS sources in the MAMBO maps that are not detected as MAMBO emission peaks. For every core in the c2d MAMBO survey the table lists sources from the IRAS Point Source Catalogue and the IRAS Faint Source Catalogue (preceded by an 'F'), and the subcores in which the IRAS sources are located, if applicable. Objects from the IRAS Point Source and Faint Source catalogues present in both catalogues are connected. The last column gives the spectral index between 12 and $25 \mu\text{m}$ wavelength.

Core	IRAS Source	Asso.	$\alpha_{12}^{25 \mu\text{m}}$
L1521-2	F04262+2654	C1	0.27 ± 0.43
L1524-4	04274+2420		-0.85 ± 0.27
	F04274+2420		-0.83 ± 0.19
B18-1	04292+2427		< -1.5
	F04291+2427		< -1.9
TMC-2	04294+2413		-0.9 ± 0.15
	F04294+2413		-0.89 ± 0.11
B18-4	04326+2405	C1	< -1.68
	F04326+2405		< -0.75
TMC-1C	04380+2553		-0.51 ± 0.15
	F04380+2553		-0.76 ± 0.12
TMC-1	F04383+2549		< -1.12
	04392+2529		
L1582A	F05290+1229		-0.51 ± 0.17
L1622A	05517+0151		-2.14 ± 0.16
	F05517+0151		-2.25 ± 0.15
	05519+0148	[C2]	
	05519+0157		
L438	18116-0707		< -1.33
L492	18130-0341		
	18132-0350		-1.82 ± 0.15
CB188	19180+1127		< -1.31
L675	19217+1103		-1.81 ± 0.25
L1148	20395+6714		
	20410+6710 ^a	C2	
L1228	F20598+7728		-0.26 ± 0.34
L1103-2	21399+5632		> -1.47
L1251A	F22282+7454		< -2.54

Notes: a) Probably an artifact since no corresponding Spitzer source exists.

4.1. Associated IRAS, 2MASS, and Spitzer Sources

Table 7 lists sources from the IRAS Point Source Catalogue (PSC; Beichman et al. 1988) and IRAS Faint Source Catalogue (FSC; Moshir & et al. 1990) not associated with intensity peaks in the MAMBO maps, and Table 8 lists those that are associated. The sources are considered to be associated with subcores and peaks detected by MAMBO if the separation between an IRAS source and a MAMBO subcore or peak is less than the uncertainty of the separation at the 2σ level (i.e., the IRAS uncertainty ellipse plus the MAMBO pointing error). These sources are most likely physically associated with the dense cores and are assumed to be young stars.

We include IRAS sources of any quality. This in principle could lead to considerable bias of our sample, since also extragalactic sources and late type stars would be picked up by these criteria. However, only a single IRAS source projected onto well detected emission is not detected as a MAMBO intensity peak (i.e., in L1521-2 C1; see Table 7); all other IRAS sources that lie within subcore boundaries but are not detected as MAMBO peaks are either detected as extensions in the MAMBO intensity contours (in B18-4 C1), projected onto noisy parts of a MAMBO

Table 8. Properties of MAMBO-detected IRAS sources. For every core in the c2d MAMBO survey the table lists dust emission peaks and, if applicable, the related subcore associated with an IRAS source (Sec. 4.1 discusses the identification of associated sources; FSC sources are preceded by an ‘F’). Associated 2MASS sources are listed too. The table further lists the spectral index between 12 and 25 μm wavelength, the bolometric temperature and luminosity, the submillimetre-to-bolometric luminosity ratio, the mass within a peak-centered aperture of 4 200 AU radius, and the infrared SED class.

Core	Asso.	IRAS Source	2MASS Source	$\alpha_{12\ \mu\text{m}}^{25\ \mu\text{m}}$	$T_{\text{bol}}^{\text{IRAS}}$ K	$L_{\text{bol}}^{\text{IRAS}}$ L_{\odot}	$L_{\text{submm}}^{\text{IRAS}}/L_{\text{bol}}^{\text{IRAS}}$	$M_{4200\text{AU}}^{\text{YSO}}$ M_{\odot}	Class
B18-1	[C2], [P5]	04292+2422	04321540+2428597	0.84 ± 0.13	< 602	> 1.09	> 0.014	> 0.179	I
B18-4	C1, P1	04325+2402 & F04292+2422	04353539+2408194	> 3.76	< 83	0.42 to 0.79	0.053 to 0.099	0.522 to 0.589	I
TMC-1C	P3	04385+2550 & F04385+2550	04413882+2556267	0.41 ± 0.13	> 596	0.23 to 0.47	0.007 to 0.015	0.042 to 0.047	I
TMC-1	C2, P2	04381+2540 & F04381+2540	04411267+2546354	1.52 ± 0.14	131	0.67 ± 0.02	0.043 ± 0.017	0.379 ± 0.010	I
IRAS05413	C2, P2	05412-0105 & F05411-0106	05434630-0104439	> 0.25	> 67	0.52 to 7.26	0.008 to 0.115	0.308 to 0.597	0
CB188	C3, P3	05413-0104	none	> -0.70	< 55	≈ 10.5	≈ 0.017	≈ 0.95	0
L1100	C1, P1	19179+1129	19201494+1135400	> 0.88	< 248	1.74 to 2.14	0.015 to 0.018	0.272 to 0.288	I
L1041-2	C1, P1	20355+6343 & F20355+6343	none	0.70 ± 0.18	< 103	1.22 to 2.13	0.023 to 0.041	0.445 to 0.515	I
L1148	C4, P4	20361+5733 & F20361+5733	none	> 3.12	< 60	3.91 to 5.07	0.025 to 0.033	0.900 to 0.966	0
L1082C	C1, P1	F20404+6712	20405664+6723047	> -0.07	> 110	0.06 to 0.40	0.023 to 0.165	0.115 to 0.146	I
L1082A	C1, P1	20503+6006 & F20503+6007	none	> 1.05	> 62	0.32 to 1.73	0.026 to 0.141	0.402 to 0.576	0
L1228	C1, P1	20520+6003	20531346+6014425	0.39 ± 0.20	< 198	1.00 to 2.49	0.018 to 0.044	0.388 to 0.491	I
L1177	C3, P5	20526+5958	none	< 119	< 119	0.84 to 1.36	0.038 to 0.061	0.538 to 0.602	I
L1228	C1, P1	20582+7724 & F20582+7724	20571294+7735437	0.35 ± 0.11	307	2.27 ± 0.04	0.035 ± 0.008	0.782 ± 0.007	I
Bern48	C1, P1	21004+7811 & F21004+7811	20591408+7823040	-0.17 ± 0.10	628	11.05 ± 0.20	0.008 ± 0.001	0.483 ± 0.003	I
L1172A	C2, P2	21017+6742 & F21017+6742	21022122+6754202	> -0.13	< 100	0.37 to 0.59	0.049 to 0.077	0.370 to 0.403	I
L1177	C1, P2	21169+6804 & F21168+6804	21173862+6817340	1.26 ± 0.27	< 127	2.50 to 3.32	0.038 to 0.051	1.030 to 1.114	I
L1021	P1	21197+5046	21212751+5059475	-0.82 ± 0.13	> 990	4.09 to 6.91	0.001 to 0.002	0.021 to 0.024	II
L1251A	C2, P3	22290+7458 & F22290+7458	22300004+7513578	> 0.68	> 88	0.12 to 0.75	0.033 to 0.216	0.284 to 0.380	I

map (in L1622A C2), or of dubious quality and discarded anyway (in L1148 C2).

The criterion of association is relaxed for IRAS05413 P2, L1100 P1, and L1082C P1. For these sources inconsistencies between the IRAS PSF and FSC indicate positional errors of order 1', and we associate them with neighboring MAMBO peaks since these would be unusually bright and compact for starless peaks. For IRAS 20410+6710, which is projected onto L1148 C2, our more sensitive Spitzer maps show no corresponding source in the MIPS bands. We therefore consider this IRAS source to be an artifact.

For those IRAS sources associated with dust emission peaks it is possible to significantly improve the accuracy of their position by adopting the position of the MAMBO peak. This then allows for a search of 2MASS counterparts of these sources. We do so by searching for 2MASS sources less than 10'' away from the MAMBO peak. If several 2MASS sources are found we assume the one closest to the MAMBO peak to be the counterpart. The identified counterparts are listed in Table 8. If no counterpart is found, 2MASS upper limits are taken to be similar to those of nearby 2MASS sources with upper limits.

This combined data yields a spectral coverage with data near 1 μm wavelength (from 2MASS), a well sampled range from 12 to 100 μm (from IRAS), and information at 1 200 μm (from MAMBO). For consistency with previous work (e.g., André et al. 1999 and Motte & André 2001), and to avoid problems of distance bias, we use dust emission flux densities for the 4 200 AU aperture to study the spectral energy distributions.

In Table 9 we also present a list of Spitzer point sources from the 3rd c2d data delivery⁷ associated with MAMBO dust emission peaks. To identify associated objects we search our maps for Spitzer sources that are detected as point sources at 24 μm wavelength, have a 24 μm flux ≥ 2 mJy, and are offset by less than 20'' from a dust emission peak. We use the 24 μm data for our search since in this band Spitzer reliably picks up sources with infrared emission apparently in excess of the photospheric emission.

The choice of the flux and offset cuts is guided by previous knowledge about sources in our sample. The 24 μm flux cut for our search must be ≤ 2 mJy, since manual inspection of our maps reveals YSOs of such flux in our sample (e.g., SSTc2d J223105.6+751337 in L1251A). The offset cut must be $\geq 10''$, larger than offsets recently observed for YSOs in our sample (L1014-IRS; see Huard et al. 2006). Using the c2d processed source catalogues (documented as part of c2d's 4th data delivery) for the area surveyed by the Spitzer Wide-Area Infrared Extragalactic survey (SWIRE; Lonsdale et al. 2003), with our criteria we expect to find 1.07 chance alignments between extragalactic background objects and one of the about 110 dust emission peaks in our MAMBO maps.

Table 10 furthermore gives a list of prominent YSOs detected in Spitzer data not taken by c2d, defined as previously known IRAS YSOs. This excludes sources in L1622A, since these are not well covered by our MAMBO maps. One source in L1582A that has apparent outflow nebulosity and was not detected by IRAS is also included. We cannot, however, associate a MAMBO peak to this star, and we therefore have to exclude it from the further analysis. Manual inspection of the images did not reveal further probable YSO candidates. No c2d photometry exists for these images, and the Spitzer source properties are not further discussed in the following, except when refining

Table 10. Prominent YSOs detected in Spitzer data not taken by c2d, and related IRAS sources, if existing.

Core	IRAS Counterpart
B18-4	04325+2402
L1582A ^a	none
IRAS05413	05412-0105 05413-0104
L1172A	21017+6742
L1177	21169+6804

Notes: a) MIPS source at 05 32 02.9, +12 31 05 (J2000.0)

Table 11. Cores in the c2d MAMBO survey with YSOs uncovered by c2d that were believed to be starless at the beginning of the c2d survey. Comments on outflows refer to jet-like extended ($\gg 1'$) features in IRAC images.

MAMBO Core	Comments
L1521F C1	VeLLO, Bourke et al. (2006)
L1582A C2 ^a	no c2d Spitzer data, possible outflow
L673-7 C1 ^a	VeLLO, Dunham et al., in prep.
L1148 C1	VeLLO, Kauffmann et al. 2005 and in prep.
L1014 C1	VeLLO, Young et al. (2004a)
L1251A C3 ^a	new class 0, prominent outflow
C4 ^a	new class 0, possible outflow

Notes: a) reported here for the first time

YSO positions (Sec. 5.4.6). Including the object in L1582A, the combined Spitzer data thus shows 7 YSOs in cores previously believed to be starless (Table 11). Four out of these (including the VeLLO candidate in L673-7) are reported here for the first time.

The data on the MAMBO-associated Spitzer sources is complemented by 2MASS data where possible. Given the nominal positional uncertainties, 2MASS sources within 2'' from Spitzer sources are assumed to be counterparts of these. For Spitzer sources without 2MASS counterparts upper limits to their flux densities in the 2MASS bands are derived from upper limits for nearby 2MASS sources not detected in all filters. The source emission is thus probed in the 1 to 70 μm wavelength range (by 2MASS and Spitzer; no c2d Spitzer data is available at 160 μm) and at 1 200 μm (from MAMBO for the 4 200 AU aperture).

Note that probably many more Spitzer sources are associated with the MAMBO cores observed in our study. However, here we are only interested in sources directly associated with features (i.e., peaks) seen in our MAMBO maps. The discussion of the other sources — which are expected to belong to the YSO classes II and III, since they lack significant millimetric dust emission — is deferred to a later paper. Also note that the emission of some YSOs might be spatially confused with dense core emission. For example, the PSC source 04326+2405 in B18-4 (marked by the only circle) might manifest as an extension in the MAMBO dust emission contours, which however cannot be uniquely separated from the dense core emission.

4.2. YSO Properties

Below we characterise the sources associated with dust emission peaks. All our target cores were covered by the extensive but

⁷ See <http://ssc.spitzer.caltech.edu/legacy/c2dhistory.html> for a detailed documentation.

Table 9. Properties of MAMBO detected c2d Spitzer sources. Like Table 8, but now listing sources from Spitzer point source catalogues and giving the spectral index between 2.2 and 24 μm wavelength. VeLLO candidates are marked in the class designation.

Field	Asso.	c2d Spitzer Source	2MASS Source	$\alpha_{2.2\ \mu\text{m}}^{24\ \mu\text{m}}$	$T_{\text{bol}}^{\text{SST}}$ K	$L_{\text{bol}}^{\text{SST}}$ L_{\odot}	$L_{\text{submm}}^{\text{SST}}/L_{\text{bol}}^{\text{SST}}$	$M_{4200\text{AU}}^{\text{YSO}}$ M_{\odot}	Class
L1521F	C1, P1	SSTc2d J042839.0+265135	none	1.56 ± 0.08	< 30	0.06 to 0.08	0.400 to 0.545	0.729 to 0.749	0, VeLLO
B18-1	[C2], [P5]	SSTc2d J043215.4+242859	04321540+2428597	-0.25 ± 0.06	no IRAC data available				
TMC1-1C	P3	SSTc2d J044138.8+255627	04413882+2556267	-0.04 ± 0.05	681	0.37 ± 0.03	0.008 ± 0.023	0.022 ± 0.005	II
TMC-1	C2, P2	SSTc2d J044112.7+254635	04411267+2546354	0.96 ± 0.06	no IRAC data available				
CB188	C1, P1	SSTc2d J192014.9+113540	19201494+1135400	0.25 ± 0.05	433	1.12 ± 0.09	0.024 ± 0.022	0.322 ± 0.007	I
L673-7	C1, P1	SSTc2d J192134.8+112123	none	0.97 ± 0.08	< 55	0.03 to 0.06	0.284 to 0.573	0.375 to 0.394	0, VeLLO
L1148	C1, P1	SSTc2d J204056.7+672305	20405664+6723047	0.73 ± 0.05	< 140	0.05 to 0.10	0.074 to 0.162	0.139 to 0.148	I, VeLLO
L1228	C1, P1	SSTc2d J205712.9+773544	20571294+7735437	0.14 ± 0.05	388	1.82 ± 0.13	0.042 ± 0.027	0.832 ± 0.007	I
Bern48	C1, P1	SSTc2d J205914.0+782304	20591408+7823040	-0.42 ± 0.10	742	8.35 ± 0.51	0.009 ± 0.013	0.265 ± 0.002	II
L1014	C1, P1	SSTc2d J212407.5+495909	none	0.33 ± 0.07	< 163	0.04 to 0.15	0.118 to 0.411	0.318 to 0.357	I, VeLLO
L1251A	C2, P3	SSTc2d J222959.5+751404	22300004+7513578	0.51 ± 0.05	< 197	0.11 to 0.35	0.060 to 0.187	0.327 to 0.382	I
	C3, P4	SSTc2d J223031.8+751409	none	0.57 ± 0.08	< 44	0.17 to 0.30	0.170 to 0.301	0.831 to 0.900	0
	C4, P5	SSTc2d J223105.6+751337	none	-0.23 ± 0.07	< 63	0.08 to 0.17	0.201 to 0.421	0.630 to 0.683	0

insensitive IRAS and 2MASS surveys. These data thus allows for a homogeneous quantification of all sources in our survey that are brighter than a few times $0.1 L_{\odot}$. Fainter sources could only be detected by Spitzer, from which data exists only for a fraction of our dense cores.

Given the differences in the spectral bands probed by these instruments, it is difficult to compare a source only detected by 2MASS and IRAS to one only detected by 2MASS and Spitzer. In order to explore and suppress related biases in estimates of source properties, we therefore analyse the Spitzer and IRAS data separately. To better distinguish results from the different approaches, in the following properties are labeled by the data source used to derive them (superscripts ‘IRAS’ and ‘SST’, the latter for the Spitzer Space Telescope).

4.2.1. Estimates from IRAS and 2MASS Data

Following Lada (1987), the spectral properties of young stars can be characterised by the spectral index between 12 and $25 \mu\text{m}$ wavelength,

$$\alpha_{12 \mu\text{m}}^{25 \mu\text{m}} = \frac{\log(12 \mu\text{m} \cdot F_{25 \mu\text{m}} / [25 \mu\text{m} \cdot F_{12 \mu\text{m}}])}{\log(25 \mu\text{m} / 12 \mu\text{m})}. \quad (9)$$

Spectral indices are listed in Tables 7 and 8 for all IRAS sources in the MAMBO maps, if detected in these bands. They roughly probe whether the spectral energy distribution (SED) is dominated by photospheric or envelope emission and are sometimes used to classify observed YSO SEDs within evolutionary schemes (Lada 1987).

For the IRAS sources associated with MAMBO peaks for which 2MASS data is available, we calculate the bolometric temperature defined by Myers & Ladd (1993),

$$T_{\text{bol}} = \frac{\zeta(4) h \langle \nu \rangle}{4 \zeta(5) k_{\text{B}}}, \quad (10)$$

where $\langle \nu \rangle = \int_0^{\infty} \nu F_{\nu} d\nu / \int_0^{\infty} F_{\nu} d\nu$ is the flux-weighted mean frequency, ζ is the Riemann zeta function, and h and k_{B} are Planck’s and Boltzmann’s constant. We integrate across the SED by interpolation between observed 2MASS and IRAS bands. For this we use piecewise power laws matching the flux densities, as indicated in Fig. 2. At $500 \mu\text{m}$ wavelength these connect to a power-law representing a modified blackbody of opacity $\propto \lambda^{-2}$ and 15 K temperature that is tuned to fit the MAMBO data; piecewise powerlaws are adopted to hold between $\lambda = 500 \mu\text{m}$ and $1200 \mu\text{m}$ (which is MAMBO’s central wavelength), and $\lambda = 1200 \mu\text{m}$ and ∞ (adopting a flux density distribution $\propto \lambda^{-4}$). For opacity-modified blackbodies of 10 to 20 K temperature this approximates the actual flux density at $\lambda = 500 \mu\text{m}$ within a factor of 1.5. The related uncertainty on integrated properties is much lower though, since the submillimetre part of the SED usually only contributes a few percent to the total luminosity (see, e.g., Table 8). The integration extends from the 2MASS bands at $\approx 1 \mu\text{m}$ to infinity. Unlike Myers & Ladd we treat all flux density upper limits like actual detections. Therefore, the derived bolometric temperatures must be interpreted with some caution, if a source is not detected in some of the bands. In these cases lower and upper limits are assigned to the bolometric temperature, depending on whether adopting flux densities below the upper limits would increase or decrease the calculated mean frequency, respectively.

Based on the derived bolometric temperature the YSOs are separated into four infrared classes. Following Chen et al. (1997,

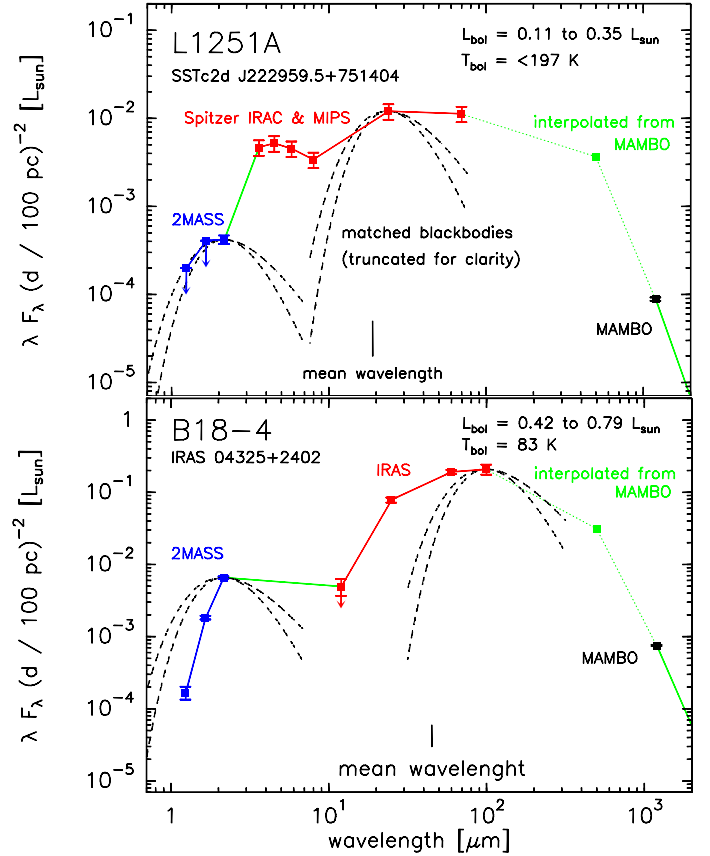


Fig. 2. Example SEDs for YSOs in the c2d MAMBO sample. The *top panel* shows the infrared star SSTc2d J222959.5+751404 associated with the P3 peak in the C2 subcore of L1251A, while the *bottom panel* shows the data for IRAS 04325+2402 associated with the P1 peak in B18-4. The SEDs are composed from 2MASS, Spitzer or IRAS, and MAMBO data, as indicated by *labels*. Also indicated are the interpolated datapoints at $500 \mu\text{m}$ that is calculated from the MAMBO flux density assuming a dust opacity $\propto \lambda^{-2}$ and a dust temperature of 15 K. *Straight lines* indicate the flux density interpolation used to calculate the bolometric luminosity and temperature indicated in the *upper right corners* (as well as the *mean wavelengths* calculated as $c/\langle \nu \rangle$ from Eq. [10] and indicated at the frame bottom). Only *limits* can be derived on T_{bol} and L_{bol} because of some upper limits in the 2MASS data; a conservative lower limit to the luminosity is set by the sum of opacity-modified blackbodies matched to the SED at short and long wavelength (*dashed lines*, drawn for opacities scaling $\propto \nu^{0 \text{ to } 2}$; see text for details). The “sign” of the bolometric temperature limits is set by the mean wavelength lying at longer wavelength than all photometric bands with upper limits.

1995) all stars with $T_{\text{bol}} < 70 \text{ K}$ are considered to be class 0 sources. Those with $70 \leq T_{\text{bol}}/\text{K} < 650$ belong to class I, for $650 \leq T_{\text{bol}}/\text{K} < 2880$ they belong to class II, and class III sources have $T_{\text{bol}} \geq 2880 \text{ K}$. In case of upper or lower limits to the bolometric temperature, the class corresponding to the derived limit is given. This treatment of uncertainties in class assignments is somewhat unsatisfying, however it does not influence our later analysis that is based on the numerical value of T_{bol} .

Sources in a given class (i.e., with similar bolometric temperature) are believed to be in a similar evolutionary stage (Chen et al. 1995 and Chen et al. 1997; see Young & Evans 2005 for illustrative examples). In their evolution from a deeply embedded object to a star surrounded by a remnant dust disk, YSOs are thought to pass through phases 0 to III in increasing order. Thus

class 0 objects would represent the youngest YSOs and class III objects would be in a stage just prior to the main sequence. Almost all of the MAMBO-detected stars covered by the present survey are in classes 0 and I; only one class II and no class III object are among them.

From the interpolated SED we derive an estimate for the bolometric luminosity,

$$L_{\text{bol}} = 4\pi d^2 \int_0^{\infty} F_{\nu} d\nu, \quad (11)$$

for IRAS sources associated with MAMBO dust emission peaks. If the source is detected in a few bands only, an upper limit to the bolometric luminosity is calculated by integrating across the flux density upper limits, while a lower limit is given by the sum of the maximum 2MASS “monochromatic luminosity”, νF_{ν} , plus the maximum detected νF_{ν} in the bands of longer wavelength (see Fig. 2 for an illustration). The latter builds on the fact that for blackbodies modified by an opacity scaling with frequency as ν^0 to ν^2 , the bolometric luminosity is the peak value of νF_{ν} times a factor 1.05 to 1.36. In a similar fashion we derive the luminosity in the submillimetre wavelength range,

$$L_{\text{submm}} = 4\pi d^2 \int_0^{c/350 \mu\text{m}} F_{\nu} d\nu, \quad (12)$$

where c is the speed of light. For both luminosities we also quote uncertainties due to statistical noise, while we do not consider systematic contributions. The aforementioned uncertainties in the submillimetre SED near $500 \mu\text{m}$ wavelength do, however, render the submillimetre luminosity uncertain by a factor of order 2; no precision measurements of it from our data is possible.

4.2.2. Estimates from Spitzer and 2MASS Data

The YSO properties derived from Spitzer and 2MASS data (Table 9) are calculated using methods similar to those adopted for the combined IRAS and 2MASS data. The spectral sampling at wavelengths $\geq 25 \mu\text{m}$ is, however, much worse than for the combined 2MASS and IRAS dataset, resulting in more uncertain estimates for cold sources (with SED peaks at wavelengths $\geq 25 \mu\text{m}$, i.e. with $T_{\text{bol}} \lesssim 160 \text{ K}$). The spectral index for the 2MASS and Spitzer bands, $\alpha_{2.2 \mu\text{m}}^{24 \mu\text{m}}$, is derived by fitting the monochromatic luminosities in the 2.2 to $24 \mu\text{m}$ wavelength range by a power law. It is, thus, not directly comparable to the spectral index derived from IRAS data.

Four stars in our sample might qualify as VeLLOs, given that they appear to be embedded in dense cores and have internal luminosities likely below $0.1 L_{\odot}$. This group includes the sources associated with L1521F P1, L1148 P1, and L1014 P1, which have been subject to detailed studies (Bourke et al. 2006; Kauffmann et al. 2005, and in prep.; Young et al. 2004a). These studies confirm the spectral properties found here. In particular, based on detailed radiative transfer SED modeling, they support the prevalence of internal luminosities $< 0.1 L_{\odot}$. This is an important factor, since the SED analysis presented here has bad spectral sampling at long wavelength, leading to uncertain properties for cool sources. It is also not suited to single out the internal luminosity due to an embedded VeLLO. Note that SED modeling of the source in L673-7 has not been presented so far, leading to a more uncertain status of this source.

Given the evidence for YSO outflows from scattered light nebulosity and outflows seen in CO, the stars in L1521F P1,

L1014 P1, L1148 P1, and L673-7 P1 are proven to be associated with the respective cores and are not unrelated background objects (see the above references and additionally Dunham et al., in prep., for L673-7, and Bourke et al. 2005 for L1014). A recent search for YSOs with internal luminosities $< 0.1 L_{\odot}$ by Dunham et al. (in prep.) lists three of these sources in their “group 1” of confirmed low-luminosity YSOs; L1448-IRS is listed in their “group 3” of good, but unconfirmed, candidates for low-luminosity YSOs. The star in L1251A P5 however, for which our above analysis suggests a low luminosity, is not likely to be a VeLLO since its luminosity limits appear to be too high.

4.2.3. Properties chosen for the Analysis

The above analysis yields two different sets of properties, one based on Spitzer data, one based on IRAS. For the bright sources of a few $0.1 L_{\odot}$, the bolometric temperatures and luminosities estimated from IRAS data are used for the further YSO analysis. This is the preferred option because IRAS data is available for all our cores, and because Spitzer fails to detect a significant fraction of the YSO emission at long wavelengths (see Sec. 5.4.3, leading to biased estimates. We abstain from constructing SEDs combining flux densities from IRAS and Spitzer in order to better control mission-related systematic trends in the data. The IRAS data might, on the other hand, suffer from contamination of unresolved nearby sources. Such contamination is not apparent at a significant level in any of the cases where we have data from both IRAS and Spitzer though.

Fainter sources are usually only detected by Spitzer. Thus, Spitzer data is used for the study of the sources in L673-7 P1, and L1251A P4 and P5. For L1521F P1, L1148 P1, and L1014 P1 results from the more involved Spitzer data analysis by Bourke et al. (2006), Kauffmann et al. (in prep.), and Young et al. (2004a) are used.

5. Analysis

In this section we exploit the survey data in order to better understand the state and evolution of starless and YSO dense cores. We discuss the general core properties before we turn to the discussion of specific issues. Throughout the following discussion we exclude starless peaks and subcores with uncertain properties, unless noted otherwise.

5.1. General Core Properties

Figure 3 shows the frequency distributions of some properties of well reconstructed dense cores. Some conclusions about the physical state of individual cores, and of dense cores in general, can be derived from these distributions.

5.1.1. Radius

The sizes of YSO cores are on average larger than those of starless and candidate VeLLO cores. This could to some extent be an observational bias. Only one YSO subcore in our sample is at a distance below 200 pc , while two dozen starless subcores are within this distance. Because confusion increases with distance, the subcores identified in the more distant YSO cores are thus likely biased towards larger sizes. Large cores might, however, indeed have better chance to form stars.

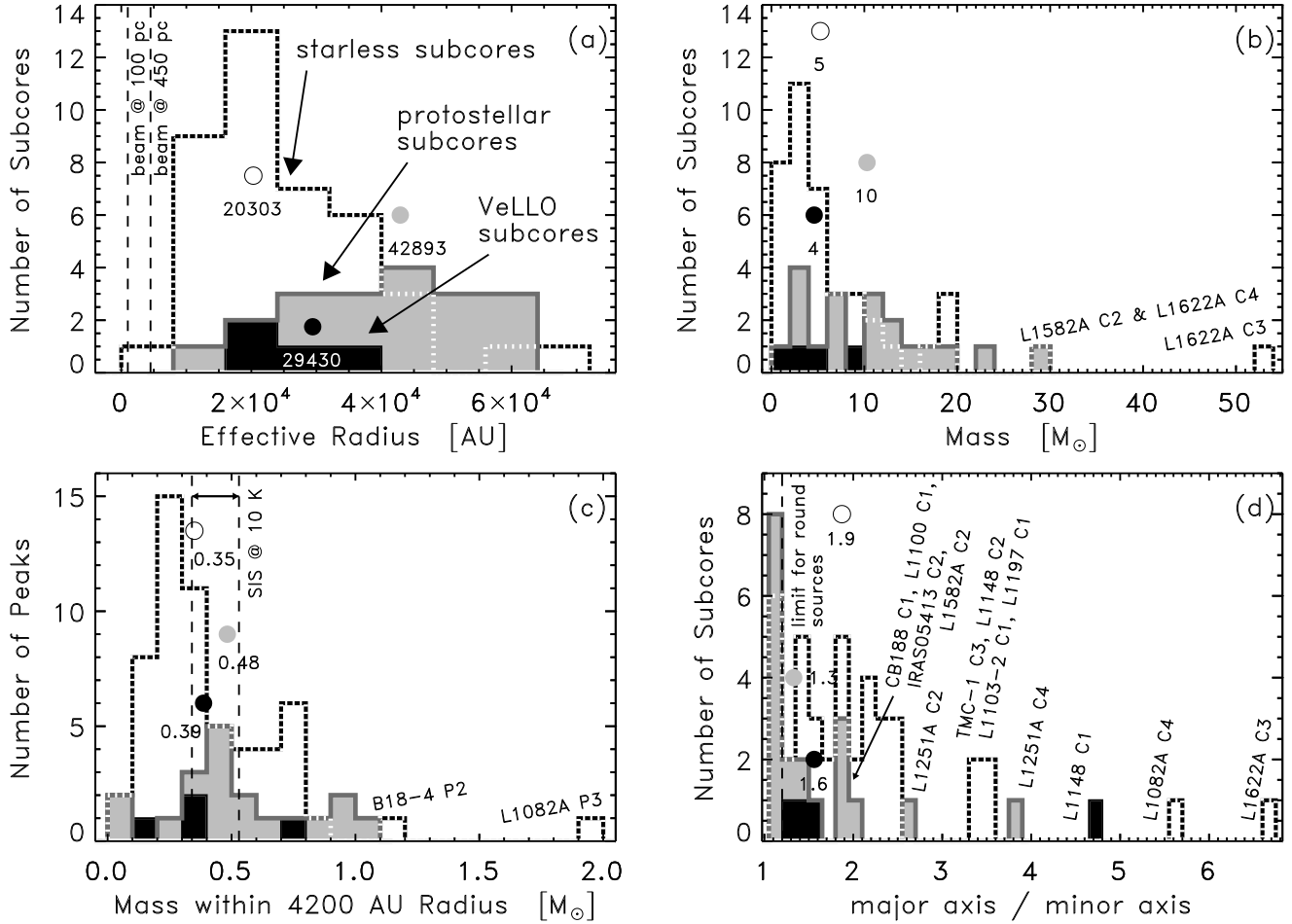


Fig. 3. Overview of the dense core properties, excluding subcores and peaks with uncertain properties due to artifacts. The *dashed line* represents the properties of starless peaks and subcores, while the *grey and black areas* hold for YSO and candidate VeLLO cores, respectively. *Bullets* of the same colours, and the related numbers, give the respective median values of the distributions. *Vertical lines in panel a)* give the beam radius at distances of 100 pc and 450 pc, respectively. The *vertical lines in panel c)* show the range of masses within a 4200 AU aperture for singular isothermal spheres of 10 K temperature and truncation radii of 4200 AU $\rightarrow \infty$. The *vertical line in panel d)* marks the boundary between round and elongated sources. Typical uncertainties of the shown properties are $\geq 10\%$ for M_{tot} , a few $0.01 M_{\odot}$ for $M_{4200\text{AU}}$, and 10% to 20% for the axis ratio.

At small radii the size distribution of starless cores is limited by the beam size; their number steeply drops to zero at the resolution limit. We might miss a population of small subcores.

5.1.2. Total Mass

The mass of the subcore L1622A C3 exceeds the mass of all other subcores by a factor 1.8 and more. Given that L1622A is one out of only 3 dense cores located in the Orion star forming complex, in which special environmental conditions prevail, it might be that L1622A C3 has, e.g., a mass much larger than the other cores in our sample. However, the extreme mass contrast to all other cores does cast some doubt on this.

It might be that L1622A is warmer than most other cores. By adopting a dust temperature of 10 K one would then overestimate the true mass. Furthermore, substructure easily disentangled in more nearby cores may be confused in L1622A, the core with the largest distance in our sample (450 pc). Then the subcore area, and therefore the mass, would be biased towards higher values. This is supported by the fact that L1622A C3 has the largest effective radius of all subcores. Also, L1582A C2 and L1622A C4, which are second to L1622A C3 in mass and are

also located in Orion, are second to L1622A C3 in the effective radius. This may hint that mass and size estimates of cores are indeed biased for larger distances.

Thus, data on distant cores must be interpreted with some caution. They might well have extreme properties, but given the lack of sufficient spatial resolution, we cannot be sure about this. Properties of nearby and distant cores are not necessarily directly comparable.

5.1.3. Mass within 4200 AU

For L1082A P3 the mass $M_{4200\text{AU}}$ exceeds those of all other peaks by a factor 1.7 and more. This large aperture mass contrast may hint on a biased mass estimate. The dust in L1082A P3 might be significantly warmer than 10 K, if this core is heated by an undetected embedded star. Following Myers et al. (1987), the failure of IRAS to detect a point source in this peak implies (for a distance of 400 pc) an upper limit to the bolometric luminosity of $\approx 0.8 L_{\odot}$ to any embedded source. In this case the average dust temperature could be 15 K instead of the assumed 10 K, and the mass could be overestimated by us by up to a factor of 2. Then $M_{4200\text{AU}}$ would not be unusual for a YSO core. Though

this evidence is not conclusive, we, thus, suspect the presence of a heating YSO source in L1082A P3 that is too faint to be detected by IRAS. Unfortunately, no Spitzer data is available for this region to confirm this.

The peak B18-4 P2 is separated from the other starless subcores. As Spitzer images show, no point sources are associated with this peak, and so internal heating cannot explain the unusual value of $M_{4200\text{AU}}$. A YSO of $\approx 0.5 L_{\odot}$ resides in B18-4 P1, which is separated from B18-4 P2 by 10 000 AU = 0.05 pc. At this distance a YSO of this low luminosity is unlikely to provide significant external heating to the peak P2. Thus the high value of $M_{4200\text{AU}}$ in B18-4 P2 is likely to be real.

The $M_{4200\text{AU}}$ distributions for all types of subcores peak at a mass of $\approx 0.35 M_{\odot}$. The mean ($0.42 M_{\odot}$, $0.54 M_{\odot}$, and $0.41 M_{\odot}$ for starless, YSO, and VeLLO cores, respectively) and median ($0.35 M_{\odot}$, $0.48 M_{\odot}$, and $0.39 M_{\odot}$, respectively) aperture mass is of the same order. Since this is a typical value for all kinds of subcores, the underlying physical process shaping the distributions must be fundamental. Interestingly, this mass is similar to the mass within 4 200 AU for a (truncated) singular hydrostatic equilibrium isothermal sphere (SIS) of 10 K gas temperature,

$$M_{4200\text{AU}} = 0.34 M_{\odot} \varepsilon (T_{\text{g}}/10 \text{ K}). \quad (13)$$

Here T_{g} is the gas temperature and the factor ε depends on the density distribution outside a radius of 4 200 AU; it is 1 if the density drops to zero outside 4 200 AU and becomes $\pi/2 \approx 1.57$ if it continues out to infinity. This mass constitutes a critical value for an SIS: no hydrostatic equilibrium solutions exist for higher values of $M_{4200\text{AU}}$. It thus might be that this critical condition manifests in characteristic values of dense core properties.

If this is true it has two interesting implications. First, dense cores would preferentially exist in a close-to-critical physical state. We note that interestingly such near-critical core states have previously been inferred by Alves et al. (2001) and particularly by Kandori et al. (2005). Second, the total pressure in the core, P , appears to be comparable to the thermal pressure. Contributions to the total pressure from the effect of turbulent gas motions or magnetic fields can not much exceed the thermal pressure. Otherwise the critical mass in the 4 200 AU aperture would be much larger since one would need to replace the gas temperature with some higher effective one, $T_{\text{g}} \rightarrow T_{\text{eff}} = 2.33 P m_{\text{H}} / (\rho k_{\text{B}}) > T_{\text{g}}$, where m_{H} is the hydrogen mass and the factor 2.33 holds for a gas mixture at cosmic abundance with most hydrogen in molecular form.

5.1.4. Elongation

Only 14% and 44% out of all starless and YSO subcores, respectively, have major-to-minor axis ratios ≤ 1.2 (where the uncertainty is 10% to 20%) and can be considered round; most subcores are not round. Unless these subcores are shaped by magnetic fields, which provide a non-isotropic supporting pressure, they can hardly on the whole be in a state of hydrostatic equilibrium.

The axis ratio distribution is continuous up to ratios of 2.0 and 2.5 for YSO and starless subcores, respectively. Several subcores have much larger axis ratios. Interestingly, two of the most distant subcores have the largest elongations (L1082A C4 and L1622A C3 at distances ≥ 400 pc). This suggests that some cores appear elongated due to unresolved cores within the beam, an effect that on average increases with distance (also see Young et al. (2006b) for this effect in Bolocam maps).

For starless cores, the median axis ratio that we derive, i.e. 1.9, is very similar to those derived from NH_3 (Jijina et al. 1999,

median of 1.5 to 2.2) and extinction maps (Lee & Myers 1999, mean of 2.4 ± 0.1) of larger core samples. For YSO cores, however, the median aspect ratio of 1.3 for our sample is at the low end of the aspect ratios derived by the above studies (medians of 1.4 to 2.0, respectively a mean of 2.2 ± 0.2 , for their YSO cores). This difference is probably an effect of the internal heating on the dust emission intensity distribution (see below).

The axis-ratio distribution has in the past been used to study the intrinsic three-dimensional geometry of dense core shapes. Following Myers et al. (1991), the median axis ratio of 1.9 for starless subcores (we exclude YSO cores, since internal heating influences the observed shapes; see next paragraph) is the expected projected axis ratio of prolate (“cigar-like”) spheroids with an intrinsic major-to-minor axis ratio of ≈ 2.5 , and of oblate (“disk-like”) ones with an axis ratio of ≥ 4 (for an observed ratio > 1.7), respectively⁸ We cannot resolve this ambiguity. Some existing theoretical analysis favors prolate cores (Myers et al. 1991; Ryden 1996), while other work prefers oblate ones (Jones et al. 2001; Jones & Basu 2002; Goodwin et al. 2002; Tassis 2007).

The median axis ratio of YSO subcores is smaller than that of starless and VeLLO cores. This could be because the YSO heating leads to an intensity peak of small physical size and low aspect ratio (since the heating, to first order, decreases radially away from the star; Eq. 5), which is blurred into a structure of even lower aspect ratio because of beam smearing. On the other hand stars are expected to form in close-to-spherical density enhancements, which in projection show a low elongation (Shu 1977). Then, YSO cores would be less elongated than the starless cores with their complex shapes at lower intensity contours. Both effects would also explain the aforementioned decrease of the aspect ratio from the large-scale core structure probed by, e.g., NH_3 and extinction maps to the core centers probed by dust emission. A more detailed analysis is needed to separate these effects.

The YSO subcores CB188 C1, IRAS05413 C2, L1100 C1, L1251A C2, and L1251A C4 are well separated from the other YSO cores in the elongation distribution. For IRAS05413 C2, however, the axis ratio is very uncertain (1.9 ± 0.5). The observed elongation is likely to be an observational artifact. In L1251A, where the major axis exceeds the beam size by a factor of several, this elongation likely reflects the morphology of the dense core from which the embedded star formed. For CB188 and L1100, however, where the major axis exceeds the beam size by a factor 3.2 and less, this elongation should reflect the morphology of the immediate density peak from which the young star accretes. This region could be shaped by the interaction with outflows from the central star. An outflow has indeed been detected toward CB188 (Yun & Clemens 1994) and for L1100 there is some evidence for an outflow from broad line wings (De Vries et al. 2002). For CB188 the position of the outflow axis derived by Yun & Clemens (1994) and the major axis of the dust emission intensity distribution are neither aligned nor perpendicular (position angles of $\approx 75^\circ$ and $16^\circ \pm 5^\circ$, respectively). If the elongated structure towards CB188 seen in the MAMBO maps is indeed related to the outflows, then the dust emission feature is likely to trace the wall of an outflow cavity. If it would trace the jet or a YSO disk, the axes are expected to be parallel or perpendicular. While these observations do not prove the interaction

⁸ This analysis assumes a random distribution of the core axes in space. This might not be justified for our sample, since most of our cores are situated in a small number of star-forming regions, in which preferred orientations might prevail.

between jets and the dense core, they motivate dedicated studies on this issue. A more detailed analysis of the dust emission maps might yield more candidates for jet-core interactions.

5.2. Correlations between Core Properties

Correlations between core parameters, like e.g. the famous size-linewidth relation (Larson 1981), can provide important hints on the nature of dense cores. Such correlations are indeed seen in our data (Fig. 4). Unfortunately, many of these cannot be cleanly separated from observational biases, and great care is needed if one wishes to exploit our data in this fashion.

To give examples, our source identification scheme directly leads to a radius-dependent lower limit to the mass, since the intensity will be at least twice the noise level within any sub-core, and thus $M \geq 2\mu_{\text{H}_2} m_{\text{H}} \pi N_{\text{RMS}}(\text{H}_2) r_{\text{eff}}^2$ (where μ_{H_2} and m_{H} are the mean molecular weight per hydrogen molecule and the mass of the hydrogen atom, respectively, and $N_{\text{RMS}}(\text{H}_2)$ is the column density corresponding to the intensity RMS; also see Appendix A). Similarly, we cannot detect massive cores of low peak column density, $N_{\text{max}}(\text{H}_2)$, in maps of limited radius, r_{map} , since $M \leq \mu_{\text{H}_2} m_{\text{H}} \pi N_{\text{max}}(\text{H}_2) r_{\text{map}}^2$. Also, we might miss low-mass (and therefore small) cores of high column density because of beam smearing. Similar considerations apply regarding $M_{4200\text{AU}}$, which can be interpreted as an aperture-averaged column density (that, however, does not suffer from beam smearing).

Given the above uncertainties, we are careful in drawing conclusions from apparent correlations. In other words, parts of the parameter space e.g. explored in Fig. 4 might not be populated because cores in these regions would not be detected given our sensitivities.

5.3. Dense Cores and their Evolution

Our data not only reveals cores in various states of evolution but in combination with the complementary YSO data we can also make statements on the progress of dense cores through evolutionary stages. The latter suggests some necessary conditions for active star formation to be possible, while it also indicates diverse evolutionary tracks for individual cores.

5.3.1. Densities from Masses and Radii

A rough estimate of the core densities can be derived from the peak aperture masses when assuming specific density profiles. The estimates will certainly often be off from the actual value by a large factor, but this analysis is still illustrative to understand trends in the data.

We here compare the observed aperture masses and radii at 70% peak intensity to those expected for dense cores with density profiles $n(\text{H}_2) = n_c(\text{H}_2)/(1 + [r/r_{1/2}]^2)$, which provides a good approximation to the density structure of starless cores (Tafalla et al. 2002). In this $n_c(\text{H}_2)$ is the central particle density, while r is the radius from the center, and $r_{1/2}$ is the radius at which $n(\text{H}_2) = n_c(\text{H}_2)/2$. Particle densities can be related to mass densities using the c2d standard H_2 -to-gas mass conversion factors documented in Appendix A. Figure 5 illustrates this analysis.

This analysis indicates typical central densities of order $3 \cdot 10^4 \text{ cm}^{-3}$, while for some extreme cores we derive densities of up to 10^6 cm^{-3} . Similar figures were derived by Tafalla et al. (2002), Crapsi et al. (2004), and Kirk et al. (2005). Note, however, that the obtained densities are crude estimates that suffer

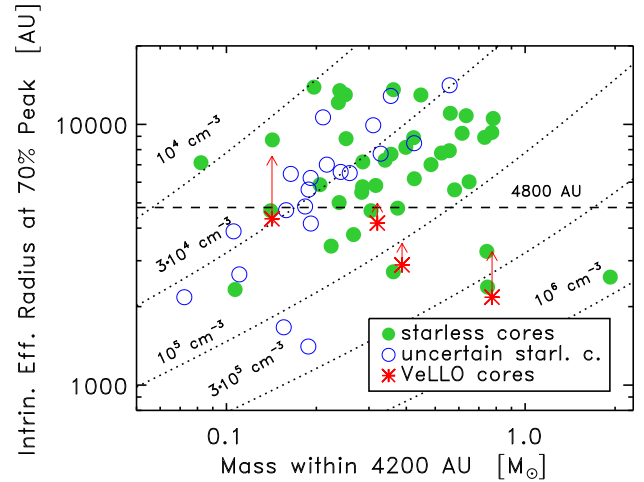


Fig. 5. Relation between the intrinsic radius at 70% peak intensity and the mass within 4200 AU radius from the peak for VeLLO candidate and starless cores. The plotted effective radii deviate from the ones listed in Table 4 in that the beam smearing is removed ($7/2$ at 70% peak). See Fig. 4 for an explanation of the symbols. The radius bias due to central heating of VeLLO cores (Sec. 5.5.2) is indicated by arrows. The dotted lines indicate curves of constant central density for some simple density profile of varying radius (see the text for details). The labels give the related central H_2 column density. The dashed line indicates the upper radius limit for evolved dense cores, ≤ 4800 AU, suggested by Crapsi et al. (2005). The candidate VeLLOs observed all fall below this limit and are, for given aperture mass, smaller than most starless cores, though this in part might come from internal heating. Also, most VeLLO cores appear to have central densities exceeding those of most starless cores. VeLLO cores are thus possibly physically more evolved than starless cores. This appears to distinguish them from starless cores.

from significant systematic uncertainties. Anyway, to give examples, for L1521F C1 the density of $\approx 4 \cdot 10^5 \text{ cm}^{-3}$ derived from our simplified analysis is in good agreement with the density of $\approx 5 \cdot 10^5 \text{ cm}^{-3}$ (for our choice of dust properties) derived by Crapsi et al. (2004).

Note that VeLLO candidate cores appear to have unusually large densities, when compared to starless cores. Section 5.5.2 discusses this in detail.

Our sample is highly biased and inhomogeneous, but it is still illustrative to derive relative dense core lifetimes from the relative numbers of dense cores of different physical state. Such estimates assume a constant core formation rate across the sample and common evolutionary paths for all cores, neither of which are likely correct for our cores. Anyway, we find about 35 starless subcores in the $10^4 < n_c(\text{H}_2)/\text{cm}^{-3} < 10^5$ density range, and 4 subcores in the $10^5 < n_c(\text{H}_2)/\text{cm}^{-3} < 10^6$ range. Under the above assumptions this implies that dense cores reside at densities of 10^4 to 10^5 cm^{-3} for a time exceeding the one for densities of 10^5 to 10^6 cm^{-3} by a factor ≈ 9 . For reference, the free fall timescale⁹,

$$\tau_{\text{ff}} = 9.8 \cdot 10^4 \text{ yr} [n(\text{H}_2)/(10^5 \text{ cm}^{-3})]^{-1/2}, \quad (14)$$

only varies by a factor $10^{1/2} \approx 3$ between the density bins. Dense core evolution in free fall would thus not explain the relative number of cores in different density bins.

⁹ We give the collapse time for a homogeneous sphere of density $n(\text{H}_2)$, i.e. $\tau_{\text{ff}} = (3\pi/[32G\rho])^{1/2}$, where G is the constant of gravity and ρ is the volume-averaged density. Our calculation assumes a mean particle weight of 2.8 per hydrogen molecule.

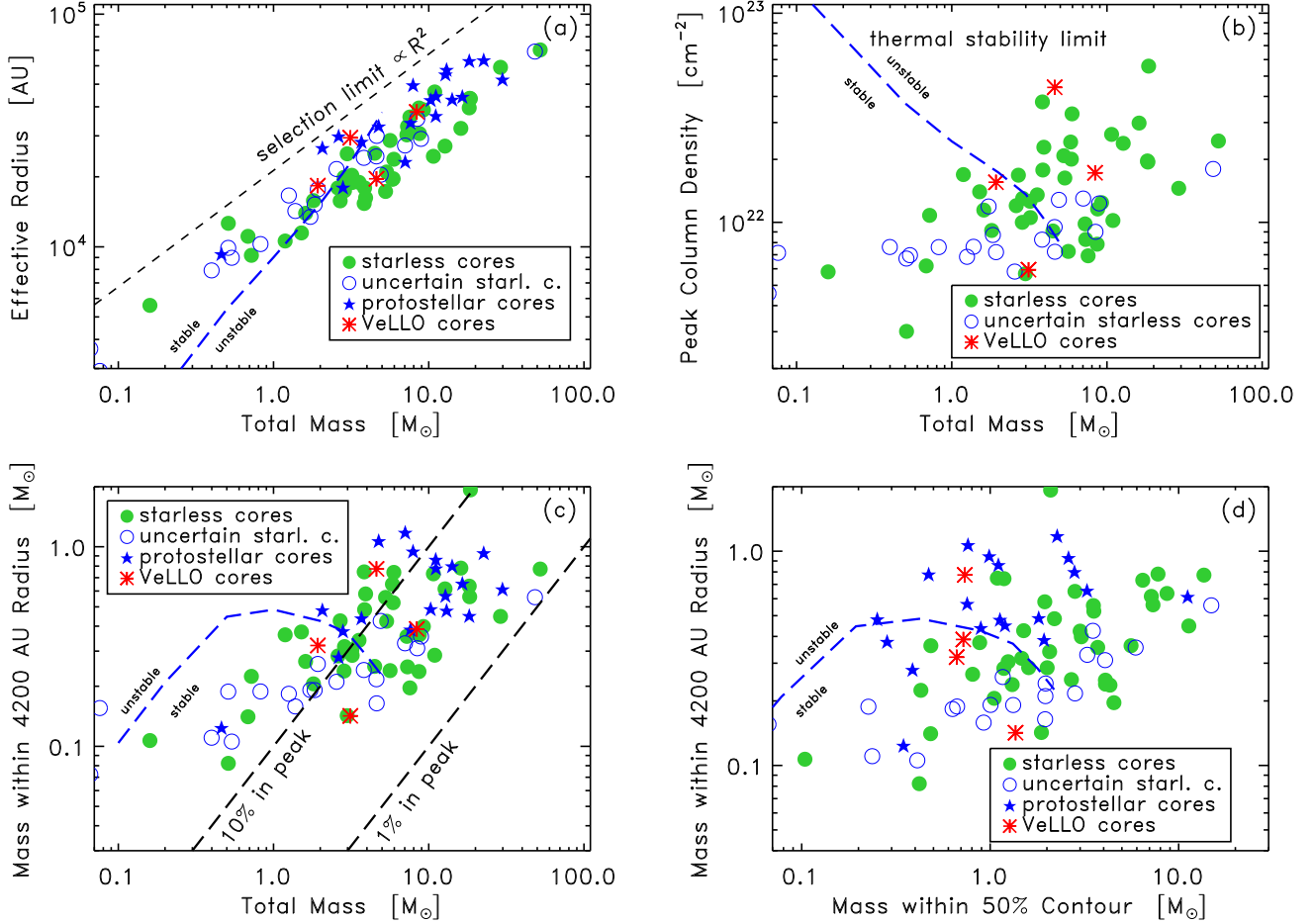


Fig. 4. Necessary conditions for active star formation from relations between dense core properties. *Filled and empty circles* give the properties of subcores with well determined and uncertain properties due to artifacts, respectively. *Stars and asterisks* are used for subcores hosting YSOs and candidate VeLLOs, respectively. The *diagonal dashed line in panel a)* indicates a selection limit; for a given total mass all subcores larger than this limit would be too faint to be identified in our maps. The *diagonal dashed lines in panel c)* mark where $M = 0.1 M_{4200\text{AU}}$ and $M = 0.01 M_{4200\text{AU}}$: only a fraction of the dense core mass is available to form stars from a column density peak. The *curved dashed lines* show the critical stability limits for hydrostatic equilibria with pure thermal pressure. For given total mass, or mass within the half intensity contour, all subcores with pure thermal pressure and with radii smaller than the critical one — respectively column density or aperture mass exceeding the critical one — are unstable. These stability limits might manifest in the data as necessary conditions for active star formation; most dense cores presently forming stars exceed these limits. However, these limits do not give sufficient conditions for ongoing star formation. Many starless cores have properties exceeding the critical values. In the core evolution framework discussed in the text this could be understood if these subcores are in hydrostatic equilibrium but supported by significant non-thermal pressure, or are collapsing.

5.3.2. Evolutionary States

Crapsi et al. (2005) suggested some criteria to assess a starless core’s evolutionary state. These also include criteria based on observations of molecular lines, which we cannot evaluate using our data. Table 12 therefore only evaluates criteria based on the dust emission. Following Crapsi et al., evolved cores must have central densities (Sec. 5.3.1; recall that this analysis only yields rough estimates) exceeding $2.5 \cdot 10^5 \text{ cm}^{-3}$ (when converting their results to our choice of dust properties) and radii at 70% peak intensity $< 4800 \text{ AU}$. Naively, one would also associate high column densities with an advanced evolutionary state. Somewhat arbitrarily we thus choose a limit of $0.7 M_{\odot}$ to highlight those starless cores with unusually high column densities in our sample. Table 12 also includes candidate VeLLO cores which are supposedly young and thus likely to not yet be significantly affected by YSO formation and evolution.

This analysis reveals 5 cores that fulfill both criteria by Crapsi et al. (2005), i.e., they are small in size and have a high central density. For two of these (L1521F C1 and L183 C3) this was already shown by Crapsi et al., while our study gives 3 more candidate evolved cores matching his criteria (B18-1 C1, B18-4 C1, and L1082A C2). Note that these cores are actually the only ones with $n_c(\text{H}_2) > 2.5 \cdot 10^5 \text{ cm}^{-3}$ and that they also have $M_{4200\text{AU}} > 0.7 M_{\odot}$. Three further cores (TMC-2 C1, TMC-1C C3, and L1622A C3) stand out in their aperture masses, thereby suggesting a somewhat evolved state. They do not fulfill the Crapsi et al. criteria, but recent molecular screening of TMC-1C C3 shows that at least one of these cores indeed seems to be close to the onset of star formation (Schnee et al. 2007a).

The c2d MAMBO survey thus reveals 3 previously unknown candidates for evolved starless cores fulfilling the criteria by Crapsi et al. (2005), and 3 further ones likely to be evolved on basis of their aperture masses. Note, however, that — following the above criteria — some of these cores seem to be more ad-

Table 12. Starless cores that fulfill at least one criteria for an advanced evolutionary state, as well as VeLLO candidate cores. Brackets for VeLLOs indicate that $r_{70\%}$ does not fulfill the criterion for evolved cores after correcting for internal luminosity.

Core	$n_c(\text{H}_2)$ > $2.5 \cdot 10^5 \text{ cm}^{-3}$	$r_{70\%}$ < 4 800 AU	$M_{4200\text{AU}}$ > $0.7 M_\odot$
<i>evolved starless cores:</i>			
L1521B-2	C2 -	+	-
L1521-2	C2 -	+	-
B18-1	C1 +	+	+
B18-2	C1 -	+	-
TMC-2	C1 -	-	+
B18-4	C1 ^a +	+	+
TMC-1C	C3 -	-	+
TMC-1	C1 -	+	-
L1507A	C3 -	+	-
L1622A	C3 -	-	+
L183	C1 -	+	-
	C2 +	+	+
	C5 -	+	-
L1082A	C2 +	+	+
<i>VeLLO cores:</i>			
L1521F	C1 +	+	+
L673-7	C1 -	+	-
L1148	C1 -	(+)	-
L1014	C1 -	(+)	-

Notes: a) Numbers hold for the starless P2 peak in B18-4.

vanced in their evolution than some candidate VeLLO cores that actually already do form stars. This suggests that the Crapsi et al. criteria are somewhat biased: they are well suited to select *some* evolved cores, but not all of them. In this respect it is important to keep in mind that their criteria were tuned to select cores like the prototype evolved starless core L1544. The analysis presented here suggests that evolved cores with physical properties different from those derived by Crapsi et al. (2005) do exist. This is not surprising though, e.g. given the observed range in stellar masses. The Crapsi et al. (2005) study might, e.g., preferentially select evolved rather massive cores on the verge to form stars of rather large mass. It would then be plausible to find evolved cores that are on the verge of forming lower mass stars (i.e., a few $0.1 M_\odot$), but have too low mass and column density to be incompatible with the Crapsi et al. criteria. In this light, Sec. 5.3.4 presents some suggestions for further refinements of criteria.

5.3.3. Star Formation Efficiency

Given a typical duration of the main accretion phase of order 10^5 yr (Barsony & Kenyon 1992; Greene et al. 1994; Kenyon & Hartmann 1995), and expected velocities for the growth of the infalling inner part of YSO envelopes of order 0.2 km s^{-1} (e.g., for singular isothermal spheres; Shu 1977), only the mass within a few 10^3 AU from a forming YSO are available for its formation. The few 10^3 AU radius of this volume are much smaller than the subcore sizes of several 10^4 AU observed by us (e.g., Fig. 3 [a]). Thus, only a small fraction of a subcore's mass is available for the formation of a given YSO. This fraction is an estimate of the subcore's efficiency to form a given YSO. The latter is a lower limit to the *total* star formation efficiency, i.e., the mass ratio between the dense cores mass and the *total* mass of all YSOs produced by it.

We use a radius of 4 200 AU for a quantitative evaluation of this efficiency, the maximum infall radius derived for the above considered YSO and envelope properties. Some 2% to 20% of the total mass of a dense core are contained in a 4 200 AU radius aperture centered on its brightest peak (Fig. 4 [c]). For other average velocities at which the infalling region grows, $\langle v_{\text{in}} \rangle$, and accretion times, τ_{accr} , the appropriate aperture radius will be larger by a factor $\approx \langle v_{\text{in}} \rangle / (0.2 \text{ km s}^{-1}) \cdot \tau_{\text{accr}} / (10^5 \text{ yr})$. In case of $n \propto r^{-2}$ density profiles the aperture mass scales linearly with the aperture radius. To give an example, recent c2d determinations indicate a class I lifetime of order $5.3 \cdot 10^5$ yr (Evans et al., in prep). Since YSOs are supposed to accrete during this phase, this would imply (using the above assumptions) that a YSO can accrete a mass $5.3 \cdot M_{4200\text{AU}}$ and that cores have a star-formation efficiency of order of several 10%.

Long accretion timescales might, however, imply low accretion efficiencies on the size scale of the infalling matter, if collapse proceeds in free fall. In this case, YSO accretion timescales of several 10^5 yr, combined with average aperture masses $M_{4200\text{AU}} = 0.4$ to $0.5 M_\odot$ (Sec. 5.1.3), imply that there is enough time to accrete several $0.5 M_\odot$ onto a forming YSO. Since, however, the average stellar mass, $\langle M_\star \rangle$ is of order $0.4 M_\odot$ (e.g., Table 2 in Kroupa 2002), a significant fraction of this aperture mass does not seem to end up in the forming star. This fraction increases with increasing accretion timescale; for the above collapsing singular isothermal sphere it is $(M_{\text{in}} - \langle M_\star \rangle) / M_{\text{in}}$, where the infalling mass $M_{\text{in}} = (\tau_{\text{accr}} / 10^5 \text{ yr}) \cdot M_{4200\text{AU}}$ and thus is of order $3/4$ for $\tau_{\text{accr}} \approx 4 \cdot 10^5$ yr. The efficiency could, however, still be large if collapse does not occur in free fall.

In summary, our data indicates a star formation efficiency of order 10%, with an uncertainty of a factor of several. Such an efficiency is of an order of magnitude exceeding estimates for the star formation efficiency of molecular clouds ($\lesssim 2\%$; e.g., Leisawitz et al. 1989). This might, e.g., indicate that the star formation efficiency is not only controlled by processes operating on the scales of dense cores, but that also by processes of importance on larger scales. Also, the low star formation efficiency on the scales of cores suggests that dense core mass functions do not directly map into stellar initial mass functions: core and YSO masses will differ, and it is not clear that their ratio is constant. In other words, it is not clear which core mass definition is relevant to measure the mass of a core that is available for accretion onto forming stars. To give an example, here we discuss three mass scales (i.e., M_{tot} , $M_{50\%}$, and $M_{4200\text{AU}}$), none of which is proven to measure the accretable mass. This questions basic assumptions made in some studies relating mass functions of stars and cores, in particular since the shape and absolute scale of the mass distribution depends on the adopted core mass definition (e.g., Fig. 3, panels [b] and [c]). There is evidence though that the shapes of some of these distributions might well be coupled to the one of the IMF (Alves et al. 2007). This would then point at a constant efficiency.

5.3.4. Star Formation Ability

Figure 4 (d) indicates that there is a fundamental difference between cores actively forming stars (i.e., they contain a YSO) and those who don't: starless cores in our sample have aperture masses of about 0.1 to $2.0 M_\odot$ (also see 3 [c]), while all young ($T_{\text{bol}} \lesssim 300 \text{ K}$) YSOs have envelope masses $\gtrsim 0.3 M_\odot$ (also see Fig. 8; we exclude the VeLLOs, since their physics may be governed by different processes, and CB188, since outflow-core interaction might have affected the core properties [Sec. 5.1.4]). The naive interpretation of this observation is that dense cores

must have $M_{4200\text{AU}} \geq 0.3 M_{\odot}$ in order to be able to actively form stars. The full story might be a bit more complex, since the present YSO aperture masses will deviate from the ones of their natal cores at the onset of star-formation. For example, a collapsing SIS (Shu 1977) has an aperture mass decreasing with time, suggesting that the observed YSO aperture masses are lower than the initial ones.

Thus $M_{4200\text{AU}} \geq 0.3 M_{\odot}$ appears to be a *necessary* condition for active star formation to occur (defined as embedded YSOs being present), but it is not a *sufficient* one, since there are many starless cores above the limiting aperture mass (with B18-1 P3, B18-4 P2, and L183 P3, all with $M_{4200\text{AU}} > 0.7 M_{\odot}$, as extreme examples; also see the discussion in Sec. 5.3.2). Thus, cores with $M_{4200\text{AU}} \geq 0.3 M_{\odot}$ *can* actively form stars, but they do not need to do so. Note, however, that starless cores with $M_{4200\text{AU}} \gg 0.3 M_{\odot}$ might well already be in a state of collapse and be destined to form a star, even when no embedded YSO has formed yet.

In a similar way, a total mass $\geq 2 M_{\odot}$ appears to be a necessary condition for active star formation to be possible. Again, there are some starless subcores with total masses much higher than those for some star-forming ones.

It is interesting to test this observation against simple models of dense core structure. For this we use models of near-isothermal pressure-supported spheres. Using boundary conditions appropriate for typical dense cores in the solar neighborhood (a visual shielding extinction of 5 mag from a dense core envelope, a cosmic ray flux of $3 \cdot 10^{-17} \text{ s}^{-1}$, and the solar neighborhood interstellar radiation field), we evaluate the stability of these spheres in case of no support from turbulence or magnetic fields (i.e., non-isothermal Bonnor-Ebert spheres; Kauffmann & Bertoldi, in prep., and Galli et al. 2002).

For fixed total mass, respectively mass at half intensity ($M_{50\%}$), these models predict critical values for parameters like the peak column density, so that all objects exceeding these cannot be stable against collapse unless supported by additional non-thermal pressure. These critical limits (or calculations are limited to total masses $\leq 5 M_{\odot}$ given a lack of molecular cooling rates for low densities, leading to a break in the boundaries drawn) are indicated in Fig. 4. Within the model, they give the limiting properties beyond which a dense core can become unstable and collapse to form a star. If these models have any relevance, the critical limits should therefore manifest in the distribution of observed actual dense core properties.

Notably, as shown in Fig. 4 (c) and (d), all young YSOs (excluding CB188 C1 and VeLLO candidates, as discussed above) are indeed consistent with having masses in excess of the mass-dependent critical aperture mass for pure thermal pressure, and the theoretically derived critical masses seem to describe the observed necessary condition for active star formation. The models also describe the necessary condition on the total mass (Fig. 4 [a] and [c]).

If dense cores can be described by the above models, a starless dense core of fixed total mass could evolve towards collapse by approaching the critical aperture mass (starting with sub-critical value) as a quasi-hydrostatic sphere, turn into a collapsing core once exceeding the critical value, and finally become a core with active star formation. In this picture starless cores with properties exceeding the critical ones for pure thermal pressure could then be collapsing cores. They could also be quasi-hydrostatic equilibria with additional non-thermal pressure, for which the critical values are beyond those for pure thermal pressure. If the latter was true, the co-existence of starless

as well as star-forming cores in the same parameter range suggests that different cores are supported by different levels of non-thermal pressure.

Note that shifts of the masses by a factor 2, either globally for all sources, or for starless cores relative to those with YSOs, only marginally influence the above discussion. (Such shifts are possible because of the uncertainties in opacities and temperatures, as discussed in Appendix A.) Still, our data would hint at the existence for necessary conditions for star formation. Strong YSO-to-starless core relative shifts of a factor 2 could, however, lead to a clear separation of starless and YSO cores in some diagnostic diagrams. Then, it might turn out that, e.g., *all* cores above some limiting aperture mass do form stars. This would turn the aforementioned *necessary* condition for star formation into a *sufficient* one. Strong global and relative mass shifts by a factor 2 might also make the applicability of the theoretical justification for the limiting curve questionable.

5.4. YSOs and their Evolution

Given the number of YSO cores, the c2d MAMBO survey is well suited to study evolutionary effects in YSO cores. Our analysis also includes the properties of some recently discovered VeLLO candidates.

The c2d MAMBO sample contains 5, 14, and 1 YSOs of the classes 0, I, and II, respectively. This is, e.g., in between the 0-to-I class ratio of 1:10 for Taurus and the Ophiuchus cloud (Andre & Montmerle 1994; Motte et al. 1998) and ratios of order 1:1 for Perseus (Hatchell et al. 2007) and some isolated cores (Visser et al. 2002). Note, however, that our sample is anything but unbiased, and thus not ideal to constrain class lifetimes from their relative number.

5.4.1. YSO Luminosities

To better characterise the central star we use the internal luminosity, L_{int} , that is due to the YSO instead of the bolometric luminosity, i.e., the total radiative power minus that due to interstellar heating. This luminosity is, however, taken to be identical to the bolometric one, except for some candidate VeLLOs for which detailed estimates exist from other studies (Bourke et al. 2006; Kauffmann et al., in prep.; Young et al. 2004a).

The approximation of the internal luminosity by the bolometric one is justified since the derived bolometric luminosities are usually dominated by the power of the embedded source, and not by the heating processes in the interstellar medium (like interaction with cosmic rays or absorption of the interstellar radiation field). The latter contribution can be estimated for the material within 4 200 AU from the density peak. A heating power $0.16 L_{\odot} \cdot (M_{4200\text{AU}}/M_{\odot})$ is required to heat the matter to a typical interstellar temperature of 10 K. For $M_{4200\text{AU}} = 0.4 M_{\odot}$, which is typical for the YSO cores in our sample (Sec. 5.1.3), this power is $0.06 L_{\odot}$.

In some sources, however, the bolometric luminosity derived by us is dominated by the power due to interstellar heating processes. For dust temperatures of at least 10 K this power exceeds the inferred bolometric luminosities of the YSOs in L1521F P1, L673-7 P1, and L1251A P3 and P5 (also depending on whether relying on IRAS or Spitzer data), also demonstrating that our method to derive L_{bol} can miss part of the actual radiative power. This is also reflected in these sources' unusually large submillimetre-to-bolometric luminosity ratios. In such cases the bolometric luminosity is not a good measure of the power input

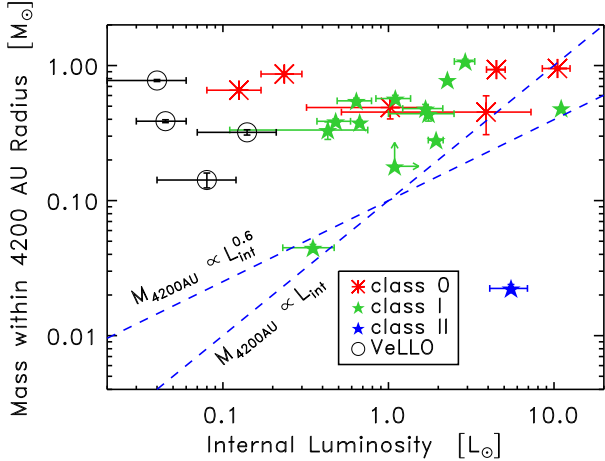


Fig. 6. The relation between the internal luminosity and the mass within a peak-centered 4 200 AU radius aperture for YSO cores. The internal luminosity is the radiation due to the embedded star, i.e., the bolometric luminosity minus the power from interstellar heating. *Markers of different shade and shape* refer to YSOs belonging to different infrared SED classes assigned on basis of their bolometric temperature (see legend). The *dashed lines* indicate the conceptual boundary for a spectrum of class 0 sources and objects in later evolutionary stages for a spectrum of stellar mass-luminosity relations, $M_{4200\text{AU}} \approx 0.1 M_{\odot} (L/L_{\odot})^{0.6 \text{ to } 1.0}$. Interestingly, class 0 and class I sources covered by the c2d MAMBO survey are not separated by the conceptual class boundaries.

by the young star. This leads to uncertain heating corrections in mass estimates of YSO envelopes (Sec. 3.2.3). The related uncertainties in the mass estimates are, however, not significant, given that the low derived luminosities imply small corrections.

5.4.2. Envelope Masses and Luminosities

YSOs are expected to evolve in luminosity and envelope properties during the star formation process. Three basic properties to characterise a YSO are its age, as believed to be roughly measured by the bolometric temperature or the infrared class, the luminosity, and the amount of matter surrounding the star. The latter two should depend on the age since they, e.g., depend on the accretion rate and the stellar mass and radius, which all evolve with time. Figure 6 shows the relation between luminosities and envelope masses. The latter are approximated by the mass within 4 200 AU radius from the star since this property has been studied in the past (Motte & André 2001).

Surprisingly, no clear evolutionary trend is obvious in this diagram, except for the significant decrease in $M_{4200\text{AU}}$ towards the class II phase; the crowding of VeLLO candidates at low luminosities is due to their definition. Class 0 and class I sources do essentially occupy the same region in the parameter space, with the class 0 sources possibly having for given internal luminosity slightly higher aperture masses than class I sources.

In particular, the classes 0 and I are not separated by the class boundary suggested by Motte & André (2001), $M_{4200\text{AU}} \approx 0.1 M_{\odot} (L/L_{\odot})^{0.6 \text{ to } 1.0}$. This law reflects the conceptual definition of class 0 sources as YSOs which have accreted less than half of their final mass (Andre et al. 1993). Thus the envelope mass in class 0 sources, as approximated by $M_{4200\text{AU}}$, must exceed the stellar mass. Depending on the exact form of the YSO mass-luminosity relation, Motte & André suggest this boundary to be given by the above relation (see Andre & Montmerle

1994 and Andre et al. 2000 for further details). This boundary is indeed observed to well separate class 0 and class I sources in the Ophiuchus molecular cloud complex and some isolated cores (Visser et al. 2002), but it fails to do so for sources in the Taurus cloud (Motte & André 2001) and Perseus (Hatchell et al. 2007).

To be precise, within the observational errors all class 0 sources in the c2d MAMBO sources do indeed have aperture masses exceeding $0.1 M_{\odot} (L/L_{\odot})^{0.6 \text{ to } 1.0}$, just as expected. However, the class I YSOs in our survey do not generally fall short of the conceptual luminosity-dependent mass limit for class 0 sources. In this respect they are different from the aforementioned class I sources in Ophiuchus that fulfill this limit. For comparison, like ours, also class I YSOs in Taurus (Motte & André 2001) and Perseus (Hatchell et al. 2007) do not conform to this conceptual boundary. This suggests that the stars in our sample reside in regions that are more similar to regions of distributed star formation, like Taurus, than to regions of clustered star formation, like Ophiuchus.

The failure of the conceptual class boundary to separate sources of class 0 and I and the absence of clear evolutionary trends between them in Fig. 6 suggests that either the concept of infrared classes, our general understanding of YSO evolution as a linear sequence of states in the $L_{\text{int}}-M_{4200\text{AU}}$ parameter space, or both, need some revision. Also, $M_{4200\text{AU}}$ might simply not be well suited to gauge the mass available for accretion. This would, however, require accretion to proceed in a manner very different from the collapse of self-similar isothermal spheres: here steadily $M_{4200\text{AU}}$ decreases with time, and independent from the final size of the infalling envelope (even if eventually $> 4\ 200$ AU) $M_{4200\text{AU}}$ would at least generally probe the mass evolution of the envelope. Whatever, the fact that similar studies of different regions find different relations between YSO and envelope properties suggests that the environment influences these relations.

5.4.3. Bolometric Temperatures and Luminosities

Figure 7 presents the bolometric temperatures and luminosities for sources in the c2d MAMBO survey. It shows that for a given star the luminosities are higher and the bolometric temperatures are lower when these properties are inferred from IRAS data instead of Spitzer observations. This is just as expected, given IRAS' better spectral coverage of the dust emission peak at sub-millimeter wavelengths.

This diagram shows that on average L_{bol} increases with increasing T_{bol} . This trend is in particular pronounced when looking at the lower envelope of the data points. However, it is likely that this is to a significant extent an observational bias, since faint sources of high bolometric temperature have lower millimetre intensities and are thus less likely to be included in our MAMBO-based source selection. For the same reason in general sources with high bolometric temperatures are less likely to be included. This is at least partially responsible for the sharp drop in the number of sources at $\gtrsim 300$ K.

Class 0 sources are found to have luminosities spanning across more than two orders of magnitude. This demonstrates the diversity of star formation activity in the c2d MAMBO survey. Note that, if sources of similar T_{bol} have similar ages and have luminosities dominated by accretion luminosity (i.e., $L_{\text{int}} \approx GM_{\star} \dot{M}_{\text{accr}}/R_{\star}$, where G , M_{\star} , R_{\star} , and \dot{M}_{accr} are the constant of gravity, the stellar mass and radius, and the accretion rate), then the class 0 sources in the c2d MAMBO survey must differ significantly in their mass-to-radius ratios, their accretion

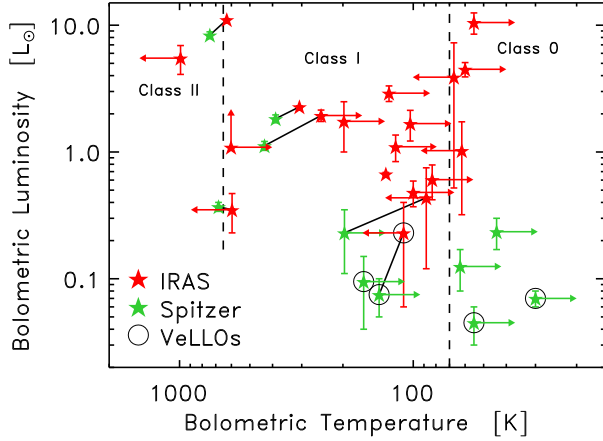


Fig. 7. Bolometric luminosities and temperatures as derived from IRAS and Spitzer (markers of different shade) data. VeLLO candidates are highlighted by circles around the markers, and the YSO class regimes are delimited by vertical dashed lines and labels. Solid lines indicate characterizations of the same star based on different data. For a given source the IRAS data usually indicates lower bolometric temperatures and higher luminosities than the Spitzer data, just as expected given IRAS’ better spectral coverage at long wavelength. Note the range in luminosities for a given class. This indicates that the accretion rates, masses, radii, or all these properties largely vary within the sample, and also a given class, if the luminosities are largely due to accretion.

rates, or both. Enoch et al. (in prep.) find similar luminosity ranges for YSOs in Perseus, Serpens, and Ophiuchus.

5.4.4. Envelope Masses and Bolometric Temperatures

Figure 8 presents bolometric temperatures and aperture masses for the c2d MAMBO sources. This reveals that on average the bolometric temperature decreases with increasing aperture mass. This could be an evolutionary trend. The coolest sources are supposedly the youngest sources, which are expected to be surrounded by significant amounts of circumstellar matter. Our observations are thus consistent with expectations.

However, the large column densities suggested by large aperture masses might lead to low bolometric temperatures because of reddening: photospheric YSO emission might be absorbed at short wavelengths and be re-emitted by the envelope at longer wavelengths. In that case bolometric temperatures would not unambiguously characterize YSO ages, but would partially be due to reddening not related to the time evolution of the source. Our sample is, however, too small to evaluate this issue comprehensively.

Within our survey, VeLLO candidates appear to have for given aperture mass the lowest bolometric temperature observed. However, this likely reflects the definition of VeLLOs as objects of low internal luminosity, since for fixed millimetre flux (or $M_{4200\text{AU}}$) the bolometric temperature decreases with decreasing luminosity.

Note that all the “usual” young YSOs with $T_{\text{bol}} < 300$ K have $M_{4200\text{AU}} > 0.3 M_{\odot}$, just as already discussed in Sec. 5.3.4. Also note the aperture masses of $M_{4200\text{AU}} \gtrsim 0.5 M_{\odot}$ for the YSOs in L1228 P1 and Bern48 P1 are unusually large, given their bolometric temperatures of ≥ 300 K. It is not clear how such sources of a relatively late evolutionary stage can maintain such massive envelopes, if our mass estimates are correct.

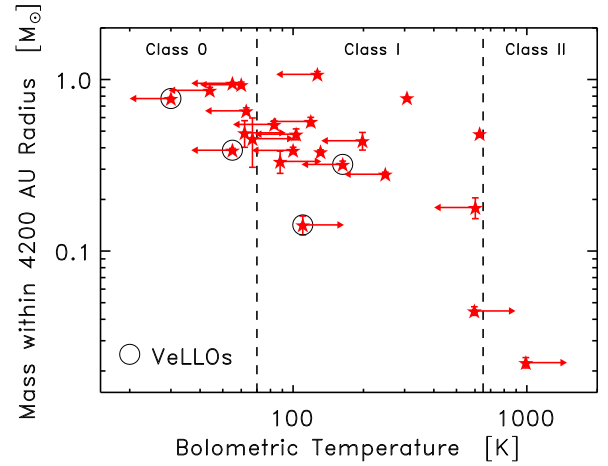


Fig. 8. Bolometric temperatures and mass within 4200 AU radius for the YSOs in the c2d MAMBO sample. Candidate VeLLOs are highlighted by circles around the markers, and the YSO class regimes are indicated by vertical dashed lines and labels. The general trend of increasing bolometric temperature with decreasing aperture mass might be an evolutionary effect. It could, however, also indicate that low bolometric temperatures are partially due to reddening by extinction and re-emission at longer wavelength, since both should scale with aperture mass. VeLLOs notably have the lowest bolometric temperature for given aperture mass, but this is likely simply reflects their definition as objects of low luminosity.

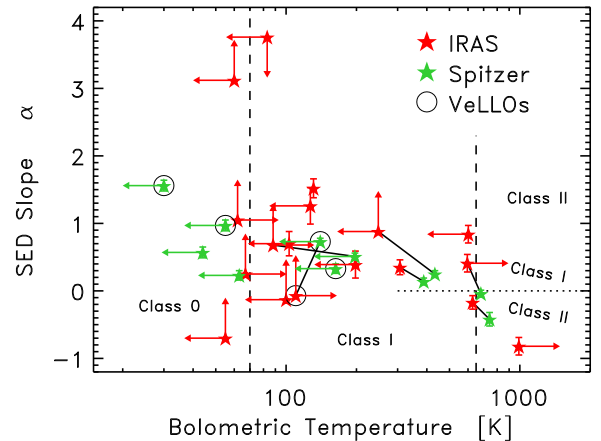


Fig. 9. SED slope versus the bolometric temperature. See Fig. 7 for the symbols used. Note that IRAS data usually implies SED slopes larger than, and bolometric temperatures smaller than, those derived from Spitzer data, just as expected from IRAS’ better spectral coverage at long wavelengths. Note that class assignments on basis of bolometric temperature and spectral slope do agree.

5.4.5. Assignment of Infrared Classes

The above discussion often assumed that the bolometric temperature uniquely parameterizes the YSO age. This is not obvious, and possibly not true. We briefly summarize hints on this issue from the c2d MAMBO data.

Figure 9 presents the relation between bolometric temperature and SED slope near $10 \mu\text{m}$ wavelength. The slopes derived from IRAS and Spitzer data ($\alpha_{12\mu\text{m}}^{25\mu\text{m}}$ and $\alpha_{3.6\mu\text{m}}^{24\mu\text{m}}$, respectively) do slightly differ in their definition (see Sec. 4). In 4 out of 5 cases

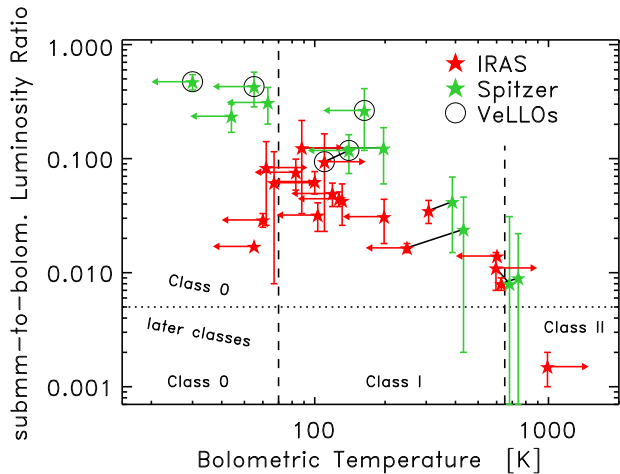


Fig. 10. Submillimetre-to-bolometric luminosity ratio versus the bolometric temperature. See Fig. 7 for the symbols used. Vertical dashed lines indicate ranges for YSO classes assigned on basis of T_{bol} , while the horizontal dotted line (described by inclined labels) gives the boundary for the class assignment based on the luminosity ratio following Andre et al. (1993). It's disagreement with T_{bol} -based class assignments is likely caused by positive biases in our evaluation of the submillimetre luminosity.

$\alpha_{12\mu\text{m}}^{25\mu\text{m}} > \alpha_{3.6\mu\text{m}}^{24\mu\text{m}}$ for sources detected by both missions. Most sources in our survey have spectral slopes of $0.0 \leq \alpha \leq 1.5$. We find a general trend of increasing α with decreasing T_{bol} across the whole sample. No such trend is, however, visible when looking at class I sources only (class 0 sources are usually not expected to have particular values of α). Note that class assignments on basis of bolometric temperature or spectral slope are consistent with each other within our sample. Given the expected uncertainties, all sources in our sample are consistent with having $T_{\text{bol}} < 650$ K (i.e., being a class 0 or class I source) when $\alpha > 0$ (note, however, that classification schemes never required class 0 to have $\alpha > 0$), and $650 < T_{\text{bol}}/\text{K} < 2880$ (i.e., being a class II source) when $0 > \alpha > -2$, just as postulated in class definitions based on T_{bol} and α (Chen et al. 1995; Lada 1987). Similar trends are found in the c2d SED studies of the Ophiuchus, Perseus, and Serpens molecular cloud complexes by Enoch et al. (in prep.).

Also note that all IRAS sources not detected by MAMBO (Table 7) are consistent with having negative spectral indices and therefore belonging to late YSO stages (if they are YSOs and not background galaxies). This fits well into a picture in which YSOs with negative spectral slopes are evolved and not anymore surrounded by dust.

Our submillimetre-to-bolometric luminosity ratios (Fig. 10; also see Tables 8 and 9) and T_{bol} -based class assignments are not well in accord with the original initial observational criterion to identify class 0 sources given by Andre et al. (1993), i.e., a luminosity ratio $\gg 0.005$; using the latter criterion, all but one of our YSOs would be in the class 0 category. Note, however, that the submillimetre part of our SEDs is the worse constrained one and that the luminosities are uncertain by a factor 2 (Sec. 4.2). Anyway, submillimetre luminosities of 0.01 to 0.1 for $T_{\text{bol}} \approx 70$ K have been observed before (Young & Evans 2005) and also Visser et al. (2002) found that essentially all YSOs in their sample would be of class 0 if the class is assigned based on a luminosity ratio > 0.005 (see Hatchell et al. 2007 for a further example; note that both studies do, like us, have

SEDs not well sampled at submillimetre wavelengths). The role of the submillimetre-to-bolometric luminosity ratio for classification purposes thus needs to be further studied with better wavelength coverage.

Also, the bolometric temperature might not uniquely parameterize age, as the aforementioned trend of decreasing bolometric temperature with increasing aperture mass might indicate.

It has also been speculated that actual class I sources have SEDs like class 0 sources if the circumstellar disk-envelope structure is seen edge-on (e.g., Whitney et al. 2003 for an overview). Interestingly, the class 0 source in IRAS05413 P3 appears to have such a particular geometry; here the outflow has an estimated inclination of $\geq 85^\circ$ with respect to the line of sight, suggesting that a YSO disk is seen nearly edge-on (Claussen et al. 1998). This geometry might explain why IRAS05413 P3, being a class 0 source marginally violating the conceptual mass-luminosity limit by Motte & André (2001), has an extreme position in Fig. 6.

In summary, class assignments based on T_{bol} are consistent with those based on α , and either is fine to classify sources of a relatively late evolutionary stage. One needs to employ the bolometric temperature though if intending to study deeply embedded sources, for which the spectral index criteria do not hold. The T_{bol} thus appears to be more versatile, but requires a well sampled SED at long wavelengths.

In contrast, assignments based on the $m_{4200\text{AU-to-}L_{\text{int}}}$ ratio are in conflict with those based on T_{bol} . A T_{bol} -based classification does however lead to a larger spectrum in evolutionary states: T_{bol} indicates class 0 and class I sources, while the $m_{4200\text{AU-to-}L_{\text{int}}}$ ratio suggests that our sample essentially only contains class 0 objects. Since the latter seems somewhat unrealistic, the larger range in assigned classes suggests that the bolometric temperature is more useful for classification.

Similarly, the submillimetre-to-bolometric luminosity ratio assigns all but one YSO to the class 0. Again, T_{bol} -based classification appears superior to the one based on luminosity ratios. This might, however, in part be due to uncertainties in our SEDs at wavelength 100 to 1000 μm and should not be generalized. Still, for data like ours luminosity ratios are barely useful.

Anyway, it is not clear which existing YSO class assignments best characterize the evolutionary ages of YSOs. In this respect it might be useful (see, e.g., Robitaille et al. 2006) to distinguish between YSO *classes*, that describe and organize observational properties such as the bolometric temperature, and evolutionary *stages*, that characterize physical properties such as the presence of envelopes and disks.

5.4.6. YSO Offsets

The spatial resolution of MAMBO and Spitzer allows to test whether YSOs actually reside in the very center of their natal dense core. The discovery of offsets would be very interesting, since present YSO evolutionary scenarios do not predict them. As shown in Table 13 we do, however, not find offsets at a significant level.

For this search the YSO positions are taken to be those of Spitzer counterparts listed in Table 9. Otherwise the positions of the 2MASS counterparts given in Table 8 are used. For YSOs with non-c2d Spitzer data only, Gaussian curves were fitted to the Spitzer images (see notes to Table 13). The dust intensity peak positions are derived as the intensity-weighted mean position of the pixels above 90% peak intensity. The offsets are given in Table 13. The uncertainty in the dust emission peak position

Table 13. YSO offsets from dust emission peaks. For each dust emission peak, and related subcore, associated with a YSO listed in Tables 8 and 9 we give the chosen reference source (preferentially seen by Spitzer) and the observed offset and position angle (i.e., position of star w.r.t. the dust emission peak).

Field	Peak	Position Reference (see notes)	Offset arcsec
L1521F	P1	SSTc2d J042839.0+265135	5.0 ± 0.6
B18-1	[P5]	SSTc2d J043215.4+242859	1.1 ± 0.6
B18-4	P1	IRAC	2.2 ± 0.6
TMC1-1C	P3	SSTc2d J044138.8+255627	3.3 ± 2.5
TMC-1	P2	SSTc2d J044112.7+254635	3.1 ± 0.6
IRAS05413	P2	MIPS	3.8 ± 0.5
	P3	MIPS	3.6 ± 0.3
CB188	P1	SSTc2d J192014.9+113540	2.3 ± 0.7
L673-7	P1	SSTc2d J192134.8+112123	2.1 ± 0.9
L1148	P1	SSTc2d J204056.7+672305	7.6 ± 2.7
L1082A	P1	2MASS J20531346+6014425	2.7 ± 0.9
L1228	P1	SSTc2d J205712.9+773544	0.8 ± 0.1
Bern48	P1	SSTc2d J205914.0+782304	0.8 ± 0.3
L1172A	P2	MIPS	7.3 ± 1.4
L1177	P2	IRAC	2.9 ± 0.1
L1021	P1	2MASS J21212751+5059475	2.5 ± 0.8
L1014	P1	SSTc2d J212407.5+495909	2.2 ± 1.3
L1251A	P3	SSTc2d J222959.5+751404	8.8 ± 1.3
	P4	SSTc2d J223031.8+751409	1.2 ± 0.2
	P5	SSTc2d J223105.6+751337	4.3 ± 0.8

Notes: Position for B18-4 P1 (average of Gaussian fits to all IRAC bands) is 04:35:35.4, 24:08:20.2 (J2000.0); for IRAS05413 P2 (from fits to MIPS band 1) it is 05:43:46.264, -01:04:43.68; for IRAS05413 P3 (from MIPS band 1) it is 05:43:51.367, -01:02:52.76; for L1172A P2 (from MIPS band 1) it is 21:02:21.118, +67:54:20.17; and for L1177 P2 (from IRAC band 4 only, where the significant scattering is supposedly lowest) it is 21:17:38.650, +68:17:33.27.

due to noise is derived from Monte-Carlo experiments with artificial noise, as explained in Sec. 3.2. The typical pointing uncertainty of $3''$ has to be further added to derive the typical total dust emission position uncertainty.

We do not find significant YSO offsets in our sample. In a first cut we find two YSOs with offsets exceeding the expected uncertainty by a factor 2. However, for one of them (L1251A P3) the pointing corrections were up to $5''.9$. For the other one (L1172A P1) the position offset exceeds the uncertainty by a factor 2.2; this is marginally significant, and should be followed up at higher resolution, but not conclusive evidence for a YSO leaving its natal core. Our data thus indicates that generally YSOs reside in the centers of their envelopes, with core-YSO relative motions not e.g. significantly affecting the accretion histories. This is in accord with studies of core-YSO-offsets in Perseus (Jørgensen et al. 2007; Enoch et al., in prep.) and Ophiuchus (Jørgensen et al., in prep.).

Note, however, that our data does not reveal the offset between the L1014 P1 column density peak and the embedded candidate VeLLO found by Huard et al. (2006) on basis of extinction maps, although their offset of $10''$ to $15''$ should be easily detected by MAMBO. Huard et al. speculate that this might be because of internal heating of the L1014 core, which is supposed to shift the dust emission peak away from the column density peak and towards the embedded source (see Young et al. 2004a and Wu et al. 2007 for SCUBA and SHARC II data on L1014, respectively). Their extinction map is, however, not well sampled

towards the VeLLO position, which introduces uncertainties to their map.

5.5. Formation and Evolution of VeLLOs

The c2d MAMBO survey provides an opportunity to investigate how candidate VeLLO natal cores are different from starless and YSO cores. For the first time it allows a direct comparison of the dust emission properties of all three kinds of objects. We here discuss whether, and if yes how, VeLLO cores differ from starless and YSO cores.

5.5.1. Masses and Total Radii of VeLLO Cores

Figures 3 and 4 show that VeLLO candidate cores cannot be distinguished from starless cores in terms of mass, column density, and total effective radius. In particular, three of the VeLLO cores have column densities, masses within the 4 200 AU aperture, and masses within the 50% intensity contour — all properties naively associated with a good chance for star formation — much lower than the starless peaks B18-1 P3 and B18-4 P2. Note that this observation is in conflict with some naive expectations for properties of starless and YSO cores: a picture of dense core evolution in which any dense core begins to actively form stars once it exceeds some fixed limit in mass, density, or both, is inconsistent with our data. Section 5.3.4 discussed this and other data in the context of necessary, but not sufficient, conditions for active star formation.

Note that 3 out of 4 VeLLO candidates are consistent with fulfilling these conditions (i.e., in Fig. 4, only the candidate VeLLO in L1148 resides in a region entirely devoid of normal YSOs, and thus also misses the theoretical star formation criterion by a large margin). In this respect *the notion that VeLLOs reside in cores not expected to be able to form stars might be wrong*. However, it might be that some VeLLOs can conceptually be characterized as YSOs forming in cores that only barely fulfill the necessary conditions for active star formation, as observed for 3 out of the 4 candidate VeLLOs in our sample. The latter might suggest a special route of star formation for some VeLLOs.

The VeLLO candidate in L1148 P1 poses a real challenge to present star formation scenarios, since it does not fulfill the necessary conditions for star formation to occur. This source might thus either hint at a particular mode of star formation, where the conditions derived in Sec. 5.3.4 do not apply, or this YSO (recent IRAM Plateau de Bure imaging indicates either a jet or a disk; Kauffmann et al., in prep.) is in an advanced evolutionary stage in which the natal core's structure does not resemble the initial one.

5.5.2. Peak Radii of VeLLO Cores

Most VeLLO candidate cores have peak density profiles flatter than $\rho \propto r^{-2}$, since their effective radius at 70% peak intensity is (with the exception of the candidate VeLLO in L673-7 P1) significantly larger than the one of a $\rho \propto r^{-2}$ density profile smeared by a $20''$ beam (i.e., $10''.7$). It is beyond the scope of the present paper to explore whether this flattening is because the density profile becomes similar to $\rho \propto r^{-3/2}$, as found for infalling envelopes around YSOs (see Evans 2003 for a review), or is due to a region of spatially constant density, as found for starless dense cores (e.g., Ward-Thompson et al. 1999). Note, however, that Crapsi et al. (2004) show that MAMBO maps for L1521F

are consistent with a functional form for the central flattening as found for starless cores. The high resolution extinction data for L1014 obtained by Huard et al. (2006) has not been analysed in such a fashion.

Compared to starless cores, candidate VeLLO natal cores do, however, have unusually steep dust emission intensity profiles, as e.g. probed by the effective radius of a dust emission peak at its 70% intensity level. For given aperture mass, VeLLO cores (with the possible exception of the uncertain radius of L1148 C1) do have smaller effective radii than most starless cores (Fig. 5), even when correcting for steepening due to internal heating by the VeLLO (for this we first use the luminosity-dependent beam-averaged dust temperature [Eq. 8] to predict the peak intensity for dust of 10 K, and then evaluate the effective radius at 70% of this intensity).

The unusually steep dust intensity profiles of candidate VeLLO natal cores thus indicate unusually steep column density profiles. This distinguishes them from most starless cores in our sample. Steep radial profiles in the density, and therefore also in the column density, are indeed expected for dense cores temporally near (e.g., McKee & Holliman 1999) or after (see Larson 2003 for a review) the onset of gravitational collapse. Density gradients in VeLLO cores are consistent with this theoretical picture. VeLLO candidates also seem to have unusually large central densities, when compared to starless cores (Fig. 5). This is again in line with the above theoretical expectations.

The steeper density profiles and higher central densities of candidate VeLLO natal cores suggest that they are temporally closer to the onset of gravitational collapse than most starless cores. *It thus appears that VeLLO cores are structurally different from most starless cores in that their density structure is more evolved.* This was first suggested by Huard et al. (2006), on basis of surface-to-center density contrasts for L1014 P1 that exceed those of previously studied starless cores. Also, all candidate VeLLOs (possibly excluding L1148 P1) have effective radii at the 70% dust emission peak intensity level below 4 800 AU, which Crapsi et al. (2005) suggested as an indicator of an advanced evolutionary stage of a core. This might bear important hints on the nature of VeLLOs.

5.5.3. VeLLO Offsets from Column Density Peaks

Huard et al. (2006) found that the candidate VeLLO in L1014 is offset by 10'' to 15'' from the apparent natal column density peak, L1014 P1. If L1014-IRS does indeed drift away from its natal core, and therefore away from the mass reservoir available for accretion, this might explain the low rate of accretion onto L1014-IRS inferred by Bourke et al. (2005). Low accretion rates could in turn explain the low luminosities of VeLLOs. They would also suggest low, and possibly substellar, final masses for VeLLOs with low accretion rates (Bourke et al. 2005). However, as already discussed in Sec. 5.4.6, we do not find any significant offsets. Our data might not rule out such offsets though, since the MAMBO data might not be suited to search for offsets (Sec. 5.4.6).

6. Summary

We present a dust continuum emission imaging study of a comprehensive sample of isolated starless and YSO-containing dense molecular cores (including 4 candidates of the enigmatic VeLLOs), the c2d MAMBO survey. This survey is technically different from previous ones in that it is

- more sensitive to faint (few mJy per 11'' beam) extended ($\geq 5'$) emission than in previous surveys thanks to modern instrumentation and a newly devised data reduction strategy (Sec. 2.3.1), resulting in
- very rich structure compared to existing surveys, since we detect faint extended emission from sources otherwise only detected in their most prominent intensity peaks.

We combine our MAMBO data with Spitzer and IRAS data to fully exploit our dust emission maps (Sec. 4). This also reveals 4 previously unreported YSOs (Table 11), including one VeLLO candidate and 2 class 0 sources. Our analysis (Sec. 5) first deals with the general structure and evolution of dense cores (Secs. 5.1 to 5.3):

- characteristic values for the mass within peak-centered apertures of 4 200 AU diameter are similar to those of singular isothermal spheres, suggesting that cores prefer a near-critical state (with respect to gravitational collapse; Sec. 5.1.3 and Fig. 3 [c]);
- subcores (i.e., extended substructure within cores) are usually elongated, implying that they are not hydrostatic objects supported by isotropic pressure (Sec. 5.1.4 and Fig. 3 [d]);
- rough density estimates indicate central H₂ densities between 10⁴ and 10⁶ cm⁻³ while the density frequency distribution suggests that cores in our sample are not in free fall (Sec. 5.3.1 and Fig. 5);
- comparison with criteria by Crapsi et al. (2005) reveals 5 candidate evolved cores (plus 3 candidates of lesser quality), out of which 3 are reported here for the first time, but the failure of these criteria to highlight candidate VeLLO cores with active star formation casts some doubt on them (Sec. 5.3.2);
- rough estimates for the dense core mass available for accretion onto a forming YSO yield values of order 10% of the dense core total mass (with an uncertainty of a factor of several), suggesting that the star formation efficiency is of the same order (which questions studies relating the mass functions of cores and stars; Sec. 5.3.3 and Fig. 4 [c]);
- there are necessary (but not sufficient) conditions which a dense core must fulfill in order to be able to actively form a star (i.e., a core fulfilling these can contain a YSO, but does not need to), which can be understood in the framework of quasi-static dense core models (Sec. 5.3.4 and Fig. 4); and
- diverse biases can and do introduce spurious features into the data, requiring care when interpreting the observations.

We then specifically turn to young stellar objects in our sample, where we in particular compare various methods to assign SED classes (Sec. 5.4):

- class assignments based on the bolometric temperature are in conflict with those based on the comparison of YSO luminosities and envelope masses (Sec. 5.4.2 and Fig. 6);
- classes assigned on the basis of T_{bol} and SED slopes agree well, i.e., the data is consistent with $\alpha \geq 0$ for $T_{\text{bol}} \leq 650$ K (Sec. 5.4.5 and Fig. 9);
- among the class assignment methods used in the present study, only the one based on bolometric temperatures implies a reasonable range of evolutionary stages in our sample and is also well applicable to deeply embedded sources (Sec. 5.4.5);
- disagreement of the T_{bol} -based class assignments with those from YSO luminosities and envelope masses suggests that the environment has an impact on YSO evolution since

these assignments agree in other regions (like the Ophiuchus molecular cloud; Sec. 5.4.2 and Fig. 6);

- there are no significant offsets between YSOs and their natal dense cores, implying that core-star relative motions do not have a significant influence on YSO evolution via the accretion history (Sec. 5.4.6 and Table 13); and
- assuming that the bolometric temperature roughly characterizes YSO ages, the large range of bolometric luminosities (two magnitudes) in early YSO stages implies a large variation of mass-to-radius relations, accretion rates, or both, in our sample.

The combined information on cores in general and YSOs in particular can then be used to assess the relevance of some characteristics of candidate VeLLO natal cores (Sec. 5.5):

- 3 out of 4 VeLLO candidate cores are consistent with fulfilling the above necessary conditions for active star formation, suggesting that the notion that VeLLOs form in cores not expected to be able to form stars is wrong, but some do only barely fulfill the requirements for active star formation, suggesting that some VeLLOs might form in cores just barely able to produce stars, possibly via a particular mode (Sec. 5.5.1);
- candidate VeLLO natal cores have density profiles steeper than and central densities larger than most starless cores, suggesting that VeLLO candidate cores are structurally different from starless ones (Sec. 5.5.2); and
- given our failure to detect core-VeLLO offsets, low accretion rates because of core-star motion as an explanation for the low VeLLO luminosities are not consistent with our observations (Sec. 5.5.3).

In this respect our study — the first one to compare candidate VeLLO cores based on a homogeneous dataset — helps to significantly further our understanding of the nature of VeLLOs.

Acknowledgements. We are grateful to A. Crapsi for sharing with us some of the MAMBO data used in this study, to IRAM's Granada staff for their support and hospitality during the long observing runs, and to M. Enoch, J. Jørgensen, and M. Dunham for access to results in advance of publication. We are indebted to an unusually thorough and concise anonymous referee, who helped significantly in making the paper more readable. Support for this work, part of the Spitzer Legacy Science Program, was provided by NASA through contracts 1224608 issued by the Jet Propulsion Laboratory, California Institute of Technology, under NASA contract 1407. Additional support came from NASA Origins grants NNG04GG24G and NNX07AJ72G to NJE. CWL acknowledges support by the KOSEF R01-2004-000-10513-0 program. JK is particularly thankful to the constant encouragement by K. Menten and M. Walmsley during the course of this study. This study had not been possible without the MAMBO bolometer build by E. Kreysa, the MOPSI software developed by R. Zylka, and the IRAM 30m-telescope maintained by IRAM's Granada staff. We thank the Lorentz Center in Leiden for hosting several meetings that contributed to this paper.

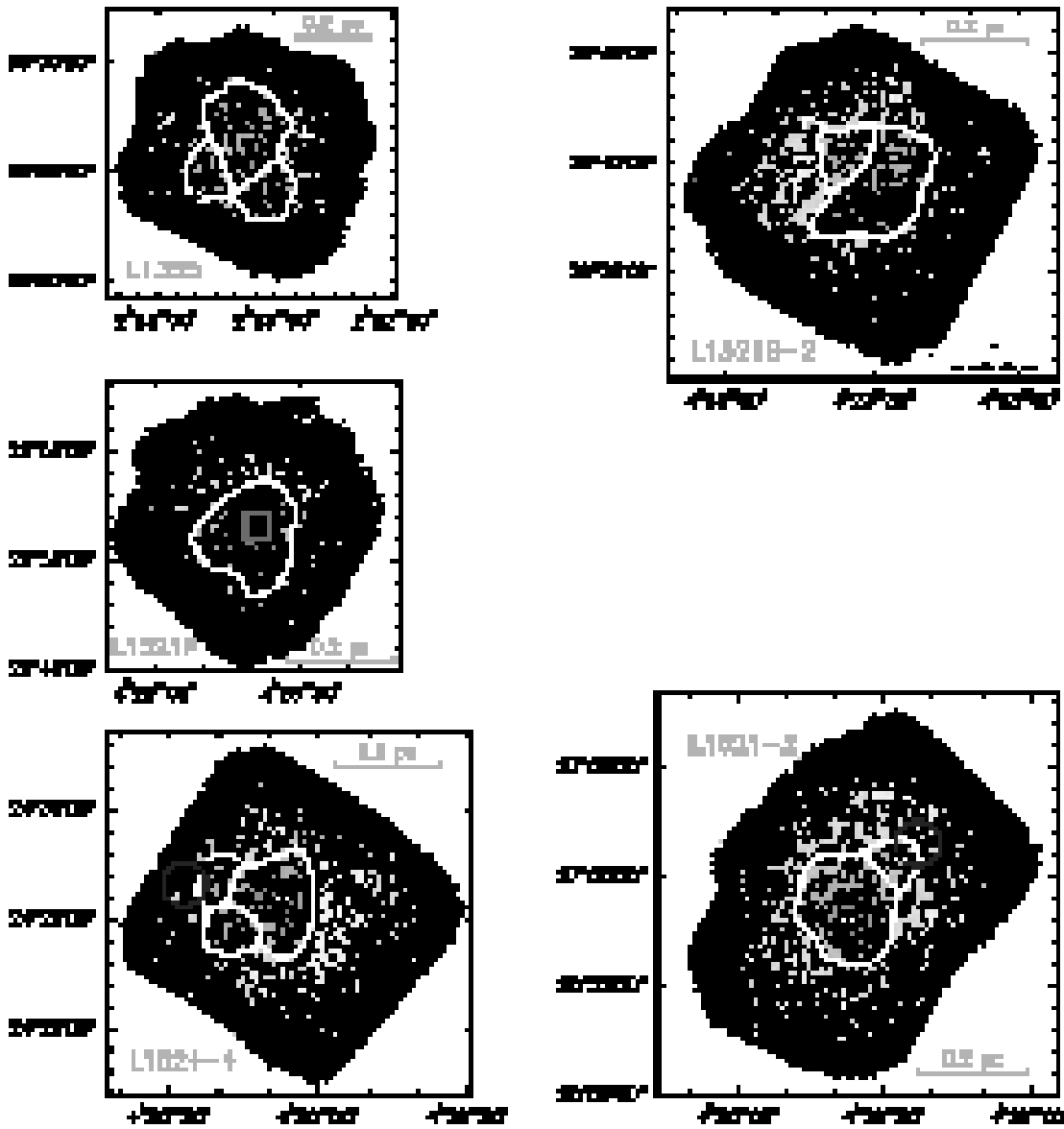


Fig. 1. Maps of the sources in the c2d MAMBO survey after smoothing to $20''$ resolution. *Coordinates* are given for J2000.0. The sources are roughly ordered in sequence of increasing right ascension. *Solid and dotted black contours* are drawn for positive intensities and intensities ≤ 0 mJy beam $^{-1}$, respectively. Contours start at zero intensity and are spaced by ± 3 mJy per $11''$ beam; this corresponds to the noise level in the map center times a factor ≈ 2 to 3 (Table 2). Above 15 mJy beam $^{-1}$, indicated by a *thick solid contour*, the contour spacing is 5 mJy beam $^{-1}$. *Gray shading* also reflects these intensity variations. *White contours* indicate subcore boundaries, while *crosses* indicate dust emission peak positions. *Horizontal bars* indicate the angular scale corresponding to a scale of 0.2 pc $\approx 40\,000$ AU at the adopted core distances. *Circles and squares* mark the positions of all infrared stars detected by IRAS, and Spitzer stars also detected as MAMBO peaks, respectively. If detected by several missions, IRAS Point Source Catalogue (PSC) positions are used instead of those from the Faint Source Catalogue (FSC), and Spitzer positions are used instead of those listed from IRAS. The IRAS PSC source 20410+6710 in L1148 is not marked since missing Spitzer counterparts indicate that this source is an artifact. [See the alternative URL in the astro-ph comments, and the journal article, for higher resolution maps.]

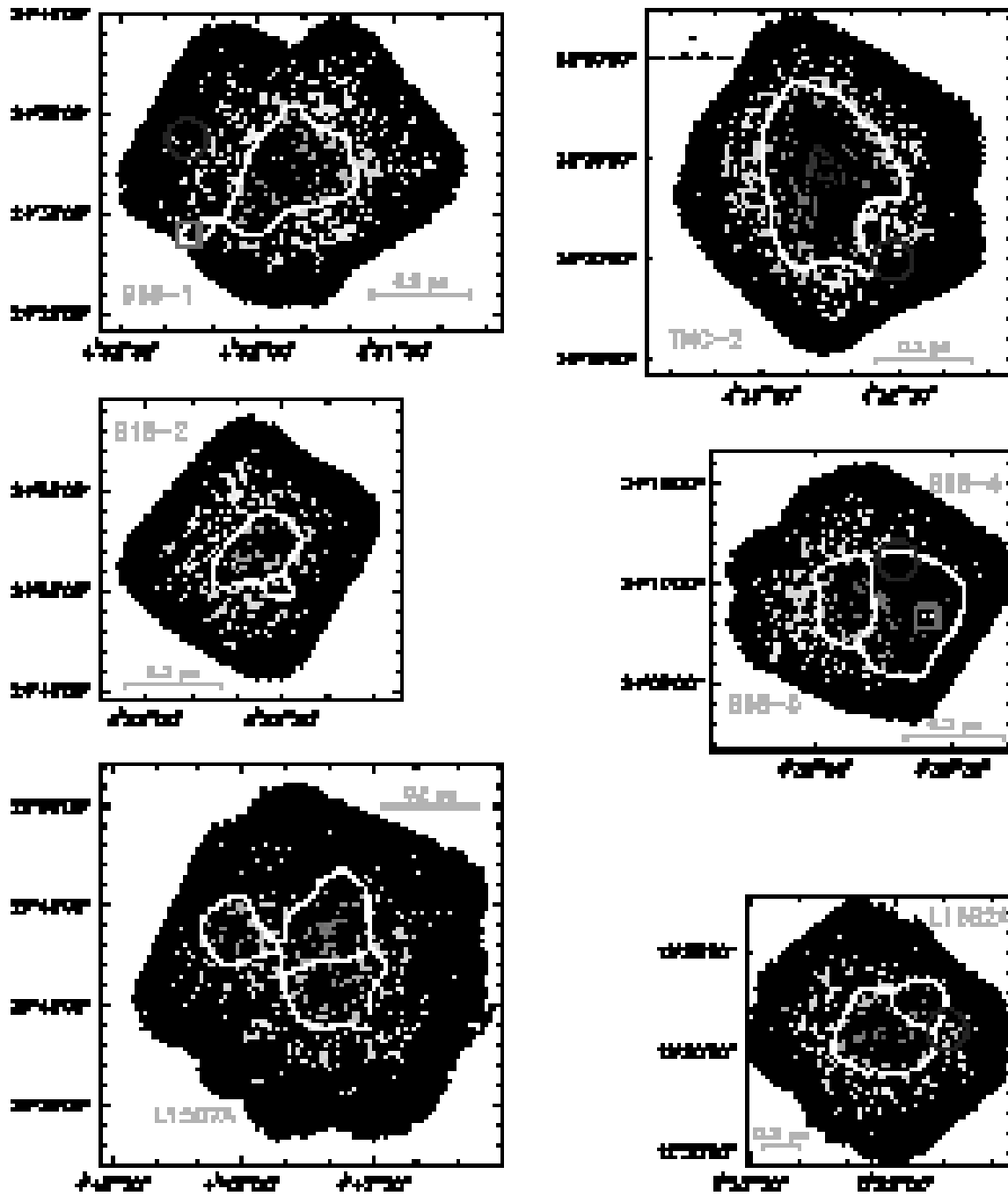


Fig. 1. continued.

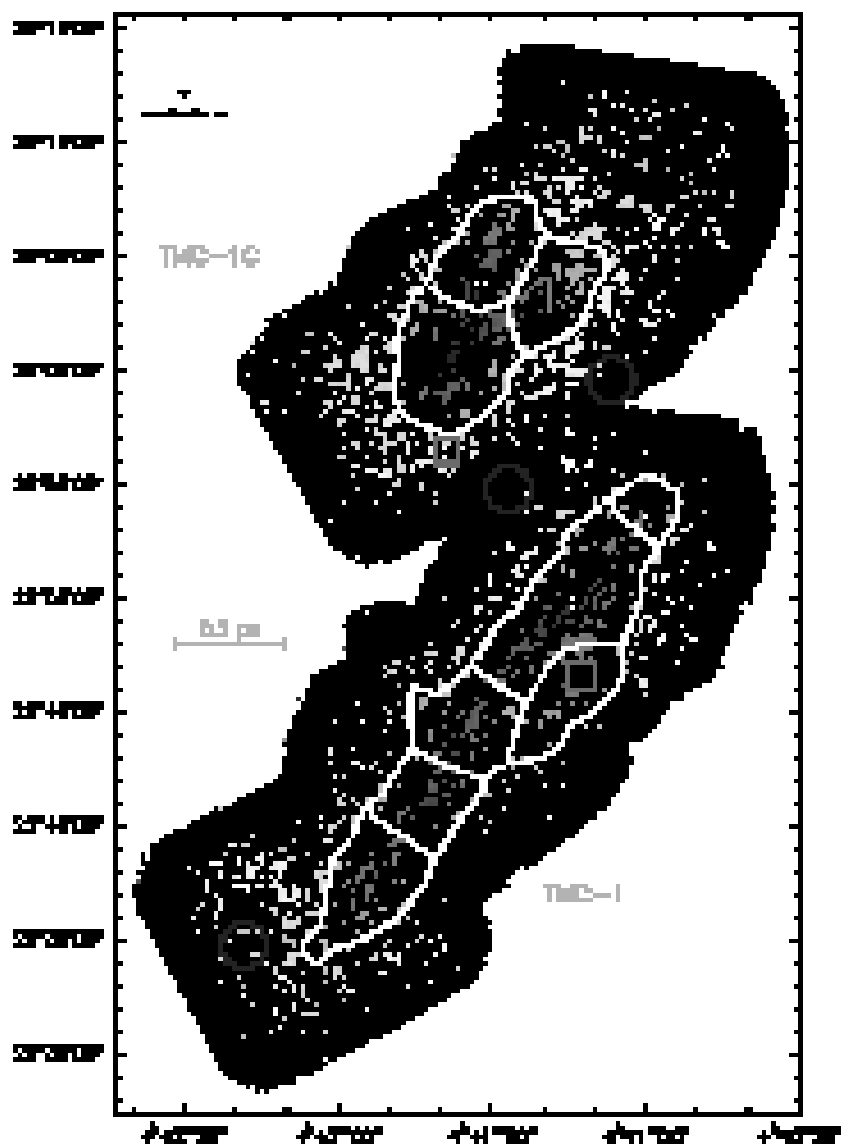


Fig. 1. continued.

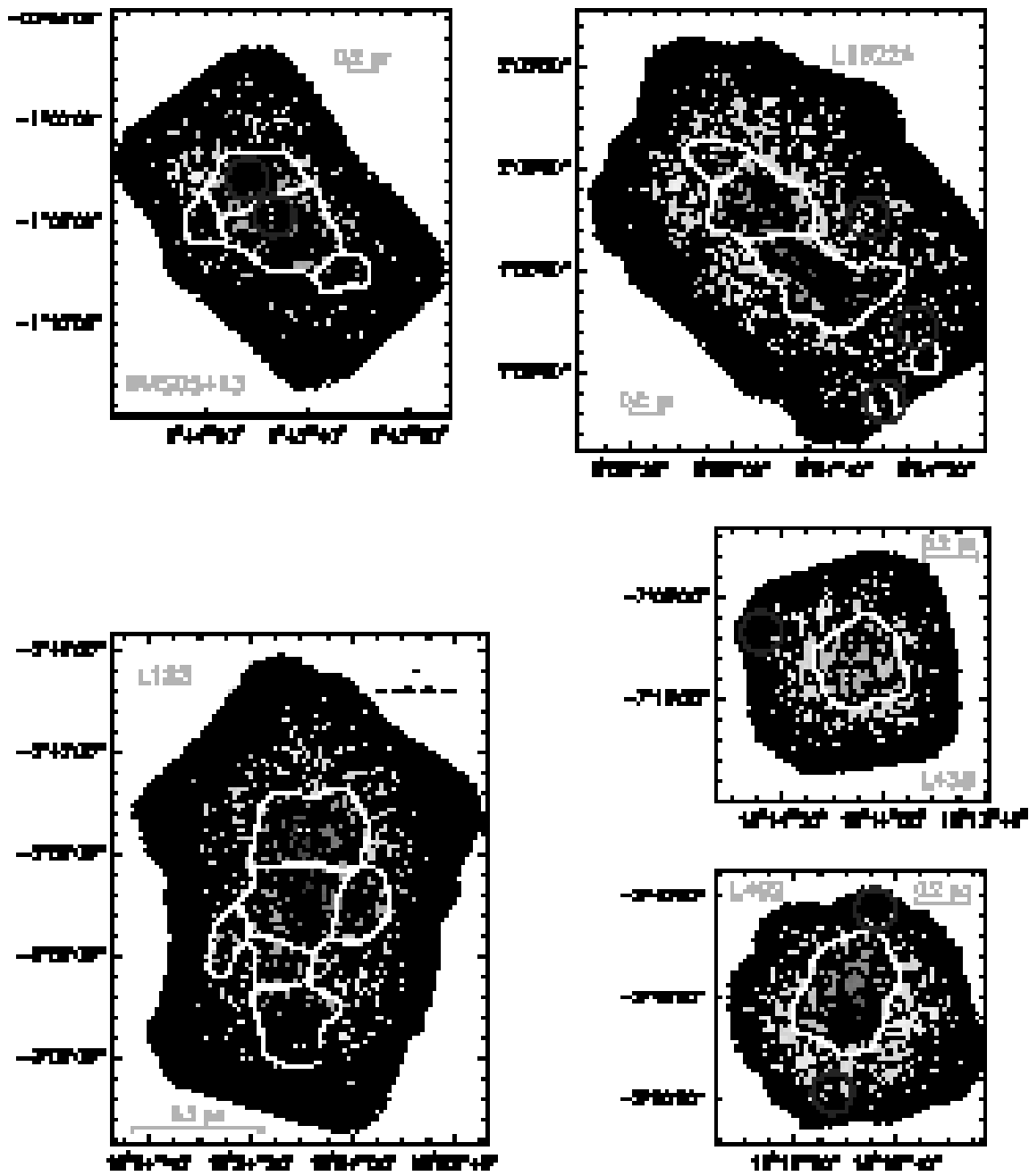


Fig. 1. continued.

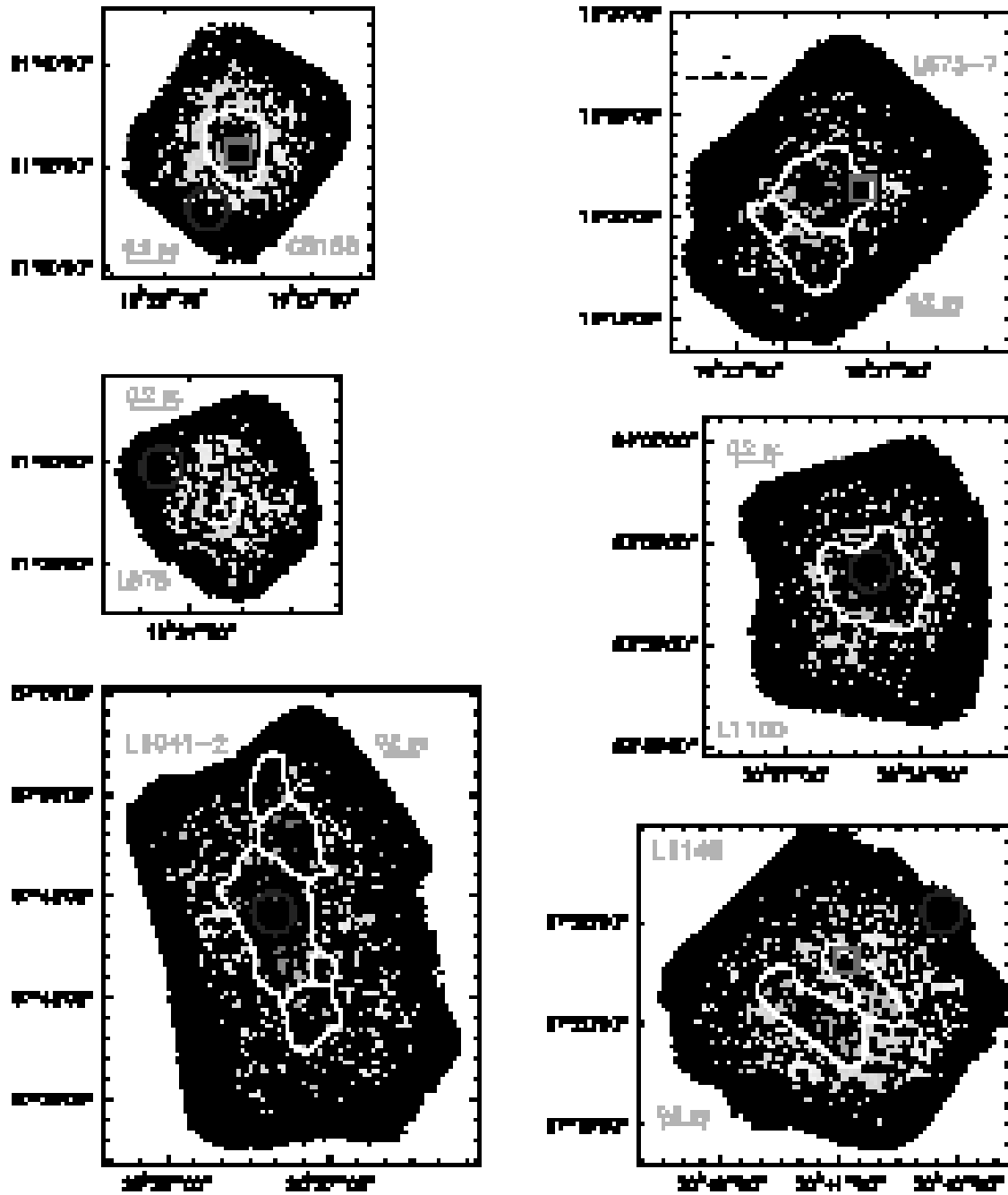


Fig. 1. continued.

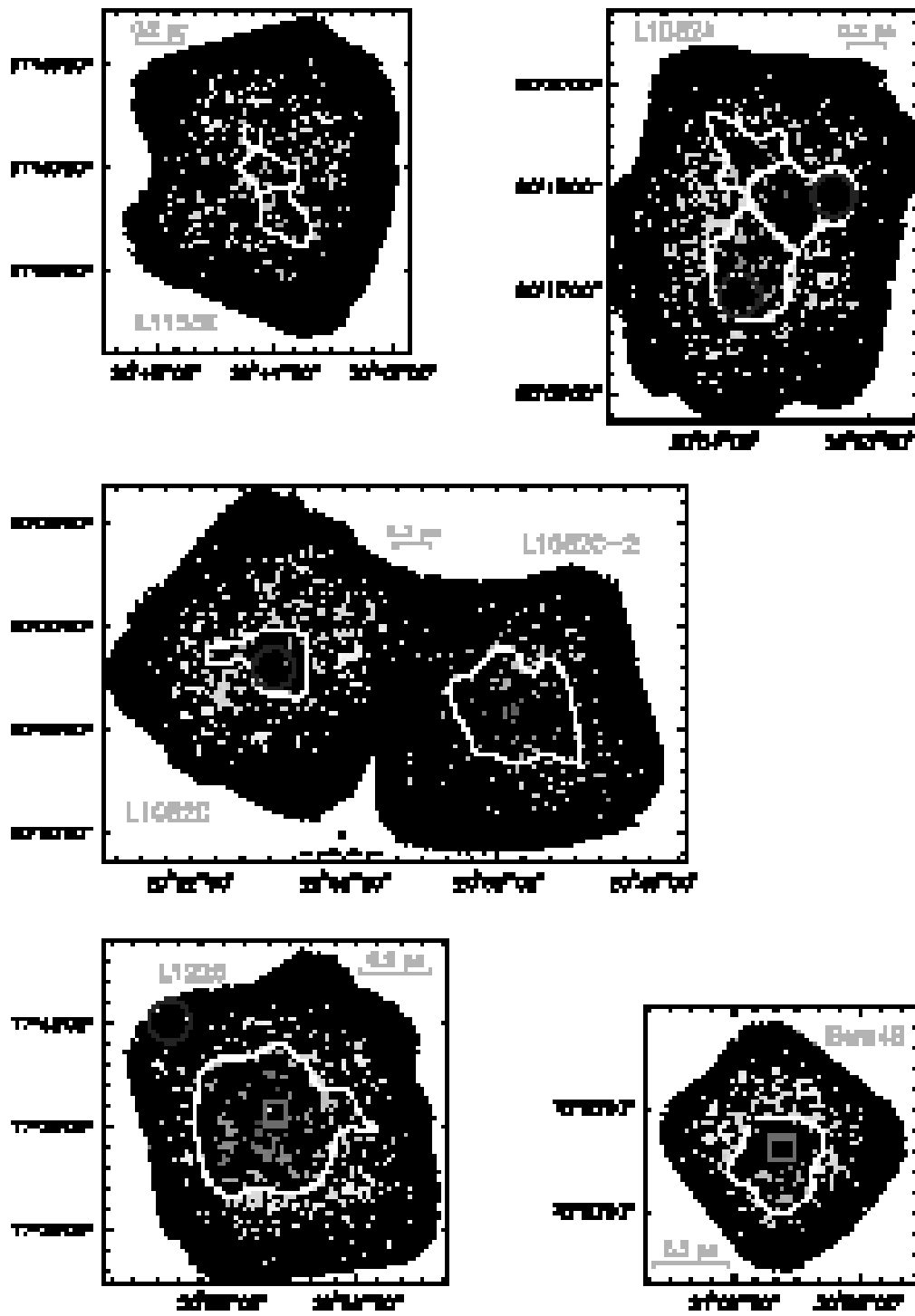


Fig. 1. continued.

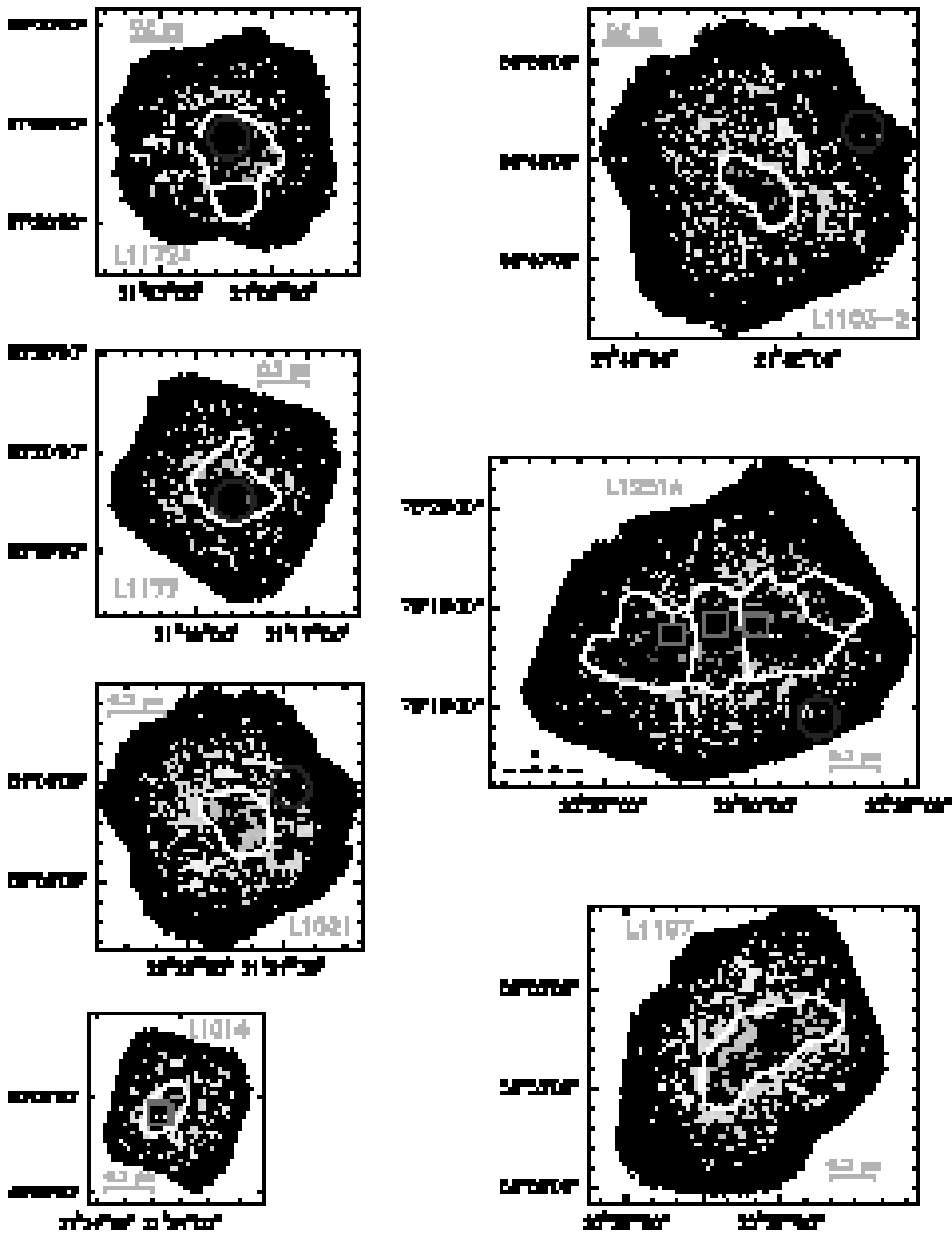


Fig. 1. continued.

Table 3. General data on subcores. Bracketed and starred subcore designations indicate subcores with uncertain properties due to artifacts and subcores with associated YSOs or VeLLOs, respectively. For every subcore the table lists the position of its “center of gravity”, the subcore area and effective radius, the integrated flux density and mass for the whole subcore as well as its area above 50% of its peak intensity, and the maximum signal-to-noise ratio within the subcore boundaries.

Core		α J2000.0	δ J2000.0	A arcmin ²	r_{eff} arcsec		F_{tot} Jy	M_{tot} M_{\odot}	$F_{50\%}$ Jy	$M_{50\%}$ M_{\odot}	$S_{\text{max}}^{\text{beam}}$
L1355	[C1]	02 52 43.2	+68 56 54.0	0.2	14.6	2929	0.04 ± 0.01	0.08 ± 0.02	0.04 ± 0.00	0.07 ± 0.01	4
	[C2]	02 53 02.8	+68 53 54.7	5.0	76.1	15214	0.98 ± 0.05	1.84 ± 0.09	0.70 ± 0.08	1.32 ± 0.16	7
	[C3]	02 53 14.9	+68 57 03.4	13.1	122.4	24473	2.45 ± 0.07	4.60 ± 0.13	1.50 ± 0.17	2.82 ± 0.32	8
	[C4]	02 53 35.5	+68 54 46.5	4.4	71.3	14261	0.73 ± 0.04	1.38 ± 0.08	0.49 ± 0.07	0.92 ± 0.14	5
L1521B-2	C1	04 23 28.0	+26 38 27.0	17.6	142.1	19897	3.09 ± 0.07	2.85 ± 0.06	1.42 ± 0.22	1.31 ± 0.20	11
	C2	04 23 35.5	+26 40 19.5	5.5	79.3	11100	0.74 ± 0.03	0.68 ± 0.02	0.52 ± 0.06	0.48 ± 0.05	8
	[C3]	04 23 42.4	+26 41 38.8	0.6	26.0	3647	0.07 ± 0.01	0.07 ± 0.01	0.06 ± 0.01	0.06 ± 0.01	5
L1521F	C1*	04 28 39.3	+26 51 38.2	17.1	140.1	19609	5.78 ± 0.09	4.60 ± 0.07	0.92 ± 0.09	0.73 ± 0.07	33
L1521-2	C1*	04 29 27.7	+27 00 42.2	3.9	66.8	9346	0.50 ± 0.03	0.46 ± 0.03	0.38 ± 0.05	0.35 ± 0.05	5
	C2	04 29 36.7	+26 58 06.0	18.4	145.0	20304	3.47 ± 0.06	3.19 ± 0.05	1.35 ± 0.15	1.25 ± 0.14	14
L1524-4	C1	04 30 07.9	+24 25 44.5	13.5	124.5	17430	3.11 ± 0.05	2.87 ± 0.05	1.60 ± 0.14	1.47 ± 0.13	13
	[C2]	04 30 17.3	+24 24 34.1	4.7	73.4	10281	0.89 ± 0.04	0.82 ± 0.03	0.72 ± 0.07	0.67 ± 0.06	7
	[C3]	04 30 20.1	+24 26 49.4	3.6	64.1	8975	0.58 ± 0.04	0.54 ± 0.03	0.45 ± 0.06	0.41 ± 0.05	5
B18-1	C1	04 31 55.4	+24 32 33.7	25.2	170.0	23797	6.47 ± 0.06	5.96 ± 0.06	1.29 ± 0.05	1.18 ± 0.04	40
	[C2*]	04 32 15.5	+24 28 59.5	1.5	40.9	5719	> 0.55	> 0.27	> 0.15	> 0.08	13
B18-2	C1	04 32 29.8	+24 50 11.4	1.4	40.0	5605	0.17 ± 0.02	0.16 ± 0.02	0.11 ± 0.02	0.10 ± 0.02	5
	C2	04 32 36.9	+24 52 05.1	11.1	112.9	15804	1.96 ± 0.05	1.81 ± 0.04	1.14 ± 0.09	1.05 ± 0.08	10
TMC-2	C1	04 32 45.9	+24 24 08.0	46.4	230.6	32291	17.48 ± 0.08	16.11 ± 0.07	8.44 ± 0.20	7.77 ± 0.19	43
B18-4	C1*	04 35 36.7	+24 09 05.0	24.1	166.1	23260	12.54 ± 0.11	7.05 ± 0.34	4.03 ± 0.17	2.27 ± 0.11	42
B18-5	C1	04 35 50.4	+24 09 20.6	11.1	112.6	15768	2.92 ± 0.04	2.69 ± 0.04	1.63 ± 0.06	1.51 ± 0.05	22
TMC-1C	C1	04 41 21.5	+26 02 55.2	14.3	128.0	17921	4.19 ± 0.05	3.86 ± 0.04	2.38 ± 0.08	2.19 ± 0.08	22
	C2	04 41 31.7	+26 04 06.5	16.9	139.4	19511	6.33 ± 0.06	5.84 ± 0.05	3.06 ± 0.25	2.82 ± 0.23	28
	C3	04 41 35.9	+26 00 54.1	26.7	175.0	24505	11.63 ± 0.07	10.71 ± 0.07	7.00 ± 0.30	6.45 ± 0.27	28
TMC-1	C1	04 40 59.6	+25 53 46.7	5.9	82.0	11479	1.64 ± 0.05	1.51 ± 0.05	0.95 ± 0.10	0.88 ± 0.09	10
	C2*	04 41 13.3	+25 46 31.7	14.5	128.9	18046	5.05 ± 0.09	2.80 ± 0.05	0.51 ± 0.08	0.28 ± 0.04	25
	C3	04 41 16.0	+25 49 11.6	32.7	193.5	27092	13.82 ± 0.11	12.73 ± 0.10	7.77 ± 0.62	7.16 ± 0.57	21
	C4	04 41 34.9	+25 44 20.7	17.2	140.2	19634	6.40 ± 0.09	5.90 ± 0.09	3.85 ± 0.19	3.55 ± 0.17	13
	C5	04 41 42.3	+25 41 17.4	13.3	123.6	17302	5.72 ± 0.10	5.27 ± 0.09	3.83 ± 0.23	3.53 ± 0.21	12
	C6	04 41 52.6	+25 38 00.2	19.6	149.8	20976	5.81 ± 0.09	5.35 ± 0.09	3.26 ± 0.22	3.00 ± 0.21	12
L1507A	C1	04 42 39.3	+29 43 56.6	16.0	135.2	18933	3.86 ± 0.07	3.55 ± 0.06	2.24 ± 0.16	2.07 ± 0.15	12
	C2	04 42 39.6	+29 41 06.2	14.3	128.0	17916	2.83 ± 0.06	2.60 ± 0.06	1.28 ± 0.13	1.18 ± 0.12	11
	C3	04 43 03.1	+29 43 35.4	8.7	99.6	13944	1.75 ± 0.06	1.61 ± 0.05	0.88 ± 0.14	0.81 ± 0.13	8
L1582A	C1	05 31 55.3	+12 32 24.2	5.1	76.7	30683	1.16 ± 0.04	8.71 ± 0.30	0.74 ± 0.06	5.59 ± 0.46	11
	C2*	05 32 03.1	+12 30 43.2	15.1	131.4	52554	3.97 ± 0.05	29.86 ± 0.40	1.48 ± 0.12	11.16 ± 0.91	22
IRAS05413	C1	05 43 32.7	-01 07 27.6	4.0	67.3	30278	0.76 ± 0.05	7.23 ± 0.49	0.39 ± 0.05	3.72 ± 0.49	6
	C2*	05 43 46.4	-01 04 49.4	17.2	140.2	63097	4.08 ± 0.07	18.24 ± 6.32	0.27 ± 0.04	1.20 ± 0.42	32
	C3*	05 43 51.6	-01 02 51.2	10.6	110.4	49690	3.11 ± 0.04	7.92 ± 0.11	0.39 ± 0.01	0.99 ± 0.02	94
	C4	05 44 00.1	-01 05 00.3	3.5	63.7	28656	0.59 ± 0.03	5.64 ± 0.28	0.43 ± 0.04	4.09 ± 0.42	8
L1622A	[C1]	05 54 21.3	+01 50 34.0	1.8	45.4	20418	0.52 ± 0.04	4.90 ± 0.36	0.37 ± 0.06	3.51 ± 0.55	6

Table 3. continued.

Core	α J2000.0	δ J2000.0	A arcmin ²	r_{eff} arcsec	F_{tot} AU	F_{tot} Jy	M_{tot} M_{\odot}	$F_{50\%}$ Jy	$M_{50\%}$ M_{\odot}	$S_{\text{max}}^{\text{beam}}$	
	[C2*]	05 54 29.8	+01 47 29.5	2.0	48.2	21694	0.78 ± 0.07	7.46 ± 0.63	0.07 ± 0.00	0.62 ± 0.05	6
	C3	05 54 42.6	+01 54 31.4	21.3	156.0	70222	5.49 ± 0.06	52.27 ± 0.59	1.43 ± 0.14	13.62 ± 1.29	28
	C4	05 54 52.6	+01 57 49.3	15.1	131.3	59097	3.05 ± 0.05	29.00 ± 0.46	1.19 ± 0.11	11.32 ± 1.00	17
	C5	05 55 02.9	+02 00 24.6	4.7	73.2	32926	0.77 ± 0.03	7.30 ± 0.30	0.43 ± 0.05	4.09 ± 0.49	8
L183	C1	15 54 00.5	-02 52 28.6	8.1	96.3	10597	2.09 ± 0.05	1.19 ± 0.03	0.85 ± 0.11	0.48 ± 0.06	16
	C2	15 54 08.6	-02 52 03.3	17.0	139.7	15362	6.75 ± 0.06	3.84 ± 0.03	1.92 ± 0.17	1.09 ± 0.10	38
	C3	15 54 09.1	-02 49 17.8	19.0	147.7	16252	6.89 ± 0.08	3.92 ± 0.05	3.43 ± 0.22	1.95 ± 0.12	18
	[C4]	15 54 12.2	-02 58 22.1	13.1	122.3	13458	3.04 ± 0.07	1.73 ± 0.04	1.77 ± 0.26	1.00 ± 0.15	8
	C5	15 54 13.5	-02 55 25.5	6.1	83.6	9195	1.27 ± 0.04	0.72 ± 0.02	0.75 ± 0.10	0.43 ± 0.06	10
	[C6]	15 54 25.2	-02 54 28.4	4.5	72.0	7922	0.70 ± 0.04	0.40 ± 0.02	0.42 ± 0.06	0.24 ± 0.03	6
L438	C1	18 14 04.7	-07 08 22.8	15.6	133.9	36145	2.21 ± 0.05	7.56 ± 0.17	1.32 ± 0.12	4.53 ± 0.41	9
L492	C1	18 15 48.1	-03 45 11.6	22.6	161.1	43494	5.36 ± 0.05	18.35 ± 0.17	2.13 ± 0.10	7.31 ± 0.35	34
CB188	C1*	19 20 15.1	+11 35 50.3	8.7	99.9	29956	1.33 ± 0.03	2.63 ± 0.07	0.20 ± 0.02	0.39 ± 0.01	40
L673-7	C1*	19 21 35.5	+11 21 19.7	14.0	126.8	38029	2.31 ± 0.05	8.38 ± 0.21	0.20 ± 0.05	0.72 ± 0.02	17
	[C2]	19 21 44.0	+11 17 58.1	8.7	100.0	29991	1.09 ± 0.05	4.62 ± 0.20	0.46 ± 0.09	1.96 ± 0.38	7
	[C3]	19 21 53.7	+11 20 05.9	2.7	55.4	16629	0.30 ± 0.02	1.25 ± 0.11	0.15 ± 0.03	0.63 ± 0.14	7
L675	C1	19 23 53.0	+11 07 43.0	1.5	42.1	12622	0.12 ± 0.01	0.51 ± 0.05	0.10 ± 0.02	0.42 ± 0.08	5
L1100	C1*	20 36 19.6	+63 53 12.6	18.3	144.6	57849	3.53 ± 0.06	13.03 ± 0.95	0.31 ± 0.04	1.13 ± 0.08	32
L1041-2	[C1]	20 37 02.3	+57 41 21.7	1.7	44.1	17644	0.26 ± 0.02	1.93 ± 0.15	0.16 ± 0.02	1.17 ± 0.15	6
	[C2]	20 37 08.3	+57 39 27.6	6.9	88.7	35491	1.12 ± 0.04	8.44 ± 0.30	0.54 ± 0.07	4.07 ± 0.52	8
	C3	20 37 13.5	+57 47 50.5	8.5	98.9	39564	2.42 ± 0.05	18.23 ± 0.35	1.15 ± 0.09	8.67 ± 0.71	17
	C4*	20 37 21.0	+57 44 08.3	22.1	159.0	63612	8.27 ± 0.07	22.59 ± 0.96	0.95 ± 0.02	2.60 ± 0.11	72
	[C5]	20 37 22.0	+57 50 32.1	4.6	72.8	29118	1.19 ± 0.05	8.91 ± 0.36	0.79 ± 0.10	5.91 ± 0.75	9
L1148	C1*	20 40 48.0	+67 22 07.6	7.2	90.6	29430	0.77 ± 0.03	3.12 ± 0.13	0.34 ± 0.06	1.36 ± 0.25	7
	C2	20 41 08.7	+67 20 01.4	12.9	121.6	39514	1.74 ± 0.04	8.65 ± 0.21	0.87 ± 0.08	4.32 ± 0.42	10
L1155E	[C1]	20 43 54.7	+67 37 31.5	4.8	74.3	24132	0.77 ± 0.04	3.82 ± 0.18	0.40 ± 0.07	1.97 ± 0.34	7
	[C2]	20 44 01.9	+67 39 49.6	3.9	66.5	21602	0.51 ± 0.03	2.55 ± 0.15	0.40 ± 0.05	1.96 ± 0.26	5
	[C3]	20 44 09.4	+67 41 38.0	0.8	30.5	9901	0.10 ± 0.01	0.51 ± 0.07	0.05 ± 0.01	0.23 ± 0.07	6
L1082C-2	[C1]	20 49 55.0	+60 15 49.7	26.0	172.7	69072	6.43 ± 0.11	48.35 ± 0.80	1.98 ± 0.34	14.90 ± 2.58	13
L1082C	C1*	20 51 28.3	+60 18 34.7	10.0	107.2	42893	2.34 ± 0.06	10.29 ± 1.82	0.41 ± 0.03	1.81 ± 0.32	21
L1082A	C1*	20 53 13.7	+60 14 45.0	4.4	71.0	28402	0.99 ± 0.03	3.69 ± 0.44	0.24 ± 0.02	0.89 ± 0.11	26
	C2	20 53 27.9	+60 14 33.8	10.2	108.3	43328	2.47 ± 0.04	18.56 ± 0.29	0.28 ± 0.00	2.09 ± 0.04	63
	C3*	20 53 50.4	+60 09 45.1	16.7	138.2	55279	3.14 ± 0.05	12.81 ± 0.72	0.18 ± 0.01	0.75 ± 0.04	29
	C4	20 53 51.9	+60 17 17.9	8.2	97.0	38808	1.23 ± 0.04	9.24 ± 0.28	0.40 ± 0.04	3.05 ± 0.30	13
L1228	C1*	20 57 13.2	+77 35 44.0	43.3	222.7	44545	13.24 ± 0.10	11.12 ± 0.08	0.56 ± 0.01	0.47 ± 0.01	107
Bern48	C1*	20 59 13.9	+78 23 04.4	15.5	133.4	26689	4.17 ± 0.05	2.06 ± 0.02	0.43 ± 0.01	0.25 ± 0.00	159
L1172A	C1	21 02 20.5	+67 51 08.8	3.8	65.6	18905	0.82 ± 0.05	3.21 ± 0.18	0.51 ± 0.11	2.01 ± 0.41	7
	C2*	21 02 22.8	+67 54 03.1	12.4	119.0	34269	3.04 ± 0.06	7.63 ± 0.32	0.77 ± 0.12	1.93 ± 0.08	21
L1177	C1*	21 17 39.0	+68 17 30.3	11.5	114.8	33063	2.93 ± 0.05	4.76 ± 0.20	0.47 ± 0.01	0.76 ± 0.03	104
L1021	C1	21 21 44.5	+50 57 51.5	8.8	100.5	25114	1.02 ± 0.03	2.98 ± 0.09	0.64 ± 0.08	1.87 ± 0.24	8
L1014	C1*	21 24 07.2	+49 59 05.0	4.7	73.3	18326	0.85 ± 0.03	1.93 ± 0.07	0.29 ± 0.03	0.66 ± 0.06	16
L1103-2	C1	21 42 14.2	+56 43 34.1	8.9	101.0	25254	1.53 ± 0.04	4.48 ± 0.13	0.92 ± 0.10	2.70 ± 0.30	8

Table 3. continued.

Core		α J2000.0	δ J2000.0	A arcmin ²	r_{eff} arcsec		F_{tot} Jy	M_{tot} M_{\odot}	$F_{50\%}$ Jy	$M_{50\%}$ M_{\odot}	$S_{\text{max}}^{\text{beam}}$
L1251A	[C1]	22 28 53.5	+75 14 56.6	7.2	90.9	27270	1.66 ± 0.06	7.03 ± 0.26	0.77 ± 0.20	3.27 ± 0.86	8
	C2*	22 29 42.7	+75 13 32.2	18.0	143.7	43099	4.85 ± 0.06	14.16 ± 2.10	0.96 ± 0.10	2.80 ± 0.41	30
	C3*	22 30 32.1	+75 14 07.9	13.0	122.2	36667	3.62 ± 0.05	11.09 ± 0.44	0.36 ± 0.01	1.11 ± 0.04	52
	C4*	22 31 11.7	+75 13 06.8	19.0	147.7	44319	4.96 ± 0.07	16.46 ± 0.68	0.98 ± 0.10	3.26 ± 0.13	34
L1197	C1	22 37 02.9	+58 57 20.8	20.8	154.4	46325	2.58 ± 0.05	10.93 ± 0.20	0.38 ± 0.11	1.60 ± 0.46	17

Table 4. Geometry data for subcores. See Table 3 for an explanation of the subcore designations. For every subcore the table lists the major and minor axis at the 50% peak intensity level and their ratio, the position angle of the major axis (east of north), the filling factor for an ellipse defined by the aforementioned axis lengths and orientations, and the effective radius at the 70% peak intensity level.

Core		arcsec	<i>a</i> AU	arcsec	<i>b</i> AU	<i>a/b</i>	P.A. deg	<i>f</i>	arcsec	<i>r</i> _{70%} AU
L1355	[C1]	30 ± 2	5942 ± 345	23 ± 3	4615 ± 648	1.3 ± 0.2	63 ± 29	0.98 ± 0.05	11.0 ± 1.7	2198 ± 334
	[C2]	157 ± 12	31456 ± 2449	121 ± 10	24211 ± 2087	1.3 ± 0.1	138 ± 25	0.67 ± 0.09	32.0 ± 6.2	6392 ± 1244
	[C3]	267 ± 11	53495 ± 2184	163 ± 14	32665 ± 2839	1.6 ± 0.2	14 ± 6	0.57 ± 0.05	35.8 ± 7.3	7152 ± 1460
	[C4]	140 ± 12	28097 ± 2456	111 ± 12	22116 ± 2373	1.3 ± 0.2	6 ± 16	0.64 ± 0.11	24.5 ± 5.9	4900 ± 1188
L1521B-2	C1	304 ± 21	42574 ± 3007	148 ± 15	20669 ± 2040	2.1 ± 0.3	131 ± 4	0.47 ± 0.06	36.5 ± 7.9	5112 ± 1101
	C2	151 ± 11	21160 ± 1496	105 ± 9	14649 ± 1324	1.4 ± 0.1	124 ± 10	0.79 ± 0.06	34.1 ± 5.3	4772 ± 745
	[C3]	61 ± 10	8493 ± 1463	34 ± 6	4769 ± 884	1.8 ± 0.3	45 ± 14	0.90 ± 0.15	17.1 ± 3.0	2394 ± 424
L1521F	C1*	69 ± 8	9715 ± 1182	51 ± 3	7186 ± 452	1.4 ± 0.1	172 ± 9	0.91 ± 0.04	17.1 ± 1.0	2394 ± 134
L1521-2	C1*	130 ± 10	18267 ± 1417	117 ± 14	16322 ± 2023	1.1 ± 0.2	95 ± 36	0.66 ± 0.08	36.5 ± 5.8	5112 ± 817
	C2	152 ± 13	21276 ± 1868	127 ± 11	17817 ± 1496	1.2 ± 0.1	8 ± 17	0.87 ± 0.05	34.1 ± 8.8	4772 ± 1238
L1524-4	C1	176 ± 11	24656 ± 1522	129 ± 9	18127 ± 1311	1.4 ± 0.1	45 ± 12	0.79 ± 0.04	42.3 ± 6.0	5916 ± 844
	[C2]	139 ± 6	19441 ± 826	123 ± 7	17275 ± 970	1.1 ± 0.1	81 ± 27	0.81 ± 0.08	40.8 ± 5.6	5712 ± 785
	[C3]	154 ± 16	21623 ± 2244	97 ± 7	13585 ± 967	1.6 ± 0.2	157 ± 14	0.64 ± 0.10	28.7 ± 6.1	4015 ± 856
B18-1	C1	109 ± 3	15321 ± 477	60 ± 2	8362 ± 310	1.8 ± 0.1	8 ± 2	0.92 ± 0.01	24.3 ± 1.2	3408 ± 174
	[C2*]	24 ± 1	3412 ± 182	22 ± 1	3016 ± 162	1.1 ± 0.1	180 ± 36	1.00 ± 0.02	8.4 ± 0.5	1172 ± 66
B18-2	C1	87 ± 14	12197 ± 1978	39 ± 6	5512 ± 842	2.2 ± 0.4	61 ± 14	0.82 ± 0.15	18.1 ± 4.2	2533 ± 587
	C2	243 ± 13	34010 ± 1806	96 ± 10	13484 ± 1333	2.5 ± 0.2	124 ± 3	0.79 ± 0.04	42.5 ± 6.5	5954 ± 917
TMC-2	C1	309 ± 3	43306 ± 404	155 ± 4	21764 ± 495	2.0 ± 0.0	10 ± 0	0.84 ± 0.01	75.6 ± 2.5	10581 ± 357
B18-4	C1*	147 ± 5	20536 ± 635	102 ± 5	14268 ± 694	1.4 ± 0.1	37 ± 3	0.91 ± 0.02	31.7 ± 1.4	4431 ± 193
B18-5	C1	152 ± 3	21256 ± 408	101 ± 4	14074 ± 552	1.5 ± 0.1	180 ± 4	0.92 ± 0.02	44.8 ± 2.9	6267 ± 402
TMC-1C	C1	174 ± 3	24379 ± 455	122 ± 5	17116 ± 739	1.4 ± 0.1	148 ± 4	0.90 ± 0.02	50.6 ± 3.1	7080 ± 437
	C2	211 ± 20	29494 ± 2771	112 ± 5	15654 ± 751	1.9 ± 0.2	158 ± 2	0.80 ± 0.03	43.6 ± 3.2	6107 ± 445
	C3	335 ± 10	46903 ± 1398	144 ± 5	20221 ± 692	2.3 ± 0.1	143 ± 1	0.80 ± 0.01	64.1 ± 3.6	8970 ± 510
TMC-1	C1	134 ± 12	18765 ± 1696	92 ± 14	12926 ± 1895	1.5 ± 0.2	158 ± 18	0.76 ± 0.08	34.8 ± 3.6	4875 ± 497
	C2*	58 ± 7	8144 ± 994	44 ± 7	6120 ± 920	1.3 ± 0.2	94 ± 26	0.91 ± 0.06	13.4 ± 0.9	1874 ± 132
	C3	475 ± 19	66492 ± 2686	134 ± 10	18734 ± 1398	3.5 ± 0.2	133 ± 1	0.76 ± 0.02	66.4 ± 6.7	9297 ± 933
	C4	284 ± 4	39699 ± 597	120 ± 8	16804 ± 1189	2.4 ± 0.2	149 ± 3	0.82 ± 0.04	55.9 ± 6.9	7829 ± 960
	C5	244 ± 9	34105 ± 1246	127 ± 8	17728 ± 1135	1.9 ± 0.1	135 ± 3	0.87 ± 0.04	57.1 ± 6.5	7988 ± 906
	C6	270 ± 11	37819 ± 1529	126 ± 14	17662 ± 1903	2.1 ± 0.2	147 ± 2	0.85 ± 0.04	63.9 ± 7.0	8949 ± 976
L1507A	C1	221 ± 12	30936 ± 1673	134 ± 9	18783 ± 1206	1.6 ± 0.1	153 ± 5	0.81 ± 0.03	52.5 ± 6.1	7355 ± 860
	C2	160 ± 11	22420 ± 1546	145 ± 16	20248 ± 2292	1.1 ± 0.1	166 ± 33	0.71 ± 0.06	39.8 ± 6.2	5577 ± 870
	C3	158 ± 19	22079 ± 2600	106 ± 21	14891 ± 2934	1.5 ± 0.2	55 ± 25	0.69 ± 0.08	27.9 ± 6.5	3909 ± 910
L1582A	C1	139 ± 10	55663 ± 4019	84 ± 8	33637 ± 3004	1.7 ± 0.2	144 ± 6	0.76 ± 0.04	34.7 ± 4.9	13884 ± 1944
	C2*	170 ± 7	67871 ± 2955	85 ± 8	33838 ± 3109	2.0 ± 0.1	73 ± 4	0.81 ± 0.03	26.4 ± 3.6	10567 ± 1436
IRAS05413	C1	162 ± 13	73042 ± 5997	95 ± 13	42641 ± 5769	1.7 ± 0.3	114 ± 9	0.41 ± 0.06	18.5 ± 5.7	8335 ± 2554
	C2*	67 ± 19	30110 ± 8667	36 ± 2	16175 ± 1008	1.9 ± 0.5	13 ± 10	0.66 ± 0.15	11.7 ± 0.4	5257 ± 201
	C3*	28 ± 0	12508 ± 111	26 ± 1	11595 ± 340	1.1 ± 0.0	119 ± 16	0.98 ± 0.01	9.3 ± 0.1	4167 ± 65
	C4	119 ± 8	53594 ± 3544	103 ± 9	46547 ± 4063	1.2 ± 0.1	170 ± 29	0.67 ± 0.08	30.8 ± 4.2	13851 ± 1906
L1622A	[C1]	82 ± 7	37112 ± 3014	73 ± 9	32685 ± 3930	1.1 ± 0.2	121 ± 32	0.71 ± 0.13	20.1 ± 4.0	9061 ± 1795
	[C2*]	18 ± 4	8323 ± 1921	7 ± 1	3179 ± 255	2.6 ± 0.8	122 ± 7	1.00 ± 0.07	3.9 ± 0.2	1777 ± 73

Table 4. continued.

Core		arcsec	a AU	arcsec	b AU	a/b	P.A. deg	f	arcsec	$r_{70\%}$ AU
	C3	269 ± 15	121133 ± 6542	40 ± 3	18114 ± 1269	6.7 ± 0.3	53 ± 1	0.87 ± 0.02	21.9 ± 2.7	9855 ± 1226
	C4	177 ± 9	79819 ± 3968	97 ± 11	43660 ± 4851	1.8 ± 0.2	17 ± 7	0.74 ± 0.05	29.7 ± 4.1	13358 ± 1858
	C5	158 ± 18	71105 ± 8116	65 ± 8	29159 ± 3721	2.4 ± 0.3	66 ± 4	0.71 ± 0.07	29.8 ± 3.7	13388 ± 1663
L183	C1	112 ± 12	12294 ± 1318	84 ± 10	9187 ± 1082	1.3 ± 0.2	177 ± 24	0.82 ± 0.04	25.7 ± 3.7	2832 ± 402
	C2	151 ± 8	16650 ± 922	60 ± 4	6603 ± 419	2.5 ± 0.2	180 ± 1	0.92 ± 0.05	22.8 ± 1.4	2505 ± 156
	C3	177 ± 9	19468 ± 968	143 ± 9	15775 ± 1040	1.2 ± 0.1	50 ± 12	0.87 ± 0.03	51.5 ± 4.2	5664 ± 457
	[C4]	238 ± 14	26193 ± 1507	177 ± 16	19499 ± 1781	1.3 ± 0.1	11 ± 10	0.54 ± 0.07	38.5 ± 7.4	4239 ± 814
	C5	140 ± 8	15415 ± 842	90 ± 11	9932 ± 1232	1.6 ± 0.2	144 ± 15	0.85 ± 0.08	31.8 ± 6.8	3502 ± 751
	[C6]	205 ± 21	22556 ± 2257	85 ± 13	9362 ± 1425	2.4 ± 0.5	167 ± 5	0.49 ± 0.09	25.2 ± 5.3	2773 ± 587
L438	C1	221 ± 9	59549 ± 2518	188 ± 15	50816 ± 3999	1.2 ± 0.1	5 ± 27	0.69 ± 0.06	51.9 ± 7.1	14025 ± 1913
L492	C1	198 ± 11	53555 ± 2989	94 ± 3	25379 ± 768	2.1 ± 0.1	179 ± 2	0.89 ± 0.02	41.5 ± 2.3	11196 ± 617
CB188	C1*	51 ± 5	15441 ± 1538	28 ± 1	8456 ± 230	1.8 ± 0.2	16 ± 4	0.88 ± 0.03	11.0 ± 0.4	3298 ± 118
L673-7	C1*	56 ± 64	16829 ± 19090	36 ± 10	10784 ± 3141	1.6 ± 1.3	90 ± 20	0.88 ± 0.26	12.0 ± 1.7	3603 ± 513
	[C2]	188 ± 13	56491 ± 3799	166 ± 15	49780 ± 4447	1.1 ± 0.1	50 ± 37	0.33 ± 0.06	22.7 ± 5.1	6806 ± 1523
	[C3]	110 ± 18	32885 ± 5393	52 ± 13	15454 ± 3833	2.1 ± 0.4	56 ± 10	0.55 ± 0.11	17.7 ± 3.9	5298 ± 1176
L675	C1	131 ± 13	39235 ± 3995	60 ± 6	18001 ± 1862	2.2 ± 0.5	125 ± 5	0.62 ± 0.16	24.8 ± 5.2	7446 ± 1574
L1100	C1*	64 ± 11	25760 ± 4219	34 ± 2	13414 ± 691	1.9 ± 0.3	31 ± 6	0.71 ± 0.06	11.5 ± 0.4	4605 ± 161
L1041-2	[C1]	88 ± 8	35159 ± 3105	51 ± 8	20267 ± 3224	1.7 ± 0.3	8 ± 14	0.72 ± 0.09	17.8 ± 3.0	7108 ± 1188
	[C2]	166 ± 13	66259 ± 5241	134 ± 12	53597 ± 4731	1.2 ± 0.2	166 ± 14	0.40 ± 0.05	25.8 ± 2.9	10328 ± 1142
	C3	164 ± 5	65597 ± 1909	69 ± 10	27482 ± 3914	2.4 ± 0.3	177 ± 5	0.78 ± 0.07	27.9 ± 3.9	11170 ± 1571
	C4*	49 ± 1	19422 ± 357	41 ± 1	16585 ± 404	1.2 ± 0.0	57 ± 3	0.98 ± 0.01	14.2 ± 0.4	5695 ± 143
	[C5]	188 ± 16	75020 ± 6205	69 ± 9	27555 ± 3420	2.7 ± 0.4	175 ± 3	0.72 ± 0.06	32.9 ± 6.1	13169 ± 2426
L1148	C1*	334 ± 22	108709 ± 7032	71 ± 12	23023 ± 3946	4.7 ± 0.7	45 ± 3	0.39 ± 0.06	15.2 ± 6.2	4929 ± 2014
	C2	291 ± 28	94458 ± 9118	82 ± 11	26700 ± 3636	3.5 ± 0.4	50 ± 2	0.70 ± 0.06	38.0 ± 4.8	12344 ± 1567
L1155E	[C1]	158 ± 14	51375 ± 4431	97 ± 12	31363 ± 3793	1.6 ± 0.3	47 ± 9	0.45 ± 0.08	21.5 ± 4.7	6971 ± 1543
	[C2]	172 ± 20	55813 ± 6491	86 ± 7	27996 ± 2341	2.0 ± 0.3	80 ± 5	0.67 ± 0.08	33.5 ± 5.8	10891 ± 1885
	[C3]	80 ± 10	26095 ± 3322	38 ± 8	12208 ± 2521	2.1 ± 0.4	33 ± 23	0.33 ± 0.18	8.4 ± 3.4	2722 ± 1121
L1082C-2	[C1]	238 ± 25	95163 ± 10142	120 ± 13	48085 ± 5214	2.0 ± 0.1	84 ± 7	0.59 ± 0.05	36.0 ± 6.3	14413 ± 2539
L1082C	C1*	58 ± 5	23283 ± 2070	42 ± 4	16778 ± 1445	1.4 ± 0.1	167 ± 11	0.95 ± 0.05	16.0 ± 0.9	6416 ± 365
L1082A	C1*	48 ± 5	19277 ± 2178	30 ± 1	12141 ± 580	1.6 ± 0.2	122 ± 4	0.98 ± 0.03	11.7 ± 0.4	4672 ± 149
	C2	30 ± 1	12066 ± 300	25 ± 1	10070 ± 204	1.2 ± 0.0	32 ± 6	0.99 ± 0.01	9.7 ± 0.3	3869 ± 111
	C3*	33 ± 3	13355 ± 1010	28 ± 1	11360 ± 394	1.2 ± 0.1	37 ± 10	1.00 ± 0.02	9.7 ± 0.4	3869 ± 166
	C4	182 ± 15	72704 ± 5831	32 ± 12	12831 ± 4800	5.7 ± 1.1	46 ± 4	0.85 ± 0.15	21.6 ± 3.7	8652 ± 1494
L1228	C1*	32 ± 1	6350 ± 172	27 ± 1	5497 ± 113	1.2 ± 0.0	13 ± 7	1.00 ± 0.01	10.1 ± 0.0	2013 ± 0
Bern48	C1*	25 ± 0	4961 ± 32	23 ± 1	4500 ± 124	1.1 ± 0.0	180 ± 25	1.00 ± 0.01	8.4 ± 0.1	1675 ± 19
L1172A	C1	107 ± 10	30875 ± 2995	100 ± 11	28762 ± 3307	1.1 ± 0.2	119 ± 48	0.70 ± 0.13	21.3 ± 6.2	6125 ± 1785
	C2*	90 ± 9	25969 ± 2644	74 ± 9	21361 ± 2473	1.2 ± 0.1	70 ± 49	0.82 ± 0.07	21.8 ± 2.1	6281 ± 608
L1177	C1*	28 ± 0	8142 ± 122	26 ± 0	7457 ± 103	1.1 ± 0.0	105 ± 5	0.96 ± 0.02	9.7 ± 0.2	2786 ± 70
L1021	C1	216 ± 12	54043 ± 3097	115 ± 12	28869 ± 2922	1.9 ± 0.2	42 ± 6	0.69 ± 0.07	35.6 ± 5.8	8899 ± 1443
L1014	C1*	62 ± 10	15519 ± 2484	49 ± 3	12255 ± 851	1.3 ± 0.2	160 ± 18	0.92 ± 0.07	18.2 ± 1.5	4551 ± 378
L1103-2	C1	273 ± 7	68328 ± 1785	81 ± 8	20275 ± 2006	3.4 ± 0.4	56 ± 2	0.69 ± 0.08	36.0 ± 5.0	8995 ± 1255
L1251A	[C1]	173 ± 15	51784 ± 4605	98 ± 24	29293 ± 7108	1.8 ± 0.5	103 ± 11	0.54 ± 0.12	26.7 ± 7.2	8013 ± 2149
	C2*	147 ± 10	44246 ± 3114	56 ± 2	16868 ± 703	2.6 ± 0.2	81 ± 3	0.59 ± 0.08	19.7 ± 1.1	5923 ± 332

Table 4. continued.

Core	arcsec	a AU	arcsec	b AU	a/b	P.A. deg	f	arcsec	$r_{70\%}$ AU	
	C3*	37 ± 1	10998 ± 292	35 ± 1	10459 ± 312	1.1 ± 0.0	71 ± 21	1.00 ± 0.01	11.8 ± 0.2	3554 ± 69
	C4*	158 ± 12	47291 ± 3503	41 ± 3	12350 ± 759	3.8 ± 0.3	135 ± 3	0.80 ± 0.05	18.1 ± 1.3	5429 ± 376
L1197	C1	200 ± 72	59945 ± 21604	59 ± 11	17669 ± 3436	3.4 ± 0.6	127 ± 4	0.48 ± 0.06	25.0 ± 2.9	7493 ± 861

Table 5. Data on dust emission peaks. Bracketed and starred peak designations indicate peaks with uncertain properties due to artifacts and peaks with associated YSOs or VeLLOs, respectively. For every peak the table lists the peak position, the associated subcore, if applicable, the peak flux density per 11'' beam (after smoothing to 20'' resolution) and the related column density and extinction, the flux density and radius for an aperture of 4 200 AU radius, and the flux densities for the c2d standard apertures between 20'' and 120'' diameter.

Core		α J2000.0	δ J2000.0	Asso.	F_{\max}^{beam} mJy beam $^{-1}$	$N(\text{H}_2)$ 10^{22} cm $^{-2}$	A_V mag	$F_{4200\text{AU}}$ mJy	$M_{4200\text{AU}}$ M_{\odot}	$F_{20''}$ mJy	$F_{40''}$ mJy	$F_{80''}$ mJy	$F_{120''}$ mJy
L1355	[P1]	02 52 41.2	+68 57 01.0	[C1]	11 ± 2	0.72 ± 0.16	7.6 ± 1.7	83 ± 14	0.16 ± 0.03	31 ± 7	79 ± 14	198 ± 28	337 ± 44
	[P2]	02 52 58.1	+68 53 17.0	[C2]	13 ± 2	0.87 ± 0.16	9.3 ± 1.7	102 ± 14	0.19 ± 0.03	36 ± 7	91 ± 13	241 ± 27	528 ± 42
	[P3]	02 53 18.9	+68 57 25.5	[C3]	14 ± 2	0.95 ± 0.12	10.1 ± 1.3	115 ± 11	0.22 ± 0.02	40 ± 5	110 ± 10	334 ± 21	695 ± 31
	[P4]	02 53 40.3	+68 53 55.5	[C4]	11 ± 2	0.76 ± 0.16	8.1 ± 1.7	84 ± 15	0.16 ± 0.03	28 ± 7	84 ± 14	246 ± 29	449 ± 45
L1521B-2	P1	04 23 30.8	+26 38 07.0	C1	15 ± 1	1.00 ± 0.09	10.6 ± 0.9	259 ± 11	0.24 ± 0.01	38 ± 4	120 ± 8	438 ± 16	832 ± 23
	P2	04 23 37.1	+26 40 23.5	[C3]	9 ± 1	0.62 ± 0.07	6.6 ± 0.8	153 ± 10	0.14 ± 0.01	24 ± 3	73 ± 6	256 ± 13	473 ± 19
	[P3]	04 23 42.3	+26 41 26.5	[C3]	6 ± 1	0.43 ± 0.09	4.6 ± 1.0	78 ± 12	0.07 ± 0.01	17 ± 4	46 ± 8	113 ± 16	249 ± 25
L1521F	P1*	04 28 39.4	+26 51 34.0	C1*	66 ± 2			972 ± 17	0.77 ± 0.01	173 ± 6	537 ± 11	1476 ± 23	2471 ± 34
L1521-2	P1	04 29 26.9	+27 00 53.5	C1*	8 ± 1	0.51 ± 0.10	5.4 ± 1.0	135 ± 12	0.12 ± 0.01	21 ± 4	59 ± 8	216 ± 17	416 ± 25
	P2	04 29 37.4	+26 58 05.5	C2	19 ± 1	1.26 ± 0.09	13.4 ± 0.9	331 ± 11	0.30 ± 0.01	50 ± 4	161 ± 7	556 ± 15	1124 ± 22
L1524-4	P1	04 30 07.5	+24 25 48.0	C1	19 ± 1	1.30 ± 0.09	13.9 ± 1.0	343 ± 12	0.32 ± 0.01	50 ± 4	164 ± 8	605 ± 16	1190 ± 25
	[P2]	04 30 15.9	+24 24 20.5	[C2]	11 ± 2	0.76 ± 0.10	8.1 ± 1.1	204 ± 13	0.19 ± 0.01	30 ± 4	98 ± 9	324 ± 18	634 ± 27
	[P3]	04 30 22.3	+24 27 26.0	[C3]	10 ± 2	0.70 ± 0.16	7.4 ± 1.7	115 ± 21	0.11 ± 0.02	31 ± 7	61 ± 14	206 ± 29	468 ± 45
B18-1	P1	04 31 45.4	+24 32 44.5	C1	13 ± 1	0.89 ± 0.07	9.5 ± 0.8	219 ± 9	0.20 ± 0.01	37 ± 3	104 ± 6	349 ± 12	704 ± 19
	P2	04 31 47.4	+24 31 55.5	C1	15 ± 1	1.01 ± 0.07	10.7 ± 0.8	274 ± 9	0.25 ± 0.01	41 ± 3	128 ± 6	446 ± 13	945 ± 19
	P3	04 31 55.6	+24 32 55.0	C1	49 ± 1	3.30 ± 0.08	35.1 ± 0.8	808 ± 10	0.74 ± 0.01	124 ± 3	421 ± 7	1200 ± 13	1992 ± 20
	P4	04 32 08.9	+24 30 21.0		9 ± 2	0.59 ± 0.12	6.3 ± 1.3	61 ± 16	0.06 ± 0.01	23 ± 5	53 ± 10	90 ± 21	210 ± 32
	[P5*]	04 32 15.4	+24 29 00.5	[C2*]	> 65 ± 5			> 360 ± 50	> 0.18 ± 0.02	> 204 ± 14	> 293 ± 30	> 480 ± 85	> 584 ± 473
B18-2	P1	04 32 30.0	+24 50 17.0	C1	9 ± 2	0.58 ± 0.11	6.2 ± 1.2	116 ± 15	0.11 ± 0.01	26 ± 5	56 ± 10	172 ± 20	334 ± 30
	P2	04 32 41.3	+24 51 30.5	C2	14 ± 1	0.91 ± 0.09	9.7 ± 1.0	223 ± 12	0.21 ± 0.01	35 ± 4	112 ± 8	369 ± 16	641 ± 24
TMC-2	P1	04 32 43.8	+24 23 14.5	C1	45 ± 1	2.98 ± 0.07	31.7 ± 0.7	835 ± 9	0.77 ± 0.01	111 ± 3	402 ± 6	1388 ± 11	2694 ± 17
B18-4	P1*	04 35 35.2	+24 08 17.5	C1*	71 ± 2			974 ± 19	0.55 ± 0.03	195 ± 6	524 ± 13	1557 ± 27	3126 ± 41
	P2	04 35 37.7	+24 09 17.0	C1*	71 ± 2	4.75 ± 0.11	50.5 ± 1.2	1282 ± 14	1.18 ± 0.01	172 ± 5	643 ± 9	2068 ± 19	3841 ± 29
B18-5	P1	04 35 51.0	+24 09 27.5	C1	25 ± 1	1.68 ± 0.08	17.9 ± 0.8	462 ± 10	0.43 ± 0.01	64 ± 3	217 ± 6	809 ± 13	1566 ± 19
TMC-1C	P1	04 41 21.8	+26 02 32.5	C1	27 ± 1	1.78 ± 0.08	18.9 ± 0.9	525 ± 10	0.48 ± 0.01	63 ± 3	245 ± 7	885 ± 14	1740 ± 21
	P2	04 41 32.2	+26 03 42.5	C2	36 ± 1	2.42 ± 0.09	25.8 ± 0.9	705 ± 11	0.65 ± 0.01	89 ± 4	328 ± 7	1197 ± 15	2306 ± 22
	P3*	04 41 38.7	+25 56 25.0		12 ± 2			71 ± 17	0.04 ± 0.00	38 ± 5	58 ± 11	58 ± 23	76 ± 35
	P4	04 41 39.2	+26 00 12.5	C3	39 ± 1	2.63 ± 0.09	28.0 ± 1.0	794 ± 12	0.73 ± 0.01	97 ± 4	356 ± 8	1350 ± 16	2659 ± 24
TMC-1	P1	04 40 59.5	+25 53 54.5	C1	21 ± 2	1.40 ± 0.15	14.9 ± 1.6	406 ± 19	0.37 ± 0.02	55 ± 6	174 ± 12	613 ± 25	1164 ± 38
	P2*	04 41 12.8	+25 46 33.5	C2*	52 ± 2			684 ± 18	0.38 ± 0.01	143 ± 6	366 ± 12	1053 ± 25	1900 ± 37
	P3	04 41 13.8	+25 49 49.5	C3	36 ± 2	2.39 ± 0.11	25.4 ± 1.2	668 ± 15	0.62 ± 0.01	91 ± 5	307 ± 10	1147 ± 20	2246 ± 29
	P4	04 41 37.2	+25 43 38.5	C4	30 ± 2	2.00 ± 0.16	21.3 ± 1.7	569 ± 20	0.52 ± 0.02	80 ± 7	256 ± 13	999 ± 27	1960 ± 41
	P5	04 41 43.9	+25 41 22.0	C5	31 ± 3	2.08 ± 0.18	22.2 ± 1.9	605 ± 23	0.56 ± 0.02	83 ± 7	277 ± 15	986 ± 30	1997 ± 45
	P6	04 41 51.9	+25 38 09.5	C6	24 ± 2	1.63 ± 0.14	17.3 ± 1.5	460 ± 18	0.42 ± 0.02	65 ± 6	199 ± 12	766 ± 24	1553 ± 36
L1507A	P1	04 42 30.5	+29 39 22.5	C2	10 ± 2	0.69 ± 0.12	7.4 ± 1.3	116 ± 15	0.11 ± 0.01	31 ± 5	66 ± 10	143 ± 21	256 ± 31
	P2	04 42 38.3	+29 43 48.5	C1	20 ± 2	1.35 ± 0.11	14.4 ± 1.1	369 ± 14	0.34 ± 0.01	50 ± 5	168 ± 9	653 ± 19	1335 ± 28
	P3	04 42 38.9	+29 45 54.5	C1	15 ± 2	1.03 ± 0.13	11.0 ± 1.4	173 ± 17	0.16 ± 0.02	43 ± 5	111 ± 11	296 ± 23	576 ± 34
	P4	04 42 41.0	+29 41 07.5	C2	18 ± 2	1.20 ± 0.11	12.8 ± 1.1	308 ± 14	0.28 ± 0.01	48 ± 4	140 ± 9	507 ± 18	1030 ± 27
	P5	04 43 02.0	+29 43 41.5	C3	17 ± 2	1.14 ± 0.13	12.2 ± 1.4	289 ± 17	0.27 ± 0.02	47 ± 6	146 ± 11	470 ± 23	863 ± 34
L1582A	P1	05 31 49.1	+12 32 00.0		14 ± 2	0.92 ± 0.14	9.7 ± 1.5	43 ± 6	0.32 ± 0.05	40 ± 6	61 ± 12	125 ± 25	302 ± 40
	P2	05 31 56.1	+12 32 24.5	C1	17 ± 2	1.16 ± 0.11	12.3 ± 1.1	48 ± 5	0.36 ± 0.03	44 ± 4	141 ± 9	493 ± 18	904 ± 28
	P3	05 32 01.1	+12 30 32.5	C2	30 ± 1	2.01 ± 0.09	21.3 ± 0.9	82 ± 4	0.61 ± 0.03	76 ± 4	260 ± 7	837 ± 15	1477 ± 23
	P4	05 32 05.4	+12 31 14.5	C2	22 ± 1	1.44 ± 0.09	15.3 ± 0.9	58 ± 4	0.44 ± 0.03	54 ± 4	188 ± 7	632 ± 15	1283 ± 23

Table 5. continued.

Core		α J2000.0	δ J2000.0	Asso.	F_{\max}^{beam} mJy beam $^{-1}$	$N(\text{H}_2)$ 10 22 cm $^{-2}$	A_V mag	$F_{4200 \text{ AU}}$ mJy	$M_{4200 \text{ AU}}$ M_{\odot}	$F_{20''}$ mJy	$F_{40''}$ mJy	$F_{80''}$ mJy	$F_{120''}$ mJy
Bern48	P1*	20 59 14.4	+78 23 05.0	C1*	170 \pm 1			877 \pm 6	0.48 \pm 0.00	523 \pm 3	851 \pm 6	1445 \pm 12	2153 \pm 18
	[P2]	20 59 42.3	+78 24 25.5	C1*	6 \pm 1	0.41 \pm 0.07	4.4 \pm 0.8	41 \pm 6	0.08 \pm 0.01	18 \pm 3	40 \pm 6	94 \pm 12	219 \pm 19
L1172A	P1	21 02 16.9	+67 51 01.5	C1	16 \pm 2	1.05 \pm 0.16	11.2 \pm 1.7	73 \pm 10	0.29 \pm 0.04	43 \pm 7	116 \pm 13	375 \pm 28	727 \pm 43
	P2*	21 02 21.8	+67 54 14.0	C2*	32 \pm 2			154 \pm 6	0.39 \pm 0.02	86 \pm 4	237 \pm 9	791 \pm 18	1403 \pm 26
	P3	21 02 41.6	+67 54 10.5	C2*	10 \pm 2	0.68 \pm 0.10	7.2 \pm 1.1	48 \pm 6	0.19 \pm 0.03	29 \pm 4	69 \pm 9	139 \pm 18	251 \pm 27
L1177	[P1]	21 17 14.7	+68 20 15.0		10 \pm 2	0.68 \pm 0.14	7.3 \pm 1.5	50 \pm 9	0.20 \pm 0.04	31 \pm 6	66 \pm 12	89 \pm 25	216 \pm 39
	P2*	21 17 38.8	+68 17 30.5	C1*	146 \pm 1			657 \pm 6	1.07 \pm 0.04	433 \pm 4	837 \pm 8	1377 \pm 16	1796 \pm 24
L1021	P1*	21 21 27.5	+50 59 46.0		11 \pm 2			42 \pm 8	0.02 \pm 0.00	35 \pm 5	39 \pm 9	89 \pm 19	137 \pm 29
	P2	21 21 46.4	+50 57 33.0	C1	8 \pm 1	0.57 \pm 0.07	6.0 \pm 0.7	48 \pm 5	0.14 \pm 0.01	22 \pm 3	64 \pm 6	219 \pm 12	385 \pm 17
L1014	P1*	21 24 07.4	+49 59 06.0	C1*	23 \pm 1			141 \pm 6	0.32 \pm 0.01	59 \pm 4	199 \pm 8	487 \pm 16	623 \pm 23
L1103-2	P1	21 42 15.9	+56 43 45.5	C1	14 \pm 1	0.91 \pm 0.10	9.7 \pm 1.0	86 \pm 7	0.25 \pm 0.02	34 \pm 4	111 \pm 8	321 \pm 17	593 \pm 25
L1251A	[P1]	22 28 51.4	+75 15 09.0	[C1]	17 \pm 2	1.17 \pm 0.16	12.4 \pm 1.7	78 \pm 9	0.33 \pm 0.04	49 \pm 7	131 \pm 13	470 \pm 28	846 \pm 43
	P2	22 29 44.6	+75 13 24.0	C2*	43 \pm 1	2.88 \pm 0.09	30.6 \pm 1.0	190 \pm 5	0.80 \pm 0.02	110 \pm 4	353 \pm 8	996 \pm 16	1715 \pm 24
	P3*	22 30 00.1	+75 13 55.5	C2*	26 \pm 1			114 \pm 5	0.33 \pm 0.05	66 \pm 4	214 \pm 8	713 \pm 15	1413 \pm 23
	P4*	22 30 32.2	+75 14 09.5	C3*	67 \pm 1			282 \pm 5	0.87 \pm 0.03	185 \pm 3	456 \pm 7	1020 \pm 14	1636 \pm 22
	P5*	22 31 06.0	+75 13 34.5	C4*	45 \pm 1			198 \pm 5	0.66 \pm 0.03	117 \pm 4	359 \pm 7	925 \pm 15	1490 \pm 22
L1197	P1	22 37 02.7	+58 57 31.5	C1	15 \pm 1	1.02 \pm 0.06	10.9 \pm 0.6	68 \pm 3	0.29 \pm 0.01	39 \pm 2	133 \pm 5	386 \pm 10	637 \pm 15

Appendix A: Dust Emission Properties

This appendix summarises formulas to convert the observed flux density of dust emission into column densities and masses. These are evaluated for the standard assumptions for dust properties made by the c2d collaboration. The discussion presented here is intended to serve as a future reference for the c2d project.

A.1. Molecular Weight

As one usually wishes to express column densities in terms of particles per area, the molecular weight needs to be introduced into the equations. The molecular weight per hydrogen molecule, μ_{H_2} , is defined via $\mu_{\text{H}_2} m_{\text{H}} \mathcal{N}(\text{H}_2) = \mathcal{M}$; here \mathcal{M} is the total mass contained in a volume with $\mathcal{N}(\text{H}_2)$ hydrogen molecules, and m_{H} is the H-atom mass. It can be calculated from cosmic abundance ratios. For hydrogen, helium, and metals the mass ratios are $\mathcal{M}(\text{H})/\mathcal{M} \approx 0.71$, $\mathcal{M}(\text{He})/\mathcal{M} \approx 0.27$, and $\mathcal{M}(\text{Z})/\mathcal{M} \approx 0.02$, respectively, where $\mathcal{M} = \mathcal{M}(\text{H}) + \mathcal{M}(\text{He}) + \mathcal{M}(\text{Z})$ (Cox 2000). As $\mathcal{N}(\text{H}) = 2\mathcal{N}(\text{H}_2)$, $\mathcal{M}(\text{H}) = m_{\text{H}}\mathcal{N}(\text{H})$,

$$\mu_{\text{H}_2} = \frac{\mathcal{M}}{m_{\text{H}}\mathcal{N}(\text{H}_2)} = \frac{2\mathcal{M}}{m_{\text{H}}\mathcal{N}(\text{H})} = \frac{2\mathcal{M}}{\mathcal{M}(\text{H})} \approx 2.8. \quad (\text{A.1})$$

Note the difference to the mean molecular weight per free particle, μ_{p} , defined via $\mu_{\text{p}} m_{\text{H}} \mathcal{N} = \mathcal{M}$, where $\mathcal{N} \approx \mathcal{N}(\text{H}_2) + \mathcal{N}(\text{He})$ for gas with all H in molecules. As the helium contribution is dominated by ^4He , and each H_2 molecule has a weight of two hydrogen atoms, $\mathcal{N}(\text{H}_2) = \mathcal{M}(\text{H})/(2m_{\text{H}})$ and $\mathcal{N}(\text{He}) = \mathcal{M}(\text{He})/(4m_{\text{H}})$. Thus

$$\mu_{\text{p}} = \frac{\mathcal{M}}{m_{\text{H}}[\mathcal{N}(\text{H}_2) + \mathcal{N}(\text{He})]} \quad (\text{A.2})$$

$$= \frac{\mathcal{M}}{m_{\text{H}}[\mathcal{M}(\text{H})/(2m_{\text{H}}) + \mathcal{M}(\text{He})/(4m_{\text{H}})]} \quad (\text{A.3})$$

$$= \frac{\mathcal{M}/\mathcal{M}(\text{H})}{[1/2 + \mathcal{M}(\text{He})/(4\mathcal{M}(\text{H}))]} \quad (\text{A.4})$$

$$\approx 2.37; \quad (\text{A.5})$$

the classical value of $\mu_{\text{p}} = 2.33$ holds for an abundance ratio $\mathcal{N}(\text{H})/\mathcal{N}(\text{He}) = 10$ and a negligible admixture of metals.

Both molecular weights are applied in different contexts. The mean molecular weight per free particle, μ_{p} , is e.g. used to evaluate the thermal gas pressure, $P = \rho k_{\text{B}} T / \mu_{\text{p}}$, where T , ρ , and k_{B} are the gas temperature, density, and Boltzmann's constant, respectively. The molecular mass per hydrogen molecule, μ_{H_2} , is needed below to derive particle column densities.

A.2. Radiative Transfer

A.2.1. Equation of Radiative Transfer

The intensity emitted by a medium of temperature T and of optical depth τ_{ν} at the frequency ν is given by the equation of radiative transfer, which reads

$$I_{\nu} = B_{\nu}(T) (1 - e^{-\tau_{\nu}}) \quad (\text{A.6})$$

in the case of local thermal equilibrium. Here B_{ν} is the Planck function. For the optical depth,

$$\tau_{\nu} = \int \kappa_{\nu} \rho \, ds, \quad (\text{A.7})$$

where κ_{ν} is the (specific) absorption coefficient (i.e., per mass) or dust opacity. If most hydrogen is in molecules, the optical depth can be related to the column density of molecular hydrogen,

$$N_{\text{H}_2} = \int n_{\text{H}_2} \, ds = \int \frac{\rho}{\mu_{\text{H}_2} m_{\text{H}}} \, ds = \frac{1}{\mu_{\text{H}_2} m_{\text{H}} \kappa_{\nu}} \int \kappa_{\nu} \rho \, ds, \quad (\text{A.8})$$

and thus

$$N_{\text{H}_2} = \frac{\tau_{\nu}}{\mu_{\text{H}_2} m_{\text{H}} \kappa_{\nu}}, \quad (\text{A.9})$$

where n_{H_2} is the particle density of hydrogen molecules. This reads in a usable form

$$N_{\text{H}_2} = 2.14 \cdot 10^{25} \text{ cm}^{-2} \tau_{\nu} \left(\frac{\kappa_{\nu}}{0.01 \text{ cm}^2 \text{ g}^{-1}} \right)^{-1}, \quad (\text{A.10})$$

where the chosen numerical value of κ_{ν} is characteristic for wavelength $\lambda \approx 1 \text{ mm}$. As typical H_2 column densities are below 10^{23} cm^{-2} , τ_{ν} is expected to be by far smaller than 1. Thermal dust emission in the (sub-)millimetre regime is therefore optically thin.

For optically thin conditions the equation of radiative transfer can be simplified:

$$I_{\nu} \approx B_{\nu}(T) \tau_{\nu}. \quad (\text{A.11})$$

As the optical depth is related to the column density (Eq. A.10), Eq. (A.11) relates the observed intensity to the column density.

A.2.2. The Planck Function

The Planck function reads

$$B_{\nu}(T) = \frac{2h\nu^3}{c^2} \frac{1}{e^{h\nu/(k_{\text{B}}T)} - 1}, \quad (\text{A.12})$$

in which c is the speed of light and h is Planck's constant. In the Rayleigh-Jeans limit, $h\nu \ll k_{\text{B}}T$, this simplifies to

$$B_{\nu}(T) = \frac{2\nu^2}{c^2} k_{\text{B}}T. \quad (\text{A.13})$$

However, the limiting condition, which reads

$$\lambda \gg 1.44 \text{ mm} \left(\frac{T}{10 \text{ K}} \right)^{-1} \quad (\text{A.14})$$

in useful units, is under typical dust temperatures of about 10 K not fulfilled for observations at about 1 mm wavelength. The exact value of the Planck function is

$$B_{\nu}(T) = 1.475 \cdot 10^{-23} \text{ W m}^{-2} \text{ Hz}^{-1} \text{ sr}^{-1} \left(\frac{\nu}{\text{GHz}} \right)^3 \frac{1}{e^{0.0048(\nu/\text{GHz})(T/10 \text{ K})^{-1}} - 1} \quad (\text{A.15})$$

in useful units.

A.3. Observed Quantities

The received flux per beam is related to the intensity by

$$F_{\nu}^{\text{beam}} = \int I_{\nu} P \, d\Omega, \quad (\text{A.16})$$

where P is the normalised power pattern of the telescope (i.e. $\max[P] = 1$). Defining the beam solid angle as the integral

$$\Omega_{\text{A}} = \int P \, d\Omega, \quad (\text{A.17})$$

one can derive a beam-averaged intensity,

$$\langle I_\nu \rangle = F_\nu^{\text{beam}} / \Omega_A. \quad (\text{A.18})$$

The beam solid angle can be conveniently approximated for telescopes with a beam profile similar to a Gaussian function,

$$P(\theta) = e^{-\theta^2/(2\theta_0^2)} \quad (\text{A.19})$$

(where the angle θ gives the distance from the beam center). The parameter θ_0 is related to the half power beam width of the telescope, θ_{HPBW} , via

$$\theta_0 = \frac{\theta_{\text{HPBW}}}{\sqrt{8 \ln(2)}}. \quad (\text{A.20})$$

For these idealisations the beam solid angle is

$$\Omega_A = 2\pi \int_0^\infty P(\theta) \theta d\theta = 2\pi \int_0^\infty e^{-\theta^2/(2\theta_0^2)} \theta d\theta \quad (\text{A.21})$$

$$= 2\pi \theta_0^2 \quad (\text{A.22})$$

$$= \frac{\pi}{4 \ln(2)} \theta_{\text{HPBW}}^2. \quad (\text{A.23})$$

Using the conversion

$$1 \text{ arcsec} = 4.85 \cdot 10^{-6} \text{ rad}, \quad (\text{A.24})$$

one obtains

$$\Omega_A = 2.665 \cdot 10^{-11} \text{ sr} \left(\frac{\theta_{\text{HPBW}}}{\text{arcsec}} \right)^2. \quad (\text{A.25})$$

The parameter θ_{HPBW} does not need to be the real telescope beam, but depends on the calibration of the data. To give an example, some software packages (e.g., MOPSIC) apply scaling factors to the data (i.e., F_ν^{beam}) when spatially smoothing a map, so that the beam width to that the calibration refers is equal to the spatial resolution of the map after smoothing.

For the idealisations made here the average intensity derived from Eq. (A.18) is a good approximation to the actual intensity only if the source has an extension of the order of the main lobe of the telescope. Otherwise radiation received via the side lobes may have a significant contribution to F_ν^{beam} , and the idealisation of the telescope beam by Gaussian functions is too simple. Inclusion of the side lobes increases Ω_A , and thus reduces $\langle I_\nu \rangle$. The nature of the average intensity derived in Eq. (A.18) is therefore comparable to the one of main beam brightness temperatures used in spectroscopic radio observations. Note that, however, spatial filtering of bolometer systems effectively reduces sidelobes. Unfortunately, this reduction depends in details on the mapping pattern and the source source geometry. It can therefore not be included here.

A.4. Derivation of Conversion Laws

A.4.1. Flux per Beam and Column Density

Equations (A.9, A.11, A.18) relate optical depth, column density, intensity, and the observed flux per beam with each other. Rearrangement yields

$$N_{\text{H}_2} = \frac{F_\nu^{\text{beam}}}{\Omega_A \mu_{\text{H}_2} m_{\text{H}} \kappa_\nu B_\nu(T)}, \quad (\text{A.26})$$

which reads

$$N_{\text{H}_2} = 2.02 \cdot 10^{20} \text{ cm}^{-2} \left(e^{1.439(\lambda/\text{mm})^{-1}(T/10 \text{ K})^{-1}} - 1 \right) \left(\frac{\lambda}{\text{mm}} \right)^3 \cdot \left(\frac{\kappa_\nu}{0.01 \text{ cm}^2 \text{ g}^{-1}} \right)^{-1} \left(\frac{F_\nu^{\text{beam}}}{\text{mJy beam}^{-1}} \right) \left(\frac{\theta_{\text{HPBW}}}{10 \text{ arcsec}} \right)^{-2} \quad (\text{A.27})$$

in useful units.

A.4.2. Flux and Mass

The mass is given by the integral of the column densities across the source,

$$M = \mu_{\text{H}_2} m_{\text{H}} \int N_{\text{H}_2} dA. \quad (\text{A.28})$$

Substitution of Eqs. (A.9, A.11) yields

$$M = \frac{1}{\kappa_\nu B_\nu(T)} \int I_\nu dA. \quad (\text{A.29})$$

The surface element dA is related to the solid angle element $d\Omega$ by $dA = d^2 d\Omega$, where d is the distance of the source. Thus

$$M = \frac{d^2}{\kappa_\nu B_\nu(T)} \int I_\nu d\Omega = \frac{d^2 F_\nu}{\kappa_\nu B_\nu(T)}, \quad (\text{A.30})$$

where $F_\nu = \int I_\nu d\Omega$ is the integrated flux. This reads

$$M = 0.12 M_\odot \left(e^{1.439(\lambda/\text{mm})^{-1}(T/10 \text{ K})^{-1}} - 1 \right) \cdot \left(\frac{\kappa_\nu}{0.01 \text{ cm}^2 \text{ g}^{-1}} \right)^{-1} \left(\frac{F_\nu}{\text{Jy}} \right) \left(\frac{d}{100 \text{ pc}} \right)^2 \left(\frac{\lambda}{\text{mm}} \right)^3 \quad (\text{A.31})$$

in useful units.

A.5. Dust Temperature and Opacity

Dust temperatures of order 10 K have been predicted for dense cores since some time. In the past years Zucconi et al. (2001) estimated dust temperatures in the range 11 to 6 K for solar neighborhood cores. The gas and dust temperature in these should be similar (Goldsmith 2001; also see Galli et al. 2002). Gas temperatures of order 10 K are indeed common for dense cores (e.g., Tafalla et al. 2004). Such temperatures even prevail in dense cores residing in molecular clouds forming stellar clusters (i.e., in Perseus; Rosolowsky et al. 2007). Finally, Schnee et al. (2007b) recently mapped the dust temperature distribution in TMC-1C using data partially also included in the present work. They derived dust temperatures of 13 to 5 K, similar to gas temperatures recently derived for L1544 (Crapsi et al. 2007). These temperatures are lower than those typically inferred from IRAS (≥ 15 K; Schnee et al. 2005) and ISO data (≥ 10 K; Lehtinen et al. 2005), possibly because these missions primarily probed very extended emission because of large beams. We therefore here adopt a temperature of 10 K in absence of protostellar heating.

Figure A.1 illustrates the uncertainty in mass estimates due to uncertainties in the temperature (based on Eq. A.31). For MAMBO this shows that for actual dust temperatures of 12 to 8 K our assumption of a dust temperature of 10 K will lead to an error in the mass estimate of factors 0.7 to 1.5, respectively. These increase to factors of 0.6 to 3 for temperatures of 14 to 6 K. The uncertainty significantly decreases with increasing wavelength.

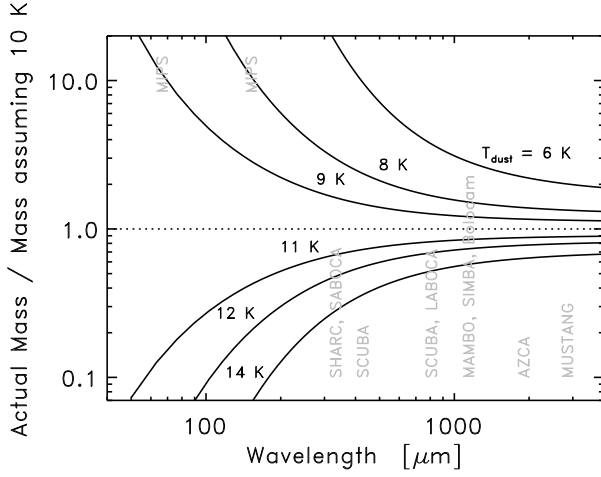


Fig. A.1. The ratio of the actual mass to the one derived when assuming a dust temperature of 10 K. *Solid lines* indicate the ratio for various actual dust temperatures. *Vertical labels* indicate the observing wavelength of several existing and upcoming bolometer arrays (for completeness also including Spitzer MIPS). The related uncertainty in mass estimates decreases significantly with increasing wavelength.

Dust opacities are presently not well constrained. We here adopt dust opacities from Ossenkopf & Henning (1994) that hold for dust with thin ice mantles coagulating for 10^5 yr at an H-density of 10^6 cm^{-3} , respectively (keeping the product of time and density constant) for 10^6 yr at an H_2 -density of $5 \cdot 10^4$ cm^{-3} , which appear to be reasonable conditions. At the MAMBO wavelength of 1.2 mm their opacity of 0.01 cm^2 per gram of interstellar matter is in between values used and suggested by other groups (from 0.005 cm^2 g^{-1} [Motte et al. 1998] to 0.02 cm^2 g^{-1} [Krügel & Siebenmorgen 1994]).

The opacities quoted above are consistent with observational opacity constraints. van der Tak et al. (1999) conclude that only coagulated dust from Ossenkopf & Henning (1994) provides a match to their extensive dust and molecular line emission data set. They probed a massive young star with a heated envelope though. Anyway, Shirley et al. (submitted) derive the same for a less luminous YSO in B335.

A.6. Standard c2d Conversion Factors

A.6.1. Conversion from Dust Emission

Table A.1 summarises the c2d standard conversion factors for masses and column densities from dust emission. The wavelength-dependent dust opacities are from Ossenkopf & Henning (1994) and hold for dust with thin ice mantles coagulating for 10^5 yr at an H-density of 10^6 cm^{-3} . We adopt a dust temperature of 10 K. This choice for the dust temperature and opacity are the standard assumptions made by the c2d collaboration. The values listed in Table A.1 are thus thought to serve as a standard reference within the collaboration.

A.6.2. Conversion to Extinction

The c2d standard conversion factor between column densities and visual extinction,

$$N_{\text{H}_2} = 9.4 \cdot 10^{20} \text{ cm}^{-2} (A_V/\text{mag}), \quad (\text{A.32})$$

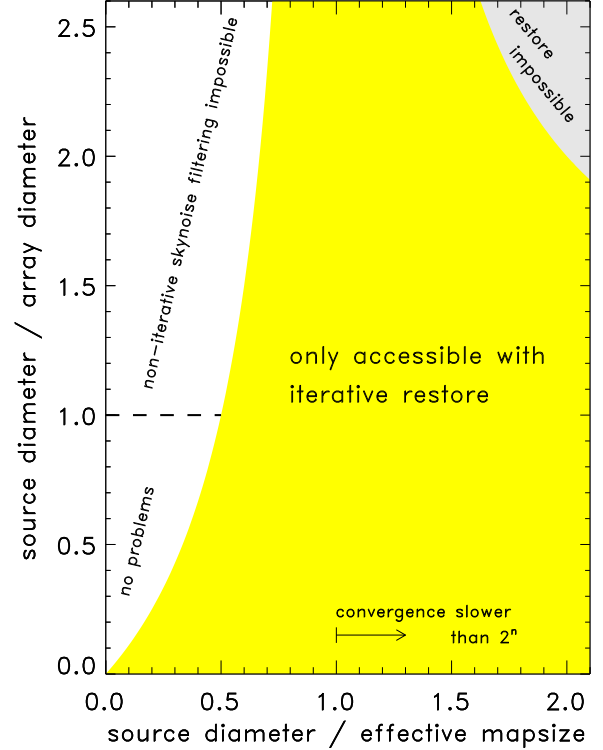


Fig. B.1. Summary of mapping parameter spaces accessible by various techniques. The *non-highlighted area* at $d_{\text{source}}/\ell_{\text{eff}} < 1$ is accessible using conventional techniques. *This is the realm in which any past and present bolometer arrays, including total power devices like SCUBA II and LABOCA, operate.* If one wishes to remove skynoise, and does not use an iterative approach for this, this further limits the accessible parameter space to $d_{\text{source}}/d_{\text{array}} < 1$. Failure to comply with these limits results in artifacts of various kind. The *area with light highlighting* is accessible when using our iterative restore algorithm, which by design also includes iterative skynoise filtering. This significantly increases the accessible mapping parameter space. However, as indicated by the *arrow*, the convergence speed decreases when increasing $d_{\text{source}}/\ell_{\text{eff}}$. Maps occupying the *area with strong highlighting* cannot be reduced without artifacts.

is taken from Bohlin et al. (1978). They combined measurements of H_2 and Hi from the Copernicus satellite for lightly reddened stars to get

$$\langle [N_{\text{H}\text{i}} + 2N_{\text{H}_2}]/E(B - V) \rangle = 5.8 \cdot 10^{21} \text{ cm}^{-2} \text{ mag}^{-1}. \quad (\text{A.33})$$

For a standard total-to-selective extinction ratio $R_V = A_V/E(B - V) = 3.1$ this yields the above conversion factor.

Appendix B: Data Reduction Details

B.1. Mapping Parameter Space

The equations on limitations of data reduction approaches, Eqs. (1-3), effectively span parameter spaces accessible by different reduction methods. We explore these limits in Fig. B.1.

For brevity, we express the effective map size, $\ell_{\text{scan}} + \ell_{\text{chop}}$, by ℓ_{eff} in the following. The vertical limit at $d_{\text{source}}/d_{\text{array}} = 1$ directly follows from Eq. (3). In principle, it continues to $d_{\text{source}}/\ell_{\text{eff}} \rightarrow \infty$. However, Eq. (2) anyway limits the realm of unproblematic data reduction along this axis. To obtain an expression for this limit, we divide Eq. (2) by d_{array} and solve for

Table A.1. Standard c2d conversion factors for masses and column densities from dust emission. For each bolometer camera employed by the c2d collaboration we list the effective wavelength, the half power beam width, the dust opacity at the effective wavelength (per gram of ISM), the conversion factors between intensity and column density, and between integrated flux density and mass (this for a distance of 100 pc), respectively.

Camera	λ μm	θ_{HPBW} arcsec	κ_{ν} $\text{cm}^2 \text{g}^{-1}$	$N_{\text{H}_2}/F_{\nu}^{\text{beam}}$ $\text{cm}^{-2} (\text{mJy beam}^{-1})^{-1}$	$M/F_{\nu}(d = 100 \text{ pc})$ $M_{\odot} \text{Jy}^{-1}$
SHARC II	350	8.5	0.101	$7.13 \cdot 10^{19}$	0.031
SCUBA	450	7	0.0619	$1.42 \cdot 10^{19}$	0.041
	850	15	0.0182	$1.34 \cdot 10^{20}$	0.18
BOLOCAM	1120	31	0.0114	$6.77 \cdot 10^{19}$	0.39
MAMBO	1200	11	0.0102	$6.69 \cdot 10^{20}$	0.47
SIMBA	1200	24	0.0102	$1.41 \cdot 10^{20}$	0.47

$d_{\text{source}}/d_{\text{array}}$. At $d_{\text{source}}/\ell_{\text{eff}} > 1$, the region accessible to iterative techniques is limited by

$$d_{\text{source}} < \ell_{\text{scan}} + \ell_{\text{chop}} + d_{\text{array}}. \quad (\text{B.1})$$

Beyond this limit, no receiver of the bolometer array moves off source, and sky brightness information is impossible to reconstruct. Equation (1) sets the indicated limits on the convergence speed.

B.2. Illustration

Figure B.2 summarizes the data reduction improvements due to our iterative method. To do so, we created artificial raw data (for the L1103-2 region of our survey) towards a circular source of $500''$ diameter and spatially constant intensity. We included beam smoothing, and added correlated and uncorrelated noise at various amplitudes. In order to roughly match the observed decrease of the noise level during skynoise filtering, the correlated-to-uncorrelated noise ratio is chosen to be 3.

Figure B.2 (a) presents a map obtained from noiseless raw data, using classical methods (i.e., plain reconstruction of the intensity distribution from the chopped bolometer data). Inspection reveals intensity depressions of $> 30\%$ within the source. Since such biases are additive, these depressions can offset intensities of smaller objects located in the map center, if such are present. Within the inner area of $400''$ diameter, the mean intensity has dropped to 80% of the true value.

Figure B.2 (b) is constructed like the map in panel (a), but was derived from raw data with superimposed artificial noise. We use noise-to-source intensity fractions of 90% and 30% for the correlated and uncorrelated noise. The simulated source thus corresponds to very faint extended features in our maps. Correspondingly, classical data reduction (i.e., reconstruction without skynoise filtering) gives a map full of artifacts (note the intensity gradient within the source) in which the signal-to-noise intensity ratio is of order 1. In practice, such a map would not be usable.

Figure B.2 (c), however, shows that iterative map reconstruction including skynoise filtering allows to reliably extract source structure from the data used for panel (b). Since most of the correlated noise has been removed, the signal-to-noise intensity ratio is of order 3 here. Furthermore, the artifacts present in panels (a) and (b) are gone: the mean intensity within the inner $400''$ diameter is 101% for the map shown.

References

Altenhoff, W. J., Baars, J. W. M., Wink, J. E., & Downes, D. 1987, A&A, 184, 381

- Alves, J., Lombardi, M., & Lada, C. J. 2007, A&A, 462, L17
 Alves, J. F., Lada, C. J., & Lada, E. A. 2001, Nature, 409, 159
 Andre, P. & Montmerle, T. 1994, ApJ, 420, 837
 André, P., Motte, F., & Bacmann, A. 1999, ApJ, 513, L57
 Andre, P., Ward-Thompson, D., & Barsony, M. 1993, ApJ, 406, 122
 —. 2000, Protostars and Planets IV, 59
 Barsony, M. & Kenyon, S. J. 1992, ApJ, 384, L53
 Beichman, C. A., Neugebauer, G., Habing, H. J., Clegg, P. E., & Chester, T. J., eds. 1988, Infrared astronomical satellite (IRAS) catalogs and atlases. Volume 1: Explanatory supplement
 Belloche, A., Hennebelle, P., & André, P. 2006, A&A, 453, 145
 Blitz, L. 1993, in Protostars and Planets III, ed. E. H. Levy & J. I. Lunine, 125–161
 Bohlin, R. C., Savage, B. D., & Drake, J. F. 1978, ApJ, 224, 132
 Bourke, T. L., Crapsi, A., Myers, P. C., et al. 2005, ApJ, 633, L129
 Bourke, T. L., Hyland, A. R., & Robinson, G. 1995, MNRAS, 276, 1052
 Bourke, T. L., Myers, P. C., Evans, II, N. J., et al. 2006, ApJ, 649, L37
 Caselli, P., Benson, P. J., Myers, P. C., & Tafalla, M. 2002, ApJ, 572, 238
 Chen, H., Grenfell, T. G., Myers, P. C., & Hughes, J. D. 1997, ApJ, 478, 295
 Chen, H., Myers, P. C., Ladd, E. F., & Wood, D. O. S. 1995, ApJ, 445, 377
 Claussen, M. J., Marvel, K. B., Wootten, A., & Wilking, B. A. 1998, ApJ, 507, L79
 Clemens, D. P. & Barvainis, R. 1988, ApJS, 68, 257
 Cox, A. N. 2000, Allen’s astrophysical quantities (Allen’s astrophysical quantities, 4th ed. Publisher: New York: AIP Press; Springer, 2000. Edited by Arthur N. Cox. ISBN: 0387987460)
 Crapsi, A., Caselli, P., Walmsley, C. M., et al. 2005, ApJ, 619, 379
 —. 2004, A&A, 420, 957
 Crapsi, A., Caselli, P., Walmsley, M. C., & Tafalla, M. 2007, A&A, 470, 221
 Dame, T. M., Ungerechts, H., Cohen, R. S., et al. 1987, ApJ, 322, 706
 De Vries, C. H., Narayanan, G., & Snell, R. L. 2002, ApJ, 577, 798
 di Francesco, J., Evans, II, N. J., Caselli, P., et al. 2007, in Protostars and Planets V, ed. B. Reipurth, D. Jewitt, & K. Keil, 17–32
 Dobashi, K., Bernard, J.-P., Yonekura, Y., & Fukui, Y. 1994, ApJS, 95, 419
 Dunham, M. M., Evans, II, N. J., Bourke, T. L., et al. 2006, ApJ, 651, 945
 Emerson, D. T., Klein, U., & Haslam, C. G. T. 1979, A&A, 76, 92
 Enoch, M. L., Glenn, J., Evans, II, N. J., et al. 2007, ApJ, 666, 982
 Enoch, M. L., Young, K. E., Glenn, J., et al. 2006, ApJ, 638, 293
 Evans, N. I. 2003, in SFChem 2002: Chemistry as a Diagnostic of Star Formation, proceedings of a conference held August 21-23, 2002 at University of Waterloo, Waterloo, Ontario, Canada N2L 3G1. Edited by Charles L. Curry and Michel Fich. NRC Press, Ottawa, Canada, 2003, p. 157., ed. C. L. Curry & M. Fich, 157–+
 Evans, N. J., Allen, L. E., Blake, G. A., et al. 2003, PASP, 115, 965
 Evans, N. J., Rawlings, J. M. C., Shirley, Y. L., & Mundy, L. G. 2001, ApJ, 557, 193
 Franco, G. A. P. 1989, A&A, 223, 313
 Galli, D., Walmsley, M., & Gonçalves, J. 2002, A&A, 394, 275
 Genzel, R. & Stutzki, J. 1989, ARA&A, 27, 41
 Goldsmith, P. F. 2001, ApJ, 557, 736
 Goodwin, S. P., Ward-Thompson, D., & Whitworth, A. P. 2002, MNRAS, 330, 769
 Greene, T. P., Wilking, B. A., Andre, P., Young, E. T., & Lada, C. J. 1994, ApJ, 434, 614
 Hatchell, J., Fuller, G. A., Richer, J. S., Harries, T. J., & Ladd, E. F. 2007, A&A, 468, 1009
 Hatchell, J., Richer, J. S., Fuller, G. A., et al. 2005, A&A, 440, 151
 Herbig, G. H. & Jones, B. F. 1983, AJ, 88, 1040
 Huard, T. L., Myers, P. C., Murphy, D. C., et al. 2006, ApJ, 640, 391

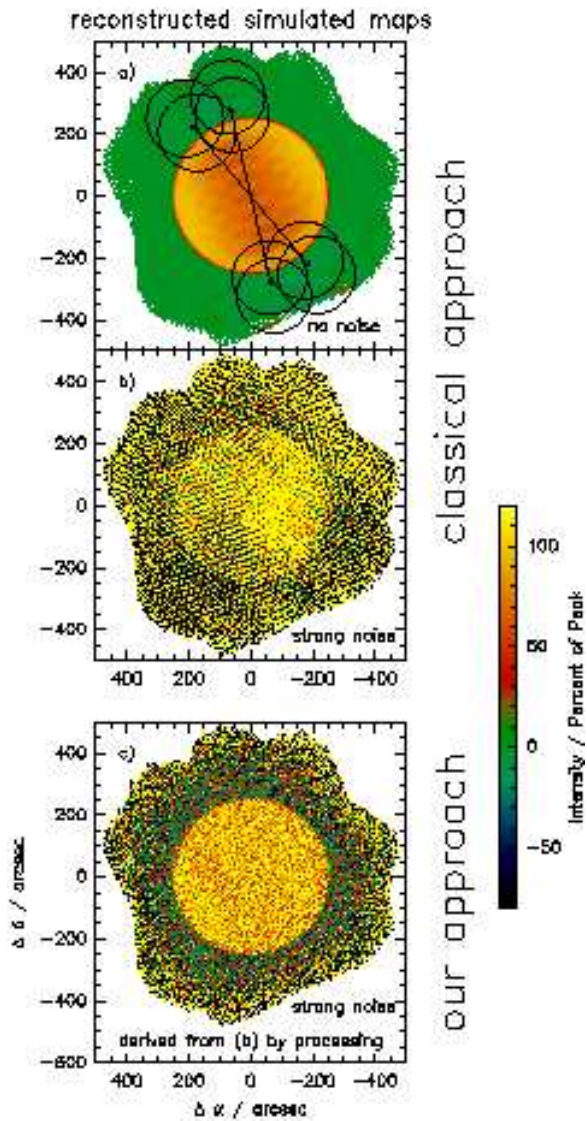


Fig. B.2. Demonstration of our bolometer data reduction approach, using artificial maps centered on a source of $500''$ diameter. *Panels (a) and (b)* present maps reconstructed using classical methods. *Panel (c)* displays a map derived using our method, which was derived by iterative processing of the data shown in panel (b). It is obvious that, even when using noisy raw data, our new approach yields maps with an artifact level better than those derived from noiseless data using classical methods (note depressions of $> 30\%$ in panel [a], and their absence in panel [c]). The *arrows in panel (a)* indicate the length ($600''$) and mean orientation of the two co-added maps. *Circles and their separation* show the array diameter and the chop throw. *Labels* indicate the presence of noise (a superposition of correlated and uncorrelated noise at levels of 90% and 30%, respectively, of the model source peak intensity), or its absence. [See the alternative URL in the astro-ph comments, and the journal article, for higher resolution maps.]

Jijina, J., Myers, P. C., & Adams, F. C. 1999, *ApJS*, 125, 161
 Johnstone, D. & Bally, J. 2006, *ApJ*, 653, 383
 Johnstone, D., Di Francesco, J., & Kirk, H. 2004, *ApJ*, 611, L45
 Johnstone, D., Fich, M., Mitchell, G. F., & Moriarty-Schieven, G. 2001, *ApJ*, 559, 307
 Johnstone, D., Matthews, H., & Mitchell, G. F. 2006, *ApJ*, 639, 259
 Johnstone, D., Wilson, C. D., Moriarty-Schieven, G., et al. 2000, *ApJ*, 545, 327
 Jones, C. E. & Basu, S. 2002, *ApJ*, 569, 280
 Jones, C. E., Basu, S., & Dubinski, J. 2001, *ApJ*, 551, 387
 Jørgensen, J. K., Johnstone, D., Kirk, H., & Myers, P. C. 2007, *ApJ*, 656, 293
 Kandori, R., Nakajima, Y., Tamura, M., et al. 2005, *AJ*, 130, 2166

Kauffmann, J., Bertoldi, F., Evans, N. J., & the C2D Collaboration. 2005, *Astronomische Nachrichten*, 326, 878
 Kenyon, S. J., Dobrzycka, D., & Hartmann, L. 1994, *AJ*, 108, 1872
 Kenyon, S. J. & Hartmann, L. 1995, *ApJS*, 101, 117
 Kirk, J. M., Ward-Thompson, D., & André, P. 2005, *MNRAS*, 360, 1506
 Krügel, E. & Siebenmorgen, R. 1994, *A&A*, 288, 929
 Kreysa, E., Gemünd, H.-P., Gromke, J., et al. 1999, *Infrared Physics and Technology*, 40, 191
 Kroupa, P. 2002, *Science*, 295, 82
 Kun, M. 1998, *ApJS*, 115, 59
 Kun, M. & Prusti, T. 1993, *A&A*, 272, 235
 Lada, C. J. 1987, in *IAU Symp. 115: Star Forming Regions*, 1–15
 Larson, R. B. 1981, *MNRAS*, 194, 809
 —. 2003, *Reports of Progress in Physics*, 66, 1651
 Lee, C. W. & Myers, P. C. 1999, *ApJS*, 123, 233
 Lee, C. W., Myers, P. C., & Tafalla, M. 2001, *ApJS*, 136, 703
 Lehtinen, K., Mattila, K., & Lemke, D. 2005, *A&A*, 437, 159
 Leisawitz, D., Bash, F. N., & Thaddeus, P. 1989, *ApJS*, 70, 731
 Lonsdale, C. J., Smith, H. E., Rowan-Robinson, M., et al. 2003, *PASP*, 115, 897
 Maddalena, R. J., Morris, M., Moscowitz, J., & Thaddeus, P. 1986, *ApJ*, 303, 375
 Magnani, L., Caillault, J.-P., Buchalter, A., & Beichman, C. A. 1995, *ApJS*, 96, 159
 McKee, C. F. & Holliman, J. H. 1999, *ApJ*, 522, 313
 Moshir, M. & et al. 1990, in *IRAS Faint Source Catalogue, version 2.0 (1990)*, 0–+
 Motte, F. & André, P. 2001, *A&A*, 365, 440
 Motte, F., André, P., & Neri, R. 1998, *A&A*, 336, 150
 Murdin, P. & Penston, M. V. 1977, *MNRAS*, 181, 657
 Myers, P. C. & Benson, P. J. 1983, *ApJ*, 266, 309
 Myers, P. C., Fuller, G. A., Goodman, A. A., & Benson, P. J. 1991, *ApJ*, 376, 561
 Myers, P. C., Fuller, G. A., Mathieu, R. D., et al. 1987, *ApJ*, 319, 340
 Myers, P. C. & Ladd, E. F. 1993, *ApJ*, 413, L47
 Myers, P. C., Linke, R. A., & Benson, P. J. 1983, *ApJ*, 264, 517
 Obayashi, A., Kun, M., Sato, F., Yonekura, Y., & Fukui, Y. 1998, *AJ*, 115, 274
 Ossenkopf, V. & Henning, T. 1994, *A&A*, 291, 943
 Paganì, L. & Breart de Boisanger, C. 1996, *A&A*, 312, 989
 Robitaille, T. P., Whitney, B. A., Indebetouw, R., Wood, K., & Denzmore, P. 2006, *ApJS*, 167, 256
 Rosolowsky, E. W., Pineda, J. E., Foster, J. B., et al. 2007, *ArXiv e-prints*, 711
 Ryden, B. S. 1996, *ApJ*, 471, 822
 Schnee, S., Caselli, P., Goodman, A., et al. 2007a, *ApJ*, 671, 1839
 Schnee, S., Kauffmann, J., Goodman, A., & Bertoldi, F. 2007b, *ApJ*, 657, 838
 Schnee, S. L., Ridge, N. A., Goodman, A. A., & Li, J. G. 2005, *ApJ*, 634, 442
 Shu, F. H. 1977, *ApJ*, 214, 488
 Stanke, T., Smith, M. D., Gredel, R., & Khanzadyan, T. 2006, *A&A*, 447, 609
 Straizys, V., Černis, K., & Bartaščiūtė, S. 2003, *A&A*, 405, 585
 Straizys, V., Černis, K., Kazlauskas, A., & Meistas, E. 1992, *Baltic Astronomy*, 1, 149
 Tafalla, M., Myers, P. C., Caselli, P., & Walmsley, C. M. 2004, *A&A*, 416, 191
 Tafalla, M., Myers, P. C., Caselli, P., Walmsley, C. M., & Comito, C. 2002, *ApJ*, 569, 815
 Tassis, K. 2007, *MNRAS*, 379, L50
 Terebey, S., Chandler, C. J., & André, P. 1993, *ApJ*, 414, 759
 van der Tak, F. F. S., van Dishoeck, E. F., Evans, II, N. J., Bakker, E. J., & Blake, G. A. 1999, *ApJ*, 522, 991
 Visser, A. E., Richer, J. S., & Chandler, C. J. 2002, *AJ*, 124, 2756
 Ward-Thompson, D., André, P., Crutcher, R., et al. 2007, in *Protostars and Planets V*, ed. B. Reipurth, D. Jewitt, & K. Keil, 33–46
 Ward-Thompson, D., Motte, F., & André, P. 1999, *MNRAS*, 305, 143
 Whitney, B. A., Wood, K., Bjorkman, J. E., & Wolff, M. J. 2003, *ApJ*, 591, 1049
 Williams, J. P., de Geus, E. J., & Blitz, L. 1994, *ApJ*, 428, 693
 Wu, J., Dunham, M. M., Evans, II, N. J., Bourke, T. L., & Young, C. H. 2007, *AJ*, 133, 1560
 Yonekura, Y., Dobashi, K., Mizuno, A., Ogawa, H., & Fukui, Y. 1997, *ApJS*, 110, 21
 Young, C. H., Bourke, T. L., Young, K. E., et al. 2006a, *AJ*, 132, 1998
 Young, C. H. & Evans, II, N. J. 2005, *ApJ*, 627, 293
 Young, C. H., Jørgensen, J. K., Shirley, Y. L., et al. 2004a, *ApJS*, 154, 396
 Young, K. E., Enoch, M. L., Evans, II, N. J., et al. 2006b, *ApJ*, 644, 326
 Young, K. E., Lee, J.-E., Evans, II, N. J., Goldsmith, P. F., & Doty, S. D. 2004b, *ApJ*, 614, 252
 Yun, J. L. & Clemens, D. P. 1994, *ApJS*, 92, 145
 Zucconi, A., Walmsley, C. M., & Galli, D. 2001, *A&A*, 376, 650